

MASTER

Towards the elucidation of the Fischer-Tropsch synthesis reaction on stepped Rhodium (211) surfaces

Broos, R.J.P.

Award date:
2014

[Link to publication](#)

Disclaimer

This document contains a student thesis (bachelor's or master's), as authored by a student at Eindhoven University of Technology. Student theses are made available in the TU/e repository upon obtaining the required degree. The grade received is not published on the document as presented in the repository. The required complexity or quality of research of student theses may vary by program, and the required minimum study period may vary in duration.

General rights

Copyright and moral rights for the publications made accessible in the public portal are retained by the authors and/or other copyright owners and it is a condition of accessing publications that users recognise and abide by the legal requirements associated with these rights.

- Users may download and print one copy of any publication from the public portal for the purpose of private study or research.
- You may not further distribute the material or use it for any profit-making activity or commercial gain

Molecular Catalysis
Department of Chemical Engineering and Chemistry
Eindhoven University of Technology

Towards the elucidation of the
Fischer-Tropsch synthesis reaction on
stepped Rhodium (211) surfaces

ROBIN BROOS

May 28, 2014

Graduation Report

Supervisors

Ir. I.A.W. Filot
Prof. dr. ir. E.J.M. Hensen

Advising Committee

Prof. dr. ir. E.J.M. Hensen
Dr. ir. T.A. Nijhuis
Prof. dr. R.A. van Santen

Contents

| | | |
|----------|--|-----------|
| 1 | Introduction | 1 |
| 1.1 | The Fischer-Tropsch reaction | 1 |
| 1.1.1 | Mechanism | 2 |
| 1.1.2 | Choice of Catalyst | 3 |
| 1.2 | The Scope of this Report | 4 |
| 2 | Theory and computational methods | 6 |
| 2.1 | Density functional theory | 6 |
| 2.1.1 | Kohn-Sham theory | 8 |
| 2.1.2 | LDA | 8 |
| 2.1.3 | Generalized Gradient Approximations | 9 |
| 2.1.4 | Projector augmented wave method | 9 |
| 2.2 | Kinetics | 10 |
| 2.2.1 | Adsorption | 10 |
| 2.2.2 | Bond order conservation principle | 11 |
| 2.2.3 | Langmuir-Hinshelwood mechanism | 12 |
| 2.2.4 | Eley-Rideal mechanism | 12 |
| 2.2.5 | Method of working | 13 |
| 2.2.6 | Nudged Elastic Band method | 14 |
| 2.3 | Microkinetic modelling | 15 |
| 2.3.1 | Hertz-Knudsen reaction kinetics | 16 |
| 2.3.2 | Transition state theory | 17 |
| 2.3.3 | Brønsted-Evans-Polanyi relation. | 17 |
| 2.3.4 | Degree of rate control | 18 |
| 3 | Computational details | 19 |
| 4 | Results and Discussion | 22 |
| 4.1 | DFT calculations | 22 |
| 4.1.1 | Adsorption and desorption reactions | 22 |
| 4.1.2 | CO dissociation reactions | 22 |
| 4.1.3 | The Methanation reaction | 25 |
| 4.1.4 | The production of C ₁ -oxygenates | 28 |
| 4.1.5 | CH _x -CH _y coupling reactions | 37 |
| 4.1.6 | Hydrogenations towards C ₂ - Hydrocarbons | 39 |
| 4.1.7 | CO insertion | 42 |
| 4.1.8 | Hydrogenations towards C ₂ -Oxygenates | 45 |
| 4.1.9 | Towards the formation of C ₃ -Oxygenates | 51 |
| 4.2 | Thermodynamic analysis | 53 |
| 4.3 | Microkinetic simulations | 54 |
| 4.3.1 | The Methanation reaction | 54 |
| 4.3.2 | The production of Methanol | 60 |
| 4.3.3 | The production of C ₂ -Oxygenates | 66 |

| | | |
|----------|--|-----------|
| 5 | Conclusions | 73 |
| 6 | Outlook | 75 |
| 7 | Acknowledgements | 76 |
| 8 | Appendix | 80 |
| 8.1 | CO dissociation reactions | 80 |
| 8.2 | water formation | 83 |
| 8.3 | Elementary Reaction Steps with kinetic parameters for the Methanation reaction | 84 |
| 8.4 | Elementary reaction steps as calculated for the reaction towards methanol | 86 |
| 8.5 | Elementary reaction steps as calculated for the C-C coupling reactions | 92 |
| 8.6 | Elementary reaction steps as calculated for the hydrogenation towards C2-hydrocarbons | 95 |
| 8.7 | Elementary reaction steps as calculated for the CO-insertion reactions | 99 |
| 8.8 | Elementary reaction steps as calculated for the hydrogenation towards C2-Oxygenates | 100 |
| 8.9 | Elementary reaction steps as calculated for the hydrogenation towards C3-Oxygenates | 113 |

Abstract

Rhodium nanoparticles are well known for their ability to act as a catalyst in the Fischer-Tropsch reaction. Rhodium catalysts have a selectivity towards relatively short oxygenates such as methanol and ethanol due to their slow CO dissociation rate and relatively fast hydrogenation rate. In this thesis, rhodium (211) is investigated catalyzing C-C coupling reactions, C-O bond activation, and hydrogenation reactions.

In the Literature, there are ongoing debates about the actual mechanism in the Fischer-Tropsch synthesis. One of the key issues is the manner in which CO dissociation proceeds. CO dissociation can proceed via a direct pathway, or via a hydrogen assisted pathway at which CO is first partially hydrogenated before the CO bond is split. In this thesis, it is shown that the direct CO dissociation is more preferable than the hydrogen assisted CO dissociation. Another ongoing debate concerns the C-C coupling and its propagation. The two mechanisms that are the most plausible for the coupling reactions are the Pichler-Schulz mechanism and the Biloen-Sachtler mechanism. Both mechanisms are studied within this thesis. In this computational study, the underlying mechanism of Rh-based Fischer-Tropsch catalysis is studied. All elementary reaction steps leading to short chain oxygenates, as well as hydrocarbon formation, are studied. A stepped Rh(211) catalyst is used as a model system for its well known ability to efficiently dissociate CO. From microkinetic studies base on quantum chemical data, it was derived that the selectivity of the reaction was highest for methane. Further, there was a selectivity to ethylene.

1 Introduction

Due to the limited availability of more easily accessible petroleum, the role of alternative energy resources is becoming increasingly more important. Because of its abundance, natural gas plays an important role as a feedstock for the synthesis of fuels and chemicals. Synthesis gas, that is derived from natural gas by steam methane reforming, can be used to produce higher hydrocarbons using the Fischer-Tropsch process [1]. Furthermore, the natural gas, oil and coal reserves are starting to run low. By estimation, we can rely on natural gas and oil for a little more than 50 years and on coal 150 years, while consuming the same amount as in 2012. This is shown in figure 1. The total reserves in 2012 as well as the annual global consumption per fossil fuel type is depicted in billions of metric tons of oil equivalents.

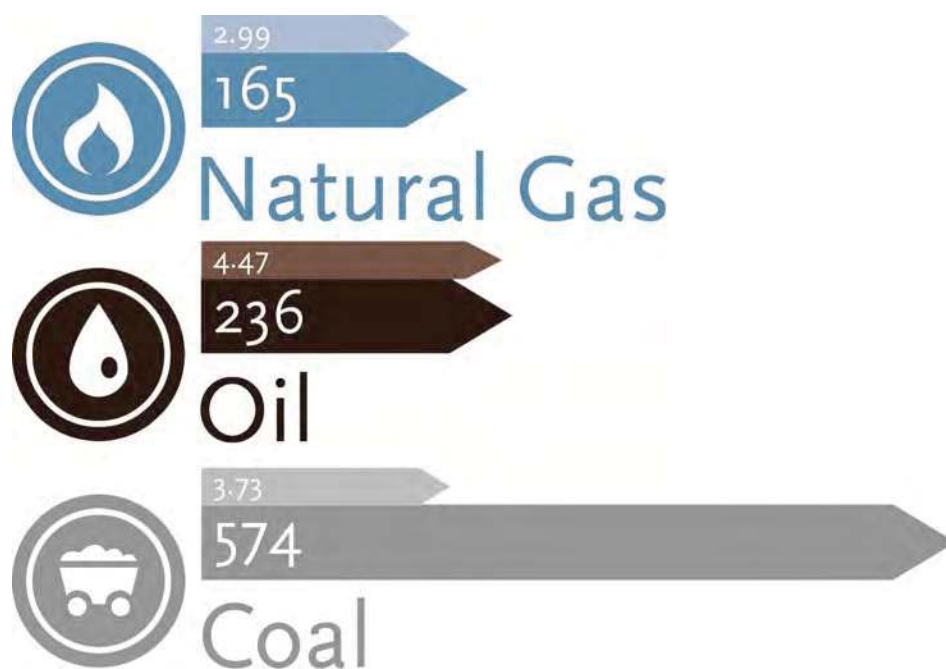


Figure 1: Reserves are depicted by darker arrows, the annual consumption by lighter arrows. The values are in billion metric tons of oil equivalents (by courtesy of Ir. Ivo A. W. Filot).

1.1 The Fischer-Tropsch reaction

Fischer-Tropsch (FT) synthesis is an attractive approach for the utilization of non-petroleum feedstock to produce ultra clean diesel, kerosene, or chemical feedstock, which is shown in figure 2. Synthesis gas needed for the FT reaction can be acquired via autothermal reforming of natural gas, gasification of coal, and in particular, pyrolysis of biomass. Subsequently, FT synthesis converts synthesis gas ($\text{CO} + \text{H}_2$) into longer hydrocarbons. Because of the worldwide demand for a decreased dependence on petroleum, FT synthesis has received renewed interest [2,3]. Quantum-chemical calculations provide valuable insights into the mechanistic pathway converting synthesis gas

into longer hydrocarbons.

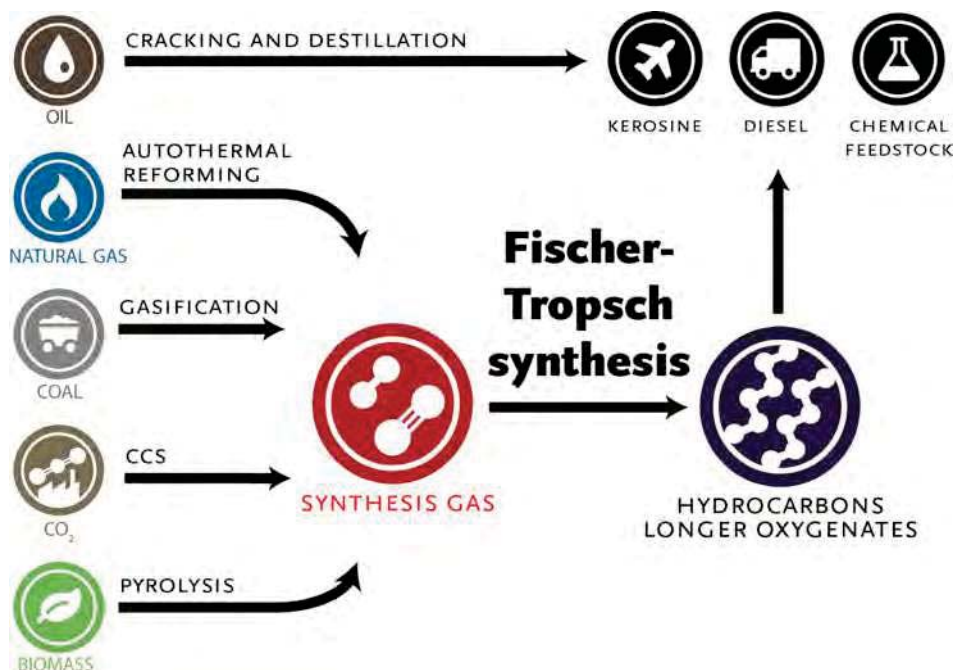


Figure 2: The Fischer-Tropsch process as an attractive alternative route towards clean transport fuels and chemical feedstock (by courtesy of Ir. Ivo A. W. Filot).

1.1.1 Mechanism

Even though the Fischer-Tropsch reaction is almost a century old, its underlying mechanism is still poorly understood. Recently, many insights about the fundamental factors governing activity and selectivity in FT have been elucidated using theoretical [1,4–7] as well as experimental [8,9] approaches. There is an on-going debate in the Literature about the mechanism of the Fischer-Tropsch synthesis reaction. Among the variety of mechanisms that are proposed, two types of mechanisms are the most plausible. During the initiation step, both mechanisms first dissociate a CO to a C_1 species. The mechanisms differ in the propagation step. One of the mechanisms assumes that during chain growth, CO dissociation needs to take place again, before the reaction can start, resulting in a CH_x-CH_x coupling. This mechanism is called the Biloen-Sachtler mechanism or Carbide mechanism [10].

The other mechanism states, that the initial C_1 species can directly couple with a CO species. This mechanism is called the Pichler-Schulz mechanism or CO insertion mechanism [11]. Both mechanisms are depicted schematically in figure 3.

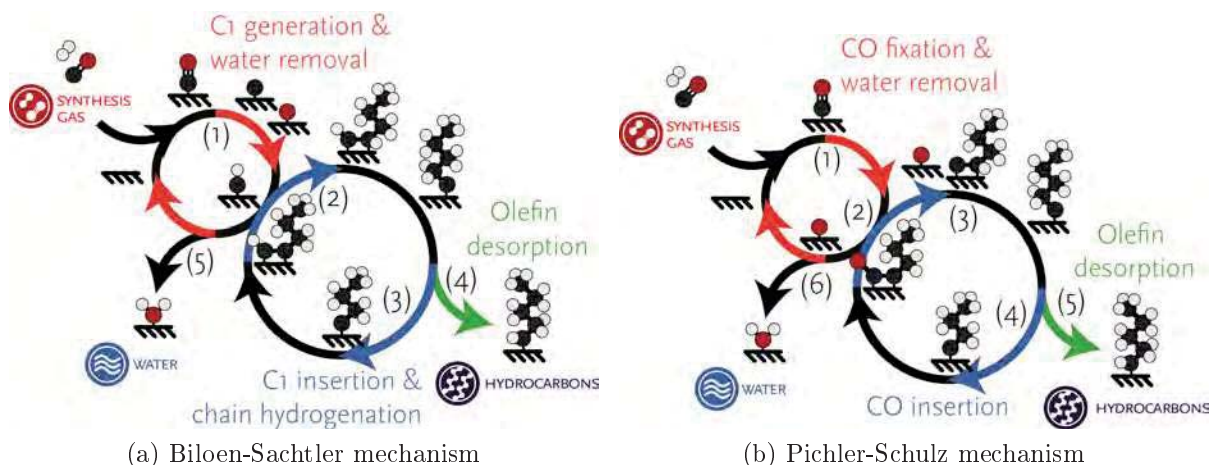


Figure 3: Schematic representations of the two main mechanisms proposed in the Fischer-Tropsch synthesis reaction.

The nature of the catalyst decides which of the two mechanisms is more likely. If the catalyst is very active for the breaking of the CO bond, then there is an abundance of C_1 species on the surface. This abundance makes it more plausible for a C_1 species to react with another C_1 species rather than reacting with a CO. This makes the Biloen-Sachtler mechanism more plausible than the Pichler-Schulz mechanism. When, on the other hand, CO dissociation is not that fast, the Pichler-Schulz mechanism will be more plausible than the Biloen-Sachtler mechanism. In short, when there are too little C_1 species on the surface, the chances for reacting with a CO species are higher than the chances for reacting with a C_1 species.

1.1.2 Choice of Catalyst

Depending on the catalyst, the Fischer-Tropsch synthesis reaction can be applied to get a variety of products. Figure 4 shows the different catalysts that can be used in the Fischer Tropsch process, together with their main products.

When Iron, Ruthenium or Cobalt is being used, the main products are longer hydrocarbons. The reason for this is the relatively high rate of CO dissociation, combined with a high rate of CH_x insertion. Finally, the rate of methane formation must be low because CH_x species are needed for the formation of longer hydrocarbons.

If, for instance, Nickel is used as a catalyst, the main product of the reaction will be methane. This is due to a slow rate of CO dissociation combined with a fast hydrogenation towards methane.

In this report, we have only considered Rhodium as a catalyst. Rhodium will produce short oxygenates, consisting of mainly methanol, acetaldehyde and ethanol. The reason for this is that Rhodium has a moderate rate of CO dissociation combined with slow rate of methane formation. In this manner, CH_x CO coupling can take place.

However, CO dissociation is not fast enough to produce long chains, so that C1 and C2 oxygenates will predominantly be formed.



Figure 4: Different product selectivities with corresponding catalysts (by courtesy of Ir. Ivo A. W. Filot)

1.2 The Scope of this Report

Rhodium yields a variety of products when it is used during the Fischer-Tropsch process. This is also graphically represented in figure 5. For a better understanding of this composition, it is key to know which elementary reactions are taking place on the catalyst and what reactions are rate controlling. By doing multi scale modeling, it is possible to acquire insights into the mechanism. Multi scale modeling combines different length and timescale calculations. In this study, DFT is combined with microkinetic modeling. The goal of this study is the elucidation of the pathways towards the formation of the shorter oxygenates and short hydrocarbons on a stepped rhodium surface.

An earlier study [12], that focused on the elucidation of the formation of Ethanol during Fischer-Tropsch synthesis on stepped rhodium, has shown that it is not possible to combine multiple datasets from the Literature to get a new and valid dataset. By combining the datasets, the underlying thermodynamics get twisted, meaning that the new dataset consists of thermodynamically incorrect values. Therefore, all elementary reactions are calculated in a similar fashion. This way, we can be sure that the thermodynamics add up. Different datasets are linked through migration corrections. Sadly, these are often not reported. Only when all migration corrections are known, multiple datasets could be combined.

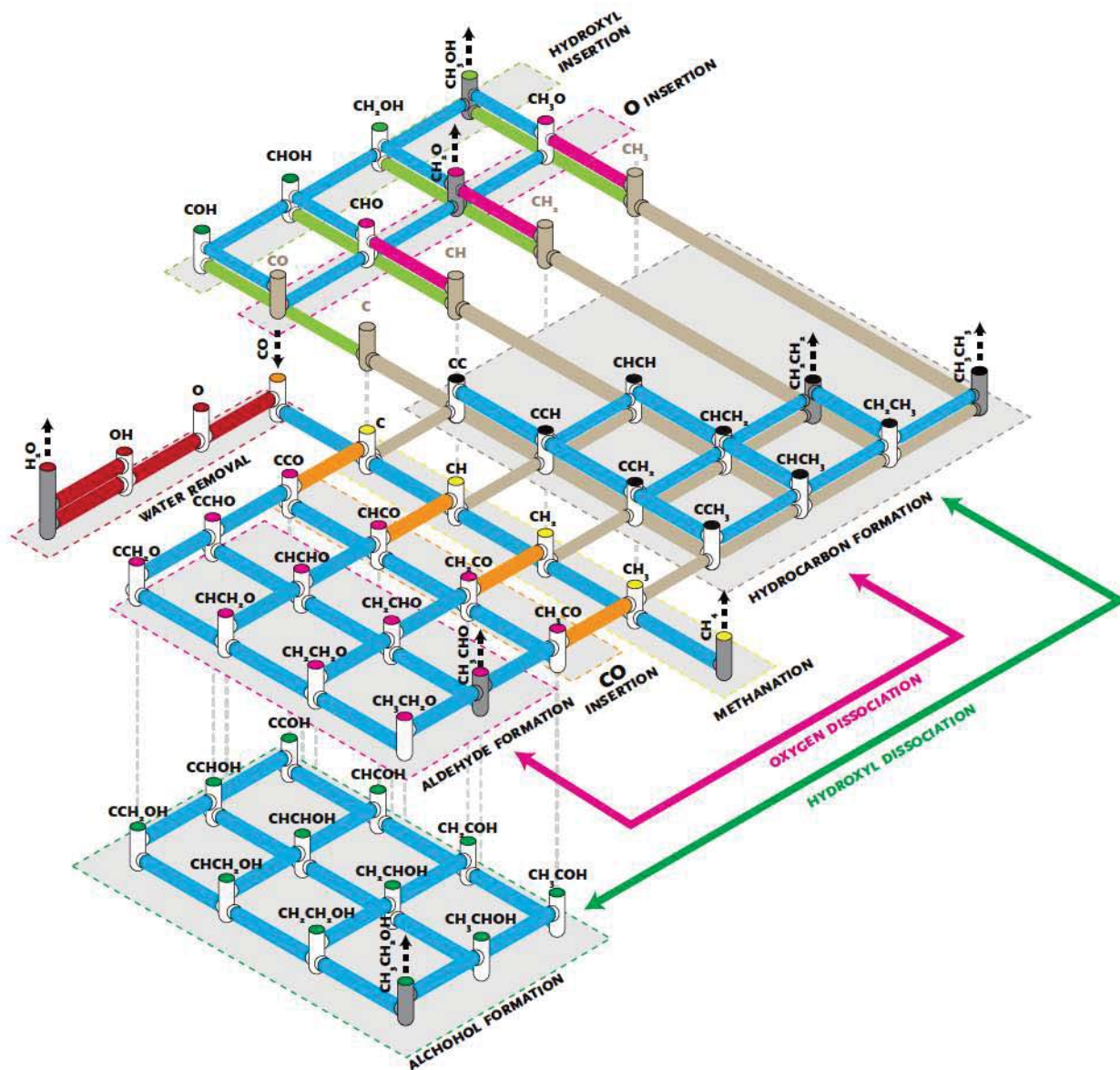


Figure 5: Different C_1 and C_2 products with corresponding pathways for the FT reaction on rhodium (by courtesy of Ir. Ivo A. W. Filot)

The questions that need to be answered concern the CO dissociation and whether this reaction proceeds via a direct pathway, or via a hydrogen assisted pathway. With the hydrogen assisted pathway the CO is first partly hydrogenated, before the C-O bond is broken. The next question concerns the dominant pathway in the C-C coupling. Further, the production of methane is compared with the production of methanol. And finally, the formation of C_2 -oxygenates is compared to the formation of methane.

2 Theory and computational methods

2.1 Density functional theory

Density functional theory (DFT) is a theory that was developed in the sixties by the solid state physicist Walter Kohn and co-workers. DFT is an ab-initio method, which can be used to obtain the interaction potential between atoms or molecules without using any adjustable parameters. Furthermore, DFT is an exact theory for the ground state of an interacting many-particle system. In its original form, it deals with many-electron systems. Electron density is an important aspect in DFT. The theory is formulated in terms of functionals of this density. The functional that is used in this study is the Perdew-Burke-Ernzerhof potential, further denoted as PBE. This functional is called an exchange-correlation functional. An often used method within DFT for doing ab initio electronic structure calculations is the projector augmented wave method. This method allows calculations to be performed with greater computational efficiency. Within this theoretical investigation, plane-wave DFT calculations are performed in conjunction with the projector augmented wave method. This method will be further elaborated on in section 2.1.4.

The most important problem in DFT is to find accurate functionals, which are an approximation of the true potential. DFT would not have been so popular were it not for a very successful approximation of these functionals called the local density approximation, further denoted as LDA. This approximation makes it possible to relate properties of the inhomogeneous, interacting many-body systems to that of a homogeneous electron gas. Very accurate theoretical results are known for the latter, although this system cannot be realized experimentally. More about the LDA will be explained in section 2.1.2.

DFT was mostly used by physicists until the nineties in order to calculate material properties such as equilibrium crystal structures, magnetizations, cohesive energies, elastic moduli and phonon spectra. These properties are found by minimizing the total energy and non-equilibrium properties by studying the motion of the nuclei due to the forces exerted on them. These forces can then be determined from the gradients of the energy landscape.

During the last decades, DFT found its way into chemistry due to its capability to treat very large molecules, e.g. C₂₀ carbohydrates, that can be formed in the FT reaction. More importantly, the development of corrections to the LDA, so called gradient corrections, led to greater precision that made it possible for chemical reactions to be simulated in this manner.

In advanced electronic structure calculations, the Born-Oppenheimer approximation [13] is often used. This approximation states that the mass of the nuclei is more than three orders of magnitude larger than that of the electrons. So, the total Hamiltonian still has contributions from the nuclei and the electronic Hamiltonian depends

only parametrically on the nuclear coordinates. Hence, a very accurate approximation can be made by separating the motion of the electrons and the motion of the nuclei. In the Born-Oppenheimer approximation, positions of the nuclei are kept fixed and a static external potential is generated. The problem, as stated in equation 1, needs to be solved. A stationary electronic state is then described by a wavefunction Ψ , that satisfies the many-electron time-independent Schrödinger equation.

$$\hat{H}\Psi = \left[\hat{T} + \hat{V} + \hat{U} \right] \Psi \quad (1)$$

which can be written as :

$$\hat{H}\Psi = \sum_{i=1}^M \left[-\frac{\hbar^2}{2m_e} \nabla_i^2 + \nu(\vec{\rho}_i) + \frac{1}{2} \frac{e^2}{4\pi\epsilon_0} \sum_{j=1, j \neq i}^M \frac{1}{|\vec{\rho}_i - \vec{\rho}_j|} \right] \Psi \quad (2)$$

In the above mentioned quantum mechanical equation, the M stands for the interacting electrons with coordinates $\vec{\rho}$ in the external potential, $\vec{\rho}_i$, due to the interaction with the nuclei (N) with coordinates \vec{r}_k .

The external potential ($\nu(\vec{\rho}_i)$) is given by the following equation:

$$\nu(\vec{\rho}_i) = - \sum_{k=1}^M \frac{e^2}{4\pi\epsilon_0} \frac{Z_k}{|\vec{\rho}_i - \vec{r}_k|} \quad (3)$$

where Z_k is the atom number of atom k.

It is sufficient to consider only the lowest eigenvalue, i.e. the energy of the electronic ground state of this Hamiltonian from equation 2. This is valid, since it is true for most cases that the electronic excitation energies are much larger than the thermal energy at temperatures of interest.

Hohenberg and Kohn have formulated two theorems from which a functional for the energy can be obtained. The first theorem states that a non-degenerate ground state wavefunction of a system interacting electrons is a functional of the ground state density [14]. In other words, the ground state density uniquely determines the potential and thus all properties of the system, including the many-body wavefunction.

$$F[n] = T[n] + U[n] \quad (4)$$

Equation 4, also known as the "HK Functional", is a universal functional of the density that does not depend explicitly on the external potential.

Their second theorem states [14] that there exists an energy functional of the electron density that is minimal for the ground state density. If we know the energy functional of theorem 2, the ground state density is found by minimizing this functional with respect to all possible electron densities $n(\vec{\rho})$, obeying equation 5:

$$\int d\vec{\rho} n(\vec{\rho}) = M \quad (5)$$

The energy functional for the ground state energy will become:

$$E[n] = \int d\vec{\rho} n(\vec{\rho}) \nu(\vec{\rho}) + F[n] \quad (6)$$

Although the above energy functional is exact, the functional $F[n]$ is not known. However, we can split this functional in two, as shown in equation 7

$$F[n] = \frac{1}{2} \int \int d\vec{\rho} d\vec{\rho}' \frac{n(\vec{\rho}) n(\vec{\rho}')}{|\vec{\rho} - \vec{\rho}'|} + G[n] \quad (7)$$

The remaining part $G[n]$ is still unknown but smaller than $F[n]$. This problem can be solved using the Kohn-Sham theory, that will be elaborated on in the next section 2.1.1.

2.1.1 Kohn-Sham theory

The theory, as described in section 2.1, is exact but not yet very useful. Therefore, Kohn and Sham came with a theory that was more practical that turned the HK theory into a more practical perspective. Kohn and Sham [15] considered a fictitious system of non-interacting electrons in such an external potential that the corresponding density is the same as that of the system of the interacting electrons. If only the kinetic part $T_s[n]$ is considered and Ψ_s is the ground state wavefunction of the non-interacting system, the functional for $T_s[n]$ becomes:

$$T_s[n] = \langle \Psi_s | T | \Psi_s \rangle = F[n] \quad (8)$$

$G[n]$ (equation 7) of the interacting system can be split in two in the following manner:

$$G[n] = T_s[n] + E_{xc}[n] \quad (9)$$

The most remarkable aspect of this outcome is that $T_s[n]$ is the kinetic energy of the non-interacting system at the same density $n(\vec{\rho})$ as that of the interacting system. The remaining functional is called the exchange-correlation energy functional. This exchange-correlation functional can be approximated by the LDA, which will be further elaborated on in section 2.1.2

2.1.2 LDA

In the local density approximation, the exchange-correlation energy functional of the inhomogeneous, interacting electron system is approximated as given in equation 10

$$E_{xc}[n] \approx \int d\vec{\rho} \epsilon_{xc}(n(\vec{\rho})) n(\vec{\rho}) \quad (10)$$

In the above-mentioned equation, $\epsilon_{xc}(n(\vec{\rho}))$ is the exchange-correlation energy per electron of a homogeneous electron gas, with a density equal to the local density that is

denoted as $n(\vec{\rho})$.

One setback of the LDA that this approximations cannot repair is the incorrect description of the London dispersion interaction [16], which is approximately proportional to $\frac{1}{r^6}$ at large distances.

In the LDA, two molecules or atoms can only "feel" each other if they have overlapping electron densities. However, London Dispersion interaction is caused by correlated movement of electrons in separate atoms or molecules by mutually induced dipoles. This occurs without such overlap that is needed in the LDA. The potential on a molecule depends on the electron density at a completely different place. This phenomenon is also present in the generalized gradient approximations (GGA).

2.1.3 Generalized Gradient Approximations

Another approximation that is made is the GGA. The LDA is exact for a homogeneous electron gas, for which the gradient of the density equals zero. The exchange-correlation potential of an inhomogeneous electron gas can be expanded in gradients of density. The GGA is in essence an extension to previously proposed LDA. The zeroth order of this expansion is the LDA. The first order vanishes because of symmetry. Various expressions have been given for the higher orders in this expansion. All these expansions combined are called the GGAs. These approximations have the capability to predict binding energies of molecules with required precision in the quantum chemistry. The GGA that is used in this study is the PBE functional.

2.1.4 Projector augmented wave method

In order to efficiently solve the one-electron Schrödinger equation, a basis set has to be chosen that is well adapted to the problem. In this case we deal with periodic systems. Therefore, a plane wave basis set is commonly used. Plane waves are well suited for the cases in which wavefunctions do not have a sharp positional dependence. However, the electrons in the innermost shells of the nuclei, the core electrons, have wavefunctions that do vary on short length scales. On the other hand, these core wavefunctions are not very different from those in the isolated atoms. Therefore, it makes sense to exclude these wavefunctions from our description and to concentrate on the outermost electrons, the valence electrons, only. These electrons are responsible for the chemical properties. However, the valence electron wavefunctions have sharp variations in the core region because they should be orthogonal to the core wavefunctions. The problem is solved by replacing the true potential by a pseudopotential and the true valence wavefunction by a pseudowavefunction, that is smooth in the core region. In such methods all the information is lost about the real wavefunction close to the nuclei. The construction of pseudopotentials is also not unique and there is no systematic way to generate good pseudopotentials.

A combination of pseudopotentials with the augmented wave method was introduced by Blöchl [17] in 1994, as an extension of both methods. This method divides the all-

electron wavefunction into a pseudowavefunction, that consists of a part that approximates the free electrons in the solid, using plane waves and a part that approximates the electrons density near the core, using pseudopotentials. There is an additional correction needed because of the difference in overlap between the two regions. A schematic overview of the the projector augmented wave method is shown in figure 6.

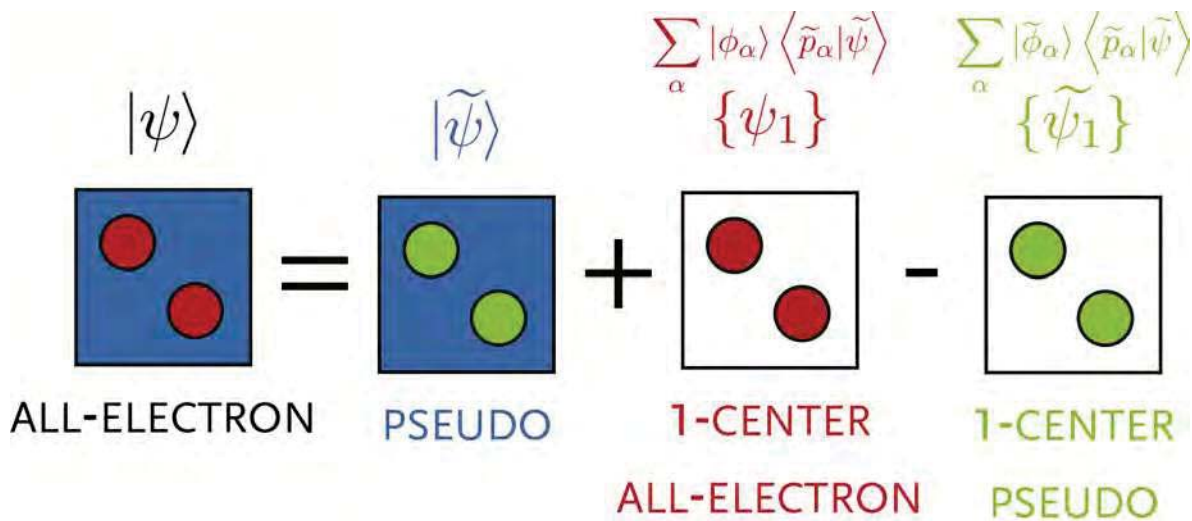


Figure 6: Schematic overview of the PAW method (by courtesy of Ir. Ivo A. W. Filot).

2.2 Kinetics

Kinetics describe the rate of a chemical reaction in relation to concentrations, pressure, and temperature. For the understanding of a reaction mechanism in catalysis, we have to make sure to measure intrinsic reaction rates. In other words, we need to understand the kinetics at the catalytic surface. However, all the observations we can make are macroscopic. We can measure extrinsic reaction rates but we are not able to measure intrinsic ones. In order to understand the intrinsic kinetics, we have to be sure that there are no mass-transfer limitations. These limitations exist between the bulk and the surface of the catalyst.

There are several proposed mechanisms by which bimolecular surface reactions can occur on surfaces, for instance the Langmuir-Hinshelwood mechanism and the Eley-Rideal mechanism. These mechanisms are further elaborated on in sections 2.2.3 and 2.2.4 respectively.

2.2.1 Adsorption

Adsorption on the surface is the first step in every heterogeneous catalytic reaction. This can occur in two different ways, specifically via dissociative adsorption or associative adsorption. A_2 will be taken as a textbook example for explaining these differences.

With dissociative adsorption, the molecules dissociate before they are adsorbed onto the surface:



Dissociative adsorption is often found in molecules like H_2 and O_2 that almost immediately dissociate upon adsorption.

With associative adsorption, the molecules are first adsorbed onto the surface and dissociate when they are on the surface, in the following manner:



Both types of adsorption are found when looking at the Fischer-Tropsch synthesis reaction. CO adsorbs in a associative way, while H_2 adsorbs in a dissociative manner.

2.2.2 Bond order conservation principle

With the formation of the chemical bond between the surface and the adsorbate, there is not only a change in the electron distribution on the adatom itself. Also the interaction between the surface atoms weakens. This can be described by the bond order conservation principle.

The bond order conservation theory is an empirical correlation of the activation energy for dissociative adsorption from the heats of the reaction. In Shustorovich's approach, empirical parameters are used for the heat of adsorption of atoms and bond strengths of the molecules in the gasphase. According to covalent bonding theory [18], the bond order decreases with longer distance, increases with shorter distance, and equals to 1 for the equilibrium distance. This bond order can be calculated in the following manner:

$$x = e^{-\frac{r-r_0}{a}} \quad (11)$$

If the 2-center interaction is described [19] via a Morse potential, a simple relationship between the bond order and the potential then becomes:

$$Q_i(r) = -Q_0 (2x - x^2) \quad (12)$$

Here, Q_0 is the equilibrium bond strength of a single bond. This assumption implies: Firstly, if atom A has n neighbors instead of 1, the bond strength becomes:

$$Q(n) = \sum_{i=1}^n Q_i \quad (13)$$

The bond strength Q can be expressed as a sum of two-body interactions. Secondly, the total bond order is conserved:

$$x(n) = \sum_{i=1}^n x_i = x_0 = 1 \quad (14)$$

If the bonds are equivalent, then it follows that:

$$x_i = \frac{1}{n} = e^{-\frac{r-r_0}{a}} \quad (15)$$

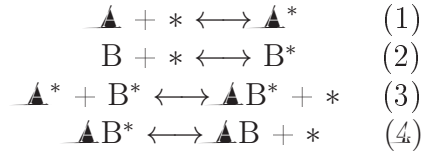
and the bond length increases compared to its value at lower coordination. If equation 15 is inserted in 12, the following equation is acquired:

$$Q(n) = -Q_0 \left(2 - \frac{1}{n} \right) \quad (16)$$

From equation 16 we can see that the bond order strength increases less than proportionally with n. The Bond order conservation holds quite well in systems that mainly have covalent bonds.

2.2.3 Langmuir-Hinshelwood mechanism

With Langmuir-Hinshelwood kinetics, all species are assumed to be adsorbed and in thermal equilibrium with the surface, before any reaction takes place. An example of such a mechanism can be the reaction of A with B, as described by the following elementary reaction steps:



For each elementary reaction step (1-4), it is now possible to write down a corresponding rate equation:

$$r_1 = k_1^+ p_A \Theta_* - k_1^- \Theta_A \quad (17)$$

$$r_2 = k_2^+ p_B \Theta_* - k_2^- \Theta_B \quad (18)$$

$$r_3 = k_3^+ \Theta_A \Theta_B - k_3^- \Theta_{AB} \Theta_* \quad (19)$$

$$r_4 = k_4^+ \Theta_{AB} - k_4^- p_{AB} \Theta_* \quad (20)$$

In the equations above, k stands for the corresponding rate constants of the forward and backward reactions and p stands for the partial pressure of a gaseous compound. Θ_R is the fraction of the sites that are occupied by molecule R, in this case A, B or AB while Θ_* stands for the empty sites. Therefore, Θ_* can be calculated in the following manner:

$$\Theta_* = 1 - \Theta_A - \Theta_B - \Theta_{AB} \quad (21)$$

2.2.4 Eley-Rideal mechanism

Another possible mechanism is the Eley-Rideal mechanism, in which one of the reactants react directly out of the gasphase, without being accommodated at the surface. This happens, for instance, with the atomic hydrogen in the gasphase together with atomic hydrogen on the surface. These hydrogen atoms are fairly active. Therefore,

the reaction takes place immediately. Because the hydrogen molecule does not adsorb strongly to the surface, the molecule will desorb instantaneously. With the exception of this example, Eley-Rideal mechanisms are very rare. Therefore, we assume the Langmuir-Hinshelwood mechanism throughout this thesis.

2.2.5 Method of working

There are several steps needed for the elucidation of a mechanism of a reaction on a catalytic surface. A schematic overview of these steps can be found in figure 7.

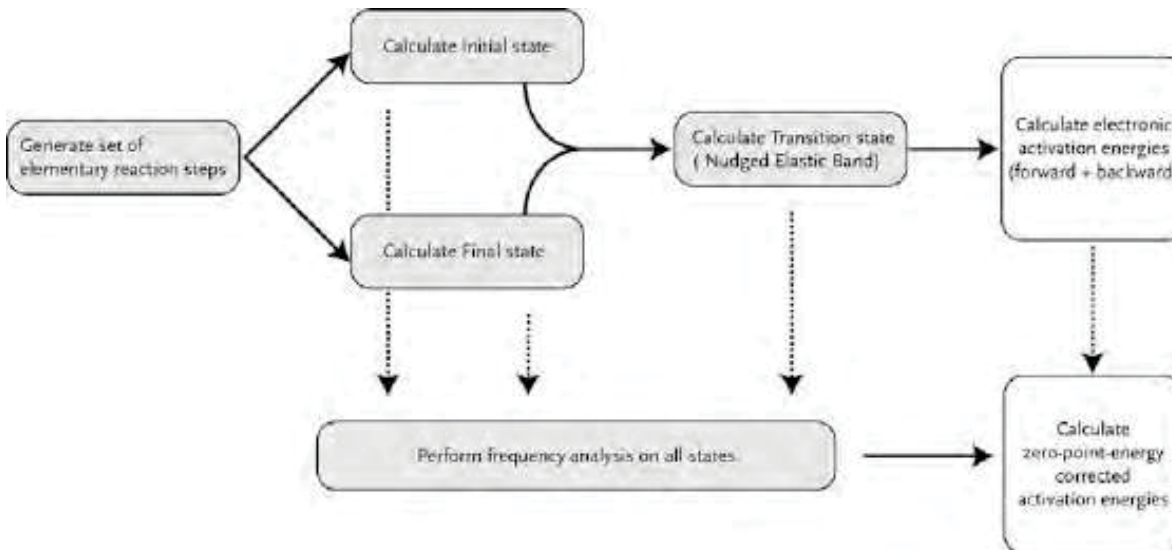


Figure 7: Method for obtaining the necessary parameters of a micro kinetic model (by courtesy of Ir. Ivo A. W. Filot).

First, the elementary reaction steps need to be determined. A list of elementary reactions, together with their kinetic parameters, can be found in tables 13 to 27 in section 8. In order to find corresponding energies with these pathways, the forward and backward reaction energy barriers need to be calculated. This is done by calculating the energy levels of the initial state, transition state, and final state. For the determination of the initial state, two different cells with the adsorbed molecules were calculated individually. This is called a migration correction. The calculations were done on a Rh(211) (3 by 2) cell. This cell was minimized in energy before adsorptions were calculated. For final state calculations, the minimum energy of the final reactant of each elementary reaction step was calculated. With these minimized initial and final states, a transition state could be determined, using the nudged elastic band method, further denoted as NEB method. This NEB method is further elaborated on in section 2.2.6.

Next, frequency analyses can be performed on the calculated initial, transition, and final states. These frequency calculations can be used to make the zero-point energy (ZPE) corrections and to calculate the pre-exponential factors. In fact, this probes the

curvature in all configurational directions from which the vibrational degrees of freedom are inventoried. From this, the ZPE correction to the electronic activation energies can be determined.

These ZPE corrections are in the same range as the typical accuracy of a DFT calculation, so neglecting this correction can lead to inaccurate results. It is even more important to take this correction into account when dealing with gasphase species. Here, the differences between the ZPE corrected and non corrected values is even greater.

What still needs to be done is to find a way to calculate the rate constants, that are needed in the microkinetic modeling. This can be done by using the partition functions corresponding to the configurational degrees of freedom in these states. To compute the rate constant for a particular elementary reaction step, the Eyring equation is used. This will be further explained in section [2.3.2](#).

2.2.6 Nudged Elastic Band method

The nudged elastic band method is used to find reaction pathways. With this method, it is possible to calculate not only the minimum energy pathway for any given chemical process, but also to determine the transition state configuration at the saddle point. In the NEB method, a minimization of an elastic band is carried out where the perpendicular component of the spring force and the parallel component of the true force are projected. An intuitive way of thinking about this method is that each image is hanging from its higher energy neighbor, trying to get in a low as possible energy. Because each image is dependent on its neighbor, the band hangs stably down from the saddle point [20].

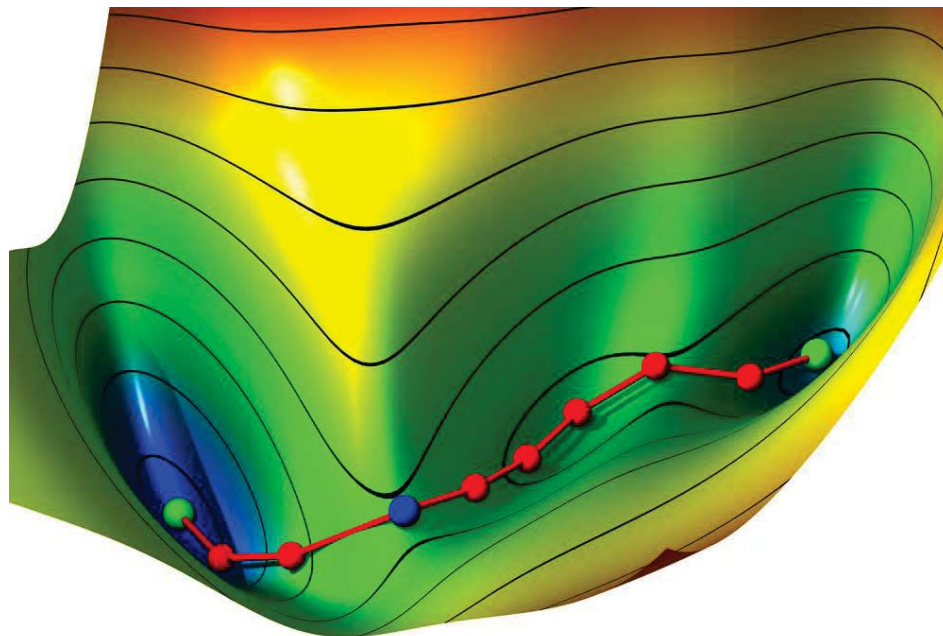


Figure 8: A graphical representation of a nudged elastic band method calculation. Here the green spheres represent the initial and final states. The red spheres show the minima towards the transition state, which is represented by a blue sphere (by the Kästner group of computational Biochemistry). [21]

Because the NEB method is a two ended search method, it is important that every atom in the initial state maps to every atom in the final state, which is the case because the method treats each atom as a distinguishable atom. When atoms are not mapped correctly, the NEB will calculate a barrier, resulting in a less favorable or improbable minimum energy pathway. In the worst case, the structure as submitted can explode.

2.3 Microkinetic modelling

Microkinetic modeling is used to model transient behavior and temperature effects of the various species in a chemical system. The reaction constant for each elementary reaction step is expressed in the Arrhenius formula.

$$k = \nu \exp\left(-\frac{E_a}{k_b T}\right) \quad (22)$$

Microkinetic modeling is a type of analysis of reaction kinetics. It attempts to incorporate the basic surface chemistry involved in the catalytic reaction. This kinetic model is based on a description of the catalytic process in terms of information and assumptions about the active sites and the nature of elementary reaction steps that may comprise the reaction scheme [22]. The starting point is the formulation of the elementary chemical reaction steps that capture the essential surface chemistry.

The key difference of microkinetic analysis compared to kinetic analysis, is the lack of initial assumptions made about kinetically significant steps and most abundant species. Instead, estimations of the rates of elementary reactions and surface coverages are a result of the analysis.

There are several parameters needed for microkinetic modeling. Sticking coefficients are used to describe the ratio of the number of adsorbate atoms or molecules that "stick" to the surface to the total number of atoms that impinge upon the surface during the same period of time. This coefficient is between 1 (when all impinging atoms stick to the surface) and 0 (when no atoms stick to the surface). This sticking coefficient depends on the temperature, surface coverage, and the kinetic energy of the impinging particles. Also, some information about the active site is needed as well as the surface bond, the pre-exponential factors, and the activation energies for surface reactions.

These parameters are based on multiple theories, specifically the transition state theory, the bond order conservation principle, and the Brønsted-Evans-Polanyi or BEP relation. These are further explained in section 2.3.2, section 2.2.2, and section 2.3.3 respectively.

2.3.1 Hertz-Knudsen reaction kinetics

MKMCXX [23], an in-house written program, was used for microkinetic modeling. Next to Arrhenius kinetics, it also employs Hertz-Knudsen kinetics. Hertz-Knudsen kinetics give a more realistic simulation because the pre-exponential factors become a function of temperature.

The pre-exponential factor for adsorption ($k_{adsorption}$) is now given as:

$$k_{adsorption} = \frac{A_{site}}{\sqrt{2\pi mk_b T}} S \quad (23)$$

In the afore mentioned equation, A_{site} stands for the area of the adsorption site, m for the mass of the molecule, k_b for the Boltzmann constant, T for the temperature, and S for the sticking coefficient.

The pre-exponential factor for desorption ($k_{desorption}$) is calculated in the following manner:

$$k_{desorption} = A_{site} \frac{k_b T^3}{h^3} \frac{2\pi mk_b}{\sigma \Theta_{rot}} \exp\left(\frac{-E_{des}}{RT}\right) \quad (24)$$

In the pre-exponential factor for the desorption, more parameters are taken into account than for the adsorption. σ stand for the symmetry number, Θ_{rot} for the characteristic temperature for rotation, E_{des} for the desorption energy, and R for the gas constant.

2.3.2 Transition state theory

The Eyring equation [24], as seen in equation 25, is used for the calculation of rate constants for elementary reaction steps.

$$k = \frac{k_b T}{h} \frac{Q^\ddagger}{Q} \exp\left(\frac{-\Delta E_{act}^{zpe-corrected}}{k_b T}\right) \quad (25)$$

Here, k_b is the Boltzmann's constant in J per Kelvin, k the reaction rate of an elementary reaction step, T the temperature in Kelvin, and h is Planck's constant in J per second. $\Delta E_{act}^{zpe-corrected}$ is the ZPE corrected activation energy in J per particle. Q^\ddagger and Q are the total partition functions of the transition state and initial state, respectively. It must be noted that the transition state has one imaginary frequency, which is not included in Q^\ddagger .

The molecular partition function for a gasphase species is a product of contributions from translational, vibrational and rotational degrees of freedom. The total partition function can be calculated as follows:

$$Q_i = q_{i,trans} q_{i,vib} q_{i,rot} \quad (26)$$

where $q_{i,trans}$, $q_{i,vib}$ and $q_{i,rot}$ are given as 27, 28 and 29 respectively.

$$q_{i,trans} = \frac{(2\pi m_i k_b T)^{\frac{3}{2}}}{h^3} \quad (27)$$

$$q_{i,vib} = \prod_j \frac{1}{1 - \exp\left(-\frac{h\nu_{ij}}{k_b T}\right)} \quad (28)$$

$$q_{i,rot} = \frac{8\pi^2 I_i k_b T}{h^2} \quad (29)$$

Where I_i is the moment of inertia, σ_r is the rotational symmetry number, and ν_{ij} stands for the frequencies of normal modes of vibration.

2.3.3 Brønsted-Evans-Polanyi relation.

The BEP relation observes that there is a linear relationship between the activation energy between two reactions of the same class proportional to the difference of their enthalpy of reaction [25,26]. This relation can be expressed as:

$$\Delta E = -\alpha \Delta H \quad (30)$$

where α characterizes the transition state along the reaction coordinate and always has a value between 0 and 1. If α is approximately 1, there is a late transition state, which means that the transition state structure has a great similarity in geometry with the final state. When α is approximately 0, the transition state is early and its structure

lies close to that of the reactants. ΔH is the enthalpy of the reaction and ΔE is formulated in the following manner:

$$\Delta E = -E_0 - E_a \quad (31)$$

In the equation above, E_a stands for the activation energy, where E_0 stands for the activation energy of a reference reaction from the same class. With this relationship, activation energies of many reactions within the same class, i.e. on the same active site and type of reaction but on for instance another metal can be calculated.

2.3.4 Degree of rate control

The rate-limiting and rate-inhibiting steps can be determined using Campbell's Degree of Rate Control methodology [27]. The amount of rate control of a particular chemical reaction step can be calculated by:

$$\chi_i = \left(\frac{\delta \ln(r_j^+)}{\delta \ln(k_i^\pm)} \right) \quad (32)$$

In this equation, χ_i is the degree of rate-control of elementary reaction step i and k_i^\pm the rate constant of the elementary reaction step i in both forward and backward direction. In other words, this means that the effect of increasing both the forward and the backward rate of a particular elementary reaction step with regard to the forward reaction rate of the key-compound is probed. If χ_i is positive, the elementary reaction step is a rate-limiting step and decreasing the transition state would result in an increase of the overall reaction rate. If χ_i is negative, the particular elementary reaction step is rate-inhibiting, while decreasing the activation energy in both directions would result in a decrease of the overall reaction rate. For any stable point in phase-space, the sum of all χ_i must be 1.

3 Computational details

The DFT calculations were performed using the Vienna ab Initio Simulation Packages (VASP) version 4.6.38. Projector augmented wave (PAW) potentials were employed to describe the interaction between ions and electrons. Exchange correlation was described using Perdew-Burke-Ernzerhof (PBE) parametrization of the generalized gradient approximation (GGA). The wave functions were expanded in the plane wave basis up to a kinetic energy of 400 eV. The partial occupancies were set using the second order occupation function of Methfessel and Paxton [28], using a width of 0.2 eV for the smearing. Calculations are stopped when the energies are converged. The maximum number of electronic steps for the initial, transition, and final state calculations were set to 40. The maximum number of electronic steps for the frequency calculations was set to 100. Not all degrees of freedom were allowed to change. The ions were allowed to relax, while the cell shape and volume were not allowed to change. A quasi-Newton variable metric algorithm was used to relax the ions into their instantaneous ground-state. This method was used for the calculation of the initial, transition, and final states. For the frequency calculations, the vibrational frequencies of the system and the Hessian matrix were determined. The Hessian matrix is a matrix of the second derivatives of the energy with respect to the atomic positions, which was calculated in all three directions. This was done for the adsorbates only, not for the Rhodium atoms. For initial and final state calculations, the POTIM was set to 0.5. The POTIM was set to 0.02 for transition state and frequency calculations. For the sampling of the Brillouin zone, an automatic k-mesh generation of 7 x 7 x 1 k-points was used. The fully automatic scheme generated $\sqrt{2}$ centered Monkhorst-Pack grids, with a subdivision of 7 7 1 along the reciprocal lattice vectors N1, N2, and N3, respectively. The numbers of subdivisions along each reciprocal lattice vector are represented as follows:

$$N_x = \max(1, l * |\vec{b}_x| + 0.5) \quad (33)$$

where x is 1 to 3.

Binding energies ($E_{binding}$) for the adsorbents were calculated as follows:

$$E_{binding} = E_{total} - E_{surface} - 2 * E_{molecule} \quad (34)$$

Where E_{total} refers to the total energy of the system, $E_{surface}$ to the metal slab energy, and $E_{molecule}$ to the adsorbents' gasphase energies. All of these energies are zero-point energy corrected. Note that on two sides of the metal slab, an adsorbent is adsorbed, so the gasphase energies need to be subtracted twice in order to get the correct binding energies.

The migration corrected activation energies for the forward (E_a) and backward (E_b) reactions are calculated as follows:

$$E_a = \frac{E_{TS} + E_{surface} - E_{adsorbent1} - E_{adsorbent2}}{2} \quad (35)$$

in which $E_{adsorbent1}$ and $E_{adsorbent2}$ both represent the energy of one of the reacting adsorbents, placed on the surface individually, and E_{TS} represents the energy of the transition state. 96.25 is the conversion factor from eV to kJ.

$$E_b = \frac{E_{TS} - E_{adsorbent}}{2} \quad (36)$$

The metal slab contained four layers with a vacuum regime of 7.5 Å on both sides. This distance suffices to avoid interactions between the adsorbates from different slabs. All transition states were found using the nudged elastic band method. Zero point energy corrections were performed by a selective dynamics run, in which only the adsorbents were allowed to vibrate. The zero point energy was then determined by adding the total energy contribution of the frequencies divided by two, to the lowest energy of the adsorbent. Imaginary frequencies from the transition state were not taken into account in this correction.

In order to determine the pre-exponential factors, frequency analyses were performed, using the following equation:

$$f = \frac{1}{1 - e^{\left(\frac{-\omega}{k_b T}\right)}} \quad (37)$$

where f stands for the vibrational partition function, ω for the frequency of the vibrational mode in meV, k_b for Boltzmann's constant in meV K⁻¹, and T for the temperature in Kelvin. For the forward pre-exponential factor, the following equation was performed:

$$\nu_f = \frac{f_{TS} k_b T}{f_{IS} h} \quad (38)$$

where ν_f is the pre-exponential factor for the forward reaction, f_{TS} is the the frequency for the transition state reaction and f_{IS} the frequency for the initial state. The temperature was set to 800K.

In order to objectively compare the energies from DFT with the energies found in experiments, the enthalpy of reaction was calculated for the formation reactions towards the different possible reaction products. The standard enthalpy of reaction $\Delta_r H^\theta$ is related to the standard enthalpy of formation $\Delta_f H^\theta$ of reactants and products by the following equation:

$$\Delta_r H^\theta = \sum_{\text{products}} \nu \Delta_f H^\theta - \sum_{\text{reagents}} \nu \Delta_f H^\theta \quad (39)$$

The standard enthalpies of formation yield a standard enthalpy of reaction at 298 K and 1 bar. Enthalpies at different temperatures can be calculated from heat capacities and reaction enthalpies at these temperatures. The thermodynamic analysis for the methanation reaction is shown as an example in figure 9.

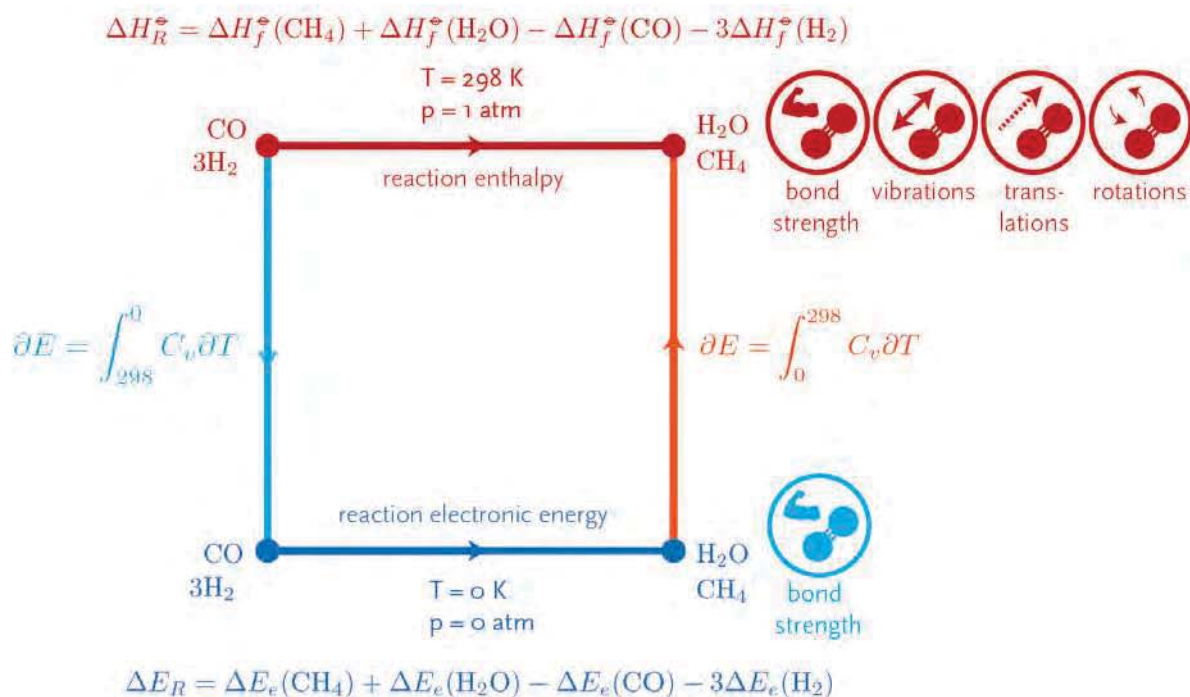


Figure 9: Thermodynamic analysis of the methanation reaction (by courtesy of Ir. Ivo A. W. Filot).

It must be noted that the values of DFT are at 0 K and 0 bar, while the values from experiments are measured under standard conditions. Hence, there will be a difference between these experimental values and DFT, which is partially due to this difference in temperature and pressure. The rest of the difference in energy is due to the accuracy of DFT.

4 Results and Discussion

4.1 DFT calculations

4.1.1 Adsorption and desorption reactions

First of all, the adsorption and desorption reaction energies were determined for the relevant $C_xH_y(O_z)$ species. Reagents as well as products were investigated, as the result of CO hydrogenation, C-C coupling, and CO insertion reactions. Table 1 gives an overview of these reagents and products with their corresponding values.

Table 1: Energies for adsorption. E_{ads} stands for the adsorption energy, in kJ/mol.

| Adsorption and Desorption Reactions | E_{ads} [kJ/mol] |
|--|--------------------|
| $H_2 + 2 * \rightleftharpoons 2 H^*_{2}$ | 118 |
| $CO + * \rightleftharpoons CO^*$ | 194 |
| $H_2O^* \rightleftharpoons H_2O + *$ | 47 |
| $CH_2O^* \rightleftharpoons CH_2O + *$ | 99 |
| $CH_3OH^* \rightleftharpoons CH_3OH + *$ | 26 |
| $CH_2CH_2^* \rightleftharpoons CH_2CH_2 + *$ | 87 |
| $CH_3CHO^* \rightleftharpoons CH_3CHO + *$ | 87 |
| $CH_3CH_2OH^* \rightleftharpoons CH_3CH_2OH + *$ | 15 |

Note that due to the associative desorption of methane and ethane, they are not taken into account with Hertz-Knudsen desorption . The adsorption energies for the reagents are in line with previous results from the Literature [29].

4.1.2 CO dissociation reactions

The CO dissociation reaction is an important reaction in the FT synthesis reaction. This reaction is key to the production of methane and longer hydrocarbons as well as the proposed reactions towards ethanol or other longer oxygenates. CO dissociation can occur in multiple ways. It can occur either directly, where the adsorbed CO splits into C and O, or via a hydrogen assisted route, where the adsorbed CO first reacts with an adsorbed hydrogen atom before splitting of the CO bond. This Hydrogen mediated CO dissociation can also occur via two pathways, namely the reaction via COH or the reaction via CH_xO intermediates. The pathways towards adsorbed CH_2 and OH are shown in figure 10. All reaction intermediates for CO dissociation are shown in table 12 and 13 in chapter 8.1.

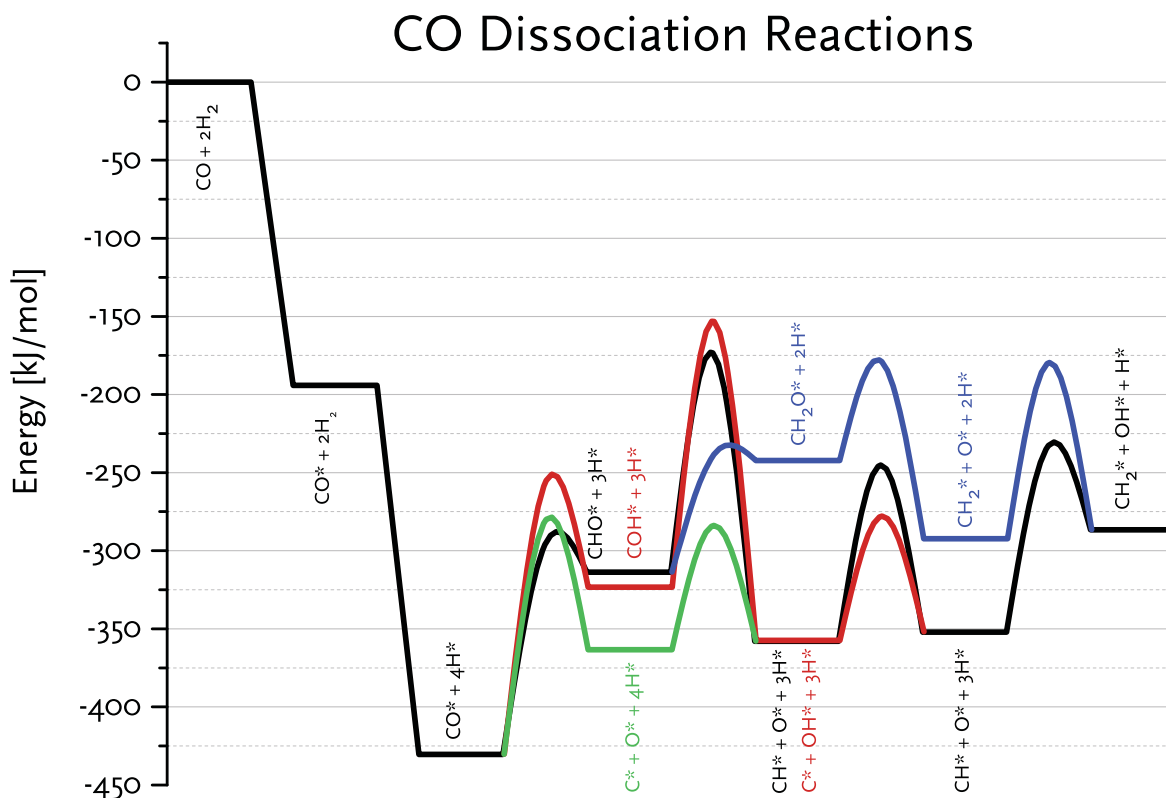


Figure 10: Reaction energy diagram of the different possible CO dissociation reactions.

From figure 10 it can be seen that CO dissociation is most likely to go via a direct pathway and not via a hydrogen mediated pathway. The same trend was also found for the CO dissociation on stepped ruthenium [30]. Even though the dissociation energy is lower for the CHO dissociation to CH and O than the direct CO dissociation to C and O, the overall energetic barrier for the hydrogen mediated CO dissociation is much higher. Another alternative path was investigated, where the CO was hydrogenated on the O rather than on the C, which results in a COH intermediate. Subsequently, this intermediate can split into C and OH. This was proposed for Ni surfaces in the Literature [31]. The initial hydrogenation step to form this COH intermediate has a barrier of 175 kJ/mol. The COH dissociation reaction to C and OH has a similar energy barrier, making this reaction the least favorite pathway for CO dissociation on stepped rhodium. This contrasts to the CO dissociation on a terrace site, at which the CO dissociation tends to happen in a hydrogen mediated manner on ruthenium [32] as well as on rhodium [33]. Table 2 shows the comparison between activation energies from own calculations, compared to the Literature [29,34].

Table 2: Elementary reaction steps as calculated for the direct and hydrogen assisted CO dissociation reactions from own calculations^a as well as from the Literature [29]^b [34]^c. E_f stands for the forward reaction energy and E_b for the backward reaction energy. All energies are in kJ/mol.

| # | Elementary Reaction Steps | E_f^a | E_b^a | E_f^b | E_b^b | E_f^c | E_b^c |
|---|--|----------|----------|----------|----------|----------|----------|
| | | [kJ/mol] | [kJ/mol] | [kJ/mol] | [kJ/mol] | [kJ/mol] | [kJ/mol] |
| 1 | $\text{CO}^* + * \rightleftharpoons \text{C}^* + \text{O}^*$ | 150 | 83 | 150 | 127 | 180 | 96 |
| 2 | $\text{CO}^* + \text{H}^* \rightleftharpoons \text{COH}^* + *$ | 175 | 68 | 106 | 27 | 94 | 11 |
| 3 | $\text{CO}^* + \text{H}^* \rightleftharpoons \text{CH}^* + \text{O}^*$ | 134 | 18 | 96 | 29 | 109 | 36 |
| 4 | $\text{CH}^* + * \rightleftharpoons \text{CH}^* + \text{O}^*$ | 140 | 185 | 98 | 93 | 184 | 192 |
| 5 | $\text{COH}^* + * \rightleftharpoons \text{C}^* + \text{OH}^*$ | 170 | 204 | 102 | 109 | 115 | 139 |

It can be seen from table 2 that the forward and backward reaction energies differ enormously. This difference is due to the stabilities of certain species and their corresponding transition state. Literature value on the forward and backward activation energy predict a significantly (around 40 kJ/mol) more stable CHO intermediate, suggesting a feasible hydrogen assisted CO dissociation, which is in contrast to our findings. A detailed RED analysis of their results shows that their migration correction is not totally correct. This is further elaborated on in section 4.1.4. This can also, to lesser extent, be the case for the COH species. It can also be seen that the forward reaction energy of the CO dissociation is the same, while the backward reaction energy differs with 44 kJ/mol. This means that we have found an easier way to produce CO out of C and O. It can further be noted that the activation energy for dissociation of CHO to CH and O lies in between the values found in the Literature. The reaction energy in the Literature is found to be rather thermo-neutral, while the reaction energy from own calculation is endothermic. This is also due to the existence of a more stable state for CHO. The forward reaction energy would then increase. If the reaction is made thermo-neutral, the values for the dissociation would be close to that of the values found by Kapur and coworkers [34]. The splitting of COH to C and OH is endothermic in both the Literature, as well as in own calculations. This means that it is possible to decrease both forward and backward reaction energy, going via a different splitting pathway. From this it can be concluded that there must be a transition state that is energetically more favorable. If only the transition state decreases in energy, the reaction energy will stay the same, while the energy barriers decrease.

Figure 11a to 11e show the transition states of reactions 1 to 5. Figure 11c to 11e show the direct and indirect CO dissociation reactions. The CO dissociation takes place on the B5-site. From figure 11a, it can be seen that the oxygen in this configuration is hard to hydrogenate. There may be a different pathway for the formation of the COH species since this reaction is more favorable, as described by Kapur and coworkers. It could be the case that hydrogen is on the step, while CO is in the step. In this manner, it may be easier to hydrogenate the oxygen. The low activation barrier for the backward reaction in reaction 3 can be explained by its transition state. The transition state from reaction 3, as shown in figure 11b, is much alike the final state. Therefore,

it is relatively easy to go from the final state to the transition state, explaining the low backward activation energy. It is shown in figure 11d and 11e that the splitting of the O and the splitting of the OH proceeds via one atom in approximately the same manner. While C is bound to the surface with three bonds, the CH is bound by the surface by two bonds and with one bond to the hydrogen atom. This is according to the bond order conservation principle. The oxygen from transition state 4 will move to a bridged position, which is also in line with the bond order conservation principle.

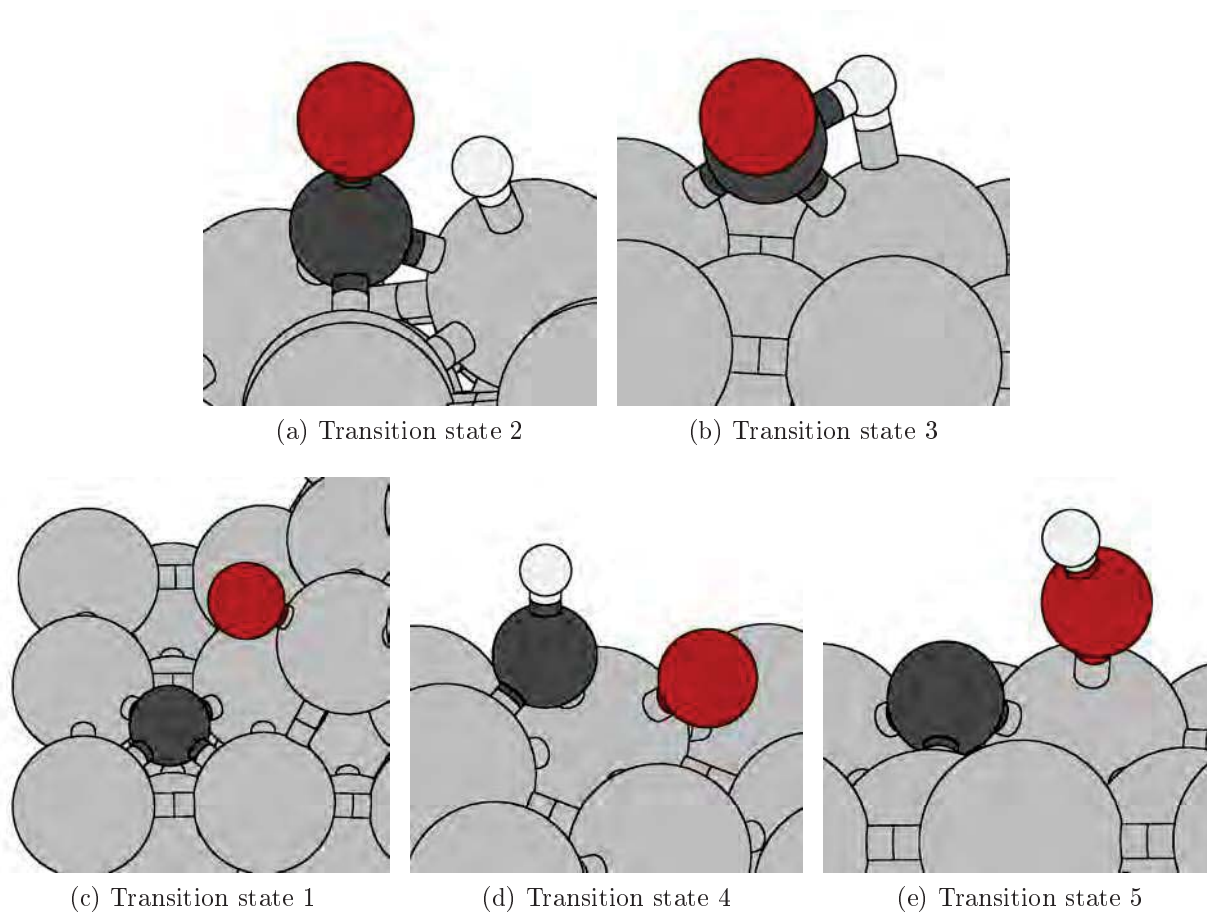


Figure 11: Graphical representation of transition states 2 to 5.

4.1.3 The Methanation reaction

Methane is one of the products that can be formed using the FT reaction on rhodium. The methanation reaction is an important reaction in Rh-based FT, as it is known that methane is the dominant product [35–39]. The methanation reaction can also be used as a good test case for a microkinetic model since the reaction deals with CO dissociation, hydrogenation, and the removal of oxygen by the production of water. On a stepped rhodium surface, CO dissociation is neither easy nor difficult. Hence, a certain amount of the CO on the surface will become dissociated into C and O. Subsequently, the adsorbed C can react with adsorbed hydrogen all the way through to

methane. The remaining oxygen on the surface can react with hydrogen to form OH, that can be hydrogenated again to water. Figure 12 clearly shows that the dissociation of CO is the rate limiting step in the methanation, because this energy barrier is the highest of all reactions. It is also shown that the reaction to CH_2 is rather difficult, since the reaction energy barrier is only 30 kJ/mol lower than the CO dissociation. This means that the surface will probably contain an abundance of CH species. It further shows that C hydrogenation to CH species and the O hydrogenation to OH species are almost thermo-neutral, while the rest of the reactions net need energy. The forward and backward reaction energies, as well as the pre-exponential factors for the methane formation, can be found in table 16 with according graphical representation in table 17 in section 8.3. The energies and pre-exponential factors for the formation of water can be found in table 14 with their graphical representations in table 15 in section 8.2. The total reaction energy for the formation of methane was found to be approximately 275 kJ/mol.

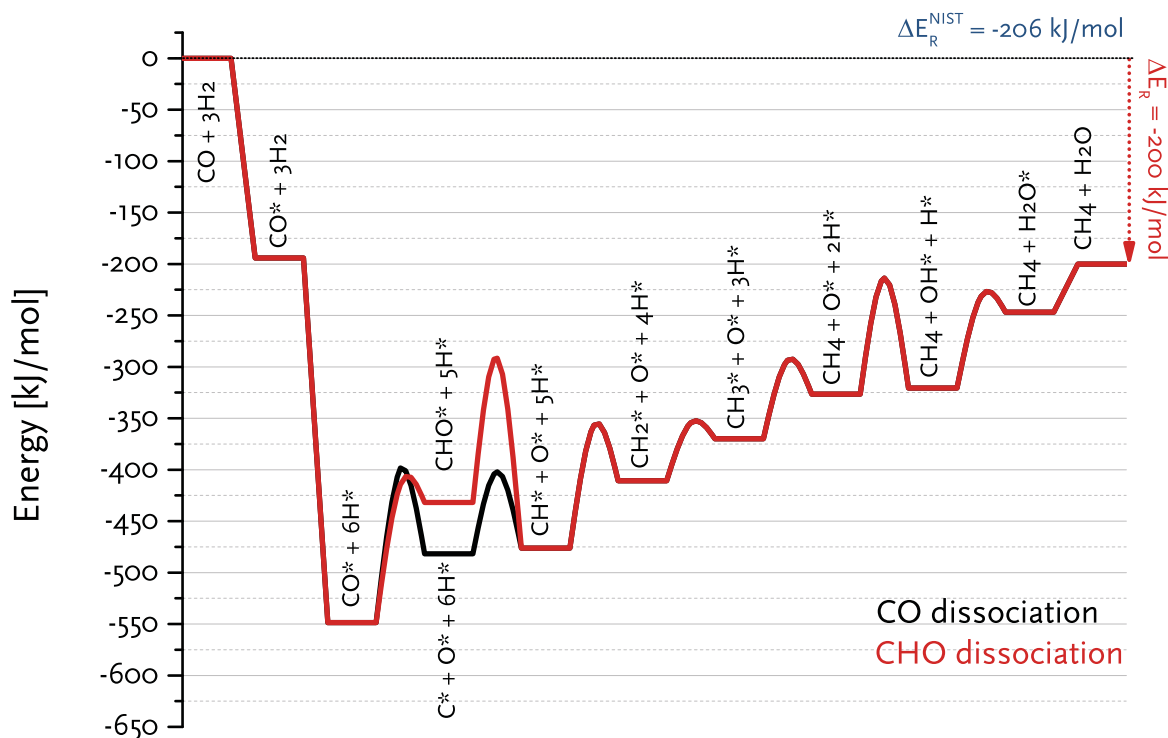


Figure 12: Reaction energy diagram direct and hydrogen assisted route for the methanation reaction.

Figure 12 compares the case of the direct CO dissociation with the hydrogen mediated CO dissociation in the methanation reaction. As discussed in section 4.1.2, the CHO has a lesser activation energy compared to the direct pathway, but has a higher overall energy barrier for the reaction to the CH species. It can further be seen that the C and CH species are relatively stable on the surface, but not as stable as CO is. The simulated reaction enthalpy nicely matches the reaction enthalpy calculated from the

formation enthalpies [40].

The comparison can also be made between the methanation reaction on rhodium and ruthenium [41]. The reaction energy diagram that compares the methanation reactions is shown in figure 13.

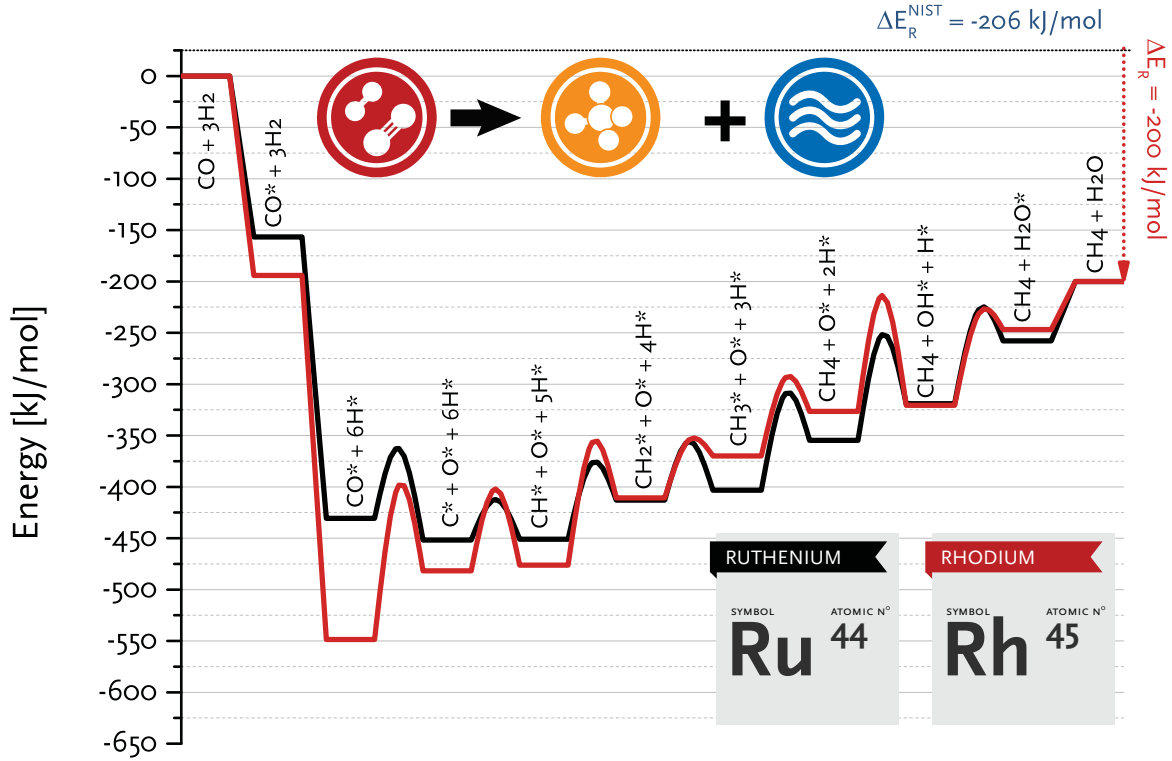


Figure 13: Reaction energy diagram for the methanation reaction on rhodium and ruthenium.

As is seen in figure 13, methanation reactions proceed via the direct CO dissociation. This figure also shows that the C hydrogenation to CH is thermo-neutral with regard to ruthenium, as was the case for rhodium. In contrast to methanation on rhodium, the CH₂ hydrogenation to CH₃ is almost thermo-neutral, whereas the O hydrogenation to OH is not. Also, the stability of the C and CH species on ruthenium, compared to the CO species is different from rhodium. On rhodium, the CO is the most stable surface species, followed by C and CH, while on ruthenium, the C and CH species are even more stable than the CO species. However, up to CH₂, the surface species are more stable on rhodium. CH₃ and O are more stable on the surface of ruthenium, while OH is more stable on rhodium. There is quite some difference in energy in the adsorption reactions as well, since both CO and H species adsorb more strongly on the rhodium surface. Table 3 shows the comparison between activation energies from own calculations, compared to the Literature [29, 42].

Table 3: Elementary reaction steps as calculated for the methanation reaction from own calculations^a as well as from the Literature [29]^b [42]^c. All energies are in kJ/mol. Data that was not calculated in the Literature is marked by a *.

| # | Elementary Reaction Steps | E_f^a | E_b^a | E_f^b | E_b^b | E_f^c | E_b^c |
|----|---|------------------------|------------------------|------------------|------------------|------------------|------------------|
| | | [kJ/mol] [own work] | [kJ/mol] [own work] | [kJ/mol] [29] | [kJ/mol] [29] | [kJ/mol] [42] | [kJ/mol] [42] |
| 9 | $C^* + H_2^* \leftrightarrow CH_2^* + *$ | 80 | 74 | 94 | 67 | 90 | 105 |
| 10 | $CH_2^* + H_2^* \leftrightarrow CH_3^* + *$ | 119 | 54 | 157 | 25 | 67 | 27 |
| 11 | $CH_3^* + H_2^* \leftrightarrow CH_4 + *$ | 16 | 56 | 115 | 60 | 59 | 92 |
| 12 | $CH_3^* + H_2^* \leftrightarrow CH_4 + 2 *$ | 76 | 33 | 112 | 40 | 71 | * |

It can be seen from table 3 that the forward and backward reaction energies do not differ enormously, comparing the C hydrogenation to CH from the Literature with the data from own calculations. It can be noted that the forward and backward reaction energy for the hydrogenation of CH, the forward reaction energy in the data from Zhu et. al. [29] is much higher than the rest of the data. This means that their CH₂ species has a less stable configuration on the surface than the other datasets. Compared to the data from own calculations, Chen and coworkers find a lower forward activation energy. This can be due to their more stable CH₂ species. Furthermore, it can be seen that for the hydrogenation of CH₂ to CH₃, the reaction barriers vary between the Literature studies, as well as with the values from own calculations. Zhu and coworkers find a higher reaction barrier, while Chen and coworkers find a lower forward activation energy. Overall, the forward reaction energies calculated by Zhu et. al. lie higher than the rest of the data, while the backward reaction energies are in the same range, resulting in a higher overall reaction barrier. On the contrary, the forward reaction energies in general are lower, while the backward reaction energies are higher. Therefore, it can be concluded that Chen et. al. find more stable conformations for their species. The differences between the data from Chen et. al. can also be due to their use of SIESTA. SIESTA calculations, which use a LCAO (Linear Combination of Atomic Orbitals) basis set instead of a plane-wave basis set, are in general less accurate.

4.1.4 The production of C₁-oxygenates

Apart from methane, the reactions to C₁-oxygenates were investigated as well. There are several possible pathways leading to the production of these species. One of the possibilities is the hydrogenation of the CO, without breaking the CO bond. CO can then be hydrogenated on the carbon or on the oxygen. These pathways are further denoted as the methoxy and the hydroxyl pathways. Other possibilities are presented when CO dissociation takes place first. The possible reactions to C₁-oxygenates that were investigated concerns the production of formaldehyde and methanol. Corresponding reaction energy diagrams are shown in figure 14 and 15, respectively.

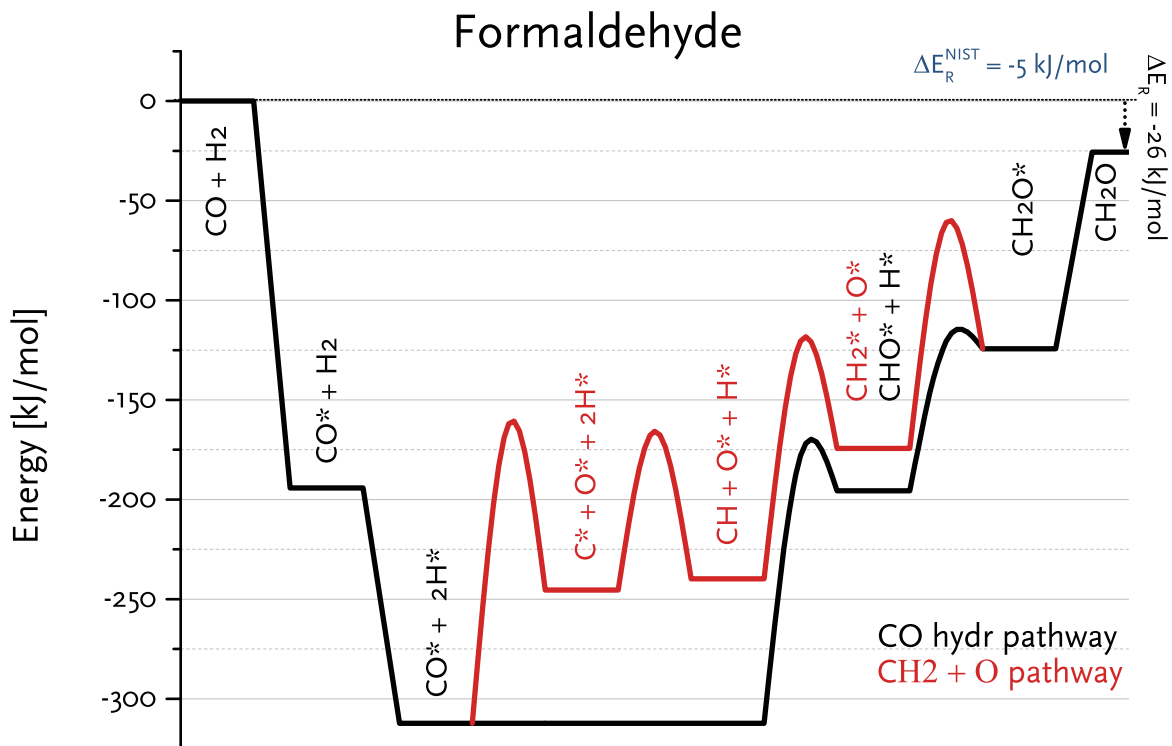


Figure 14: Reaction energy diagram for different pathways for the formation of formaldehyde on stepped rhodium.

There are only two possible pathways for the production of formaldehyde, starting from either CO hydrogenation to CHO or from CO dissociation to C and O. The latter possibility needs an additional coupling with an oxygen or hydroxy species. The simulated reaction enthalpy nicely matches the reaction enthalpy calculated from the formation enthalpies [40].

The reaction energy diagram shows two different pathways for the formation of formaldehyde that were investigated. It shows that not only the CO dissociation is less favorable than the methoxy pathway, it also shows that the overall energy barrier is higher. It can be concluded that the methoxy pathway is more favorable for the production of formaldehyde, and is therefore more likely to occur than the hydroxyl pathway. The total forward reaction energy was found to be 350 kJ/mol.

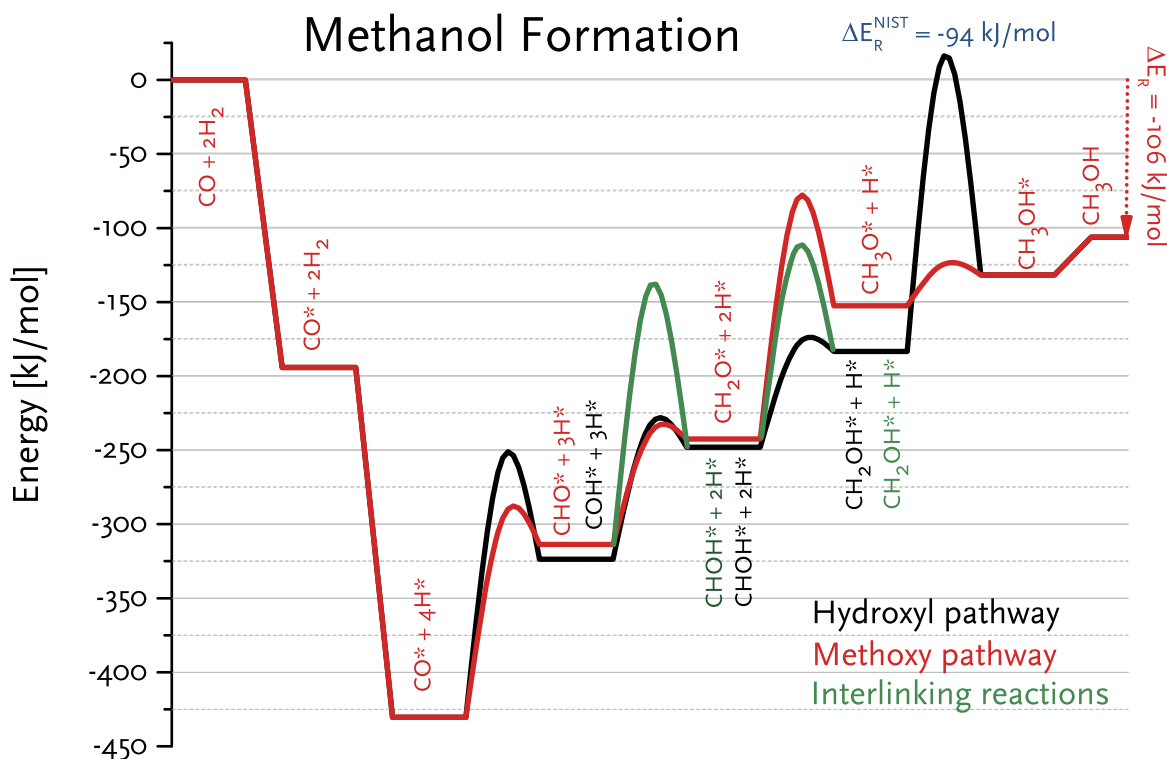


Figure 15: Reaction energy diagram for different pathways for the formation of methanol on stepped rhodium.

For the production of methanol, three possible pathways arise. Next to the CO dissociation pathway and the methoxy pathway, the hydroxyl pathway is now a possibility as well. With the hydroxyl pathway, the CO is hydrogenated on the oxygen, and a COH species is formed. This COH species propagates to CH₂OH, followed by the termination to CH₃OH. A comparison has been made between the hydroxyl pathway and the methoxy pathway.

The methoxy pathway starts by hydrogenating a CO species to a CHO species. This CHO species propagates to CH₃O and terminates to CH₃OH. Also, the interlinking reactions were investigated. These interlinking reactions contain CHO hydrogenation to CHOH and CH₂O to CH₂OH. The other possibility is breaking the CO bond before hydrogenation. This route then needs to couple again with an oxygen or and hydroxy species to obtain a C₁-oxygenate. This possibility is not further investigated, since the CO dissociative pathway turned out to be the least favorable the formation of formaldehyde.

Figure 15 shows that the energy barriers up until the CH₂O species are the lowest for the methoxy pathway. From the CH₂O species, the interlinking reaction to CH₂OH

is more favorable than the methoxy pathway reaction to CH_3O . However, the termination reaction of the hydroxyl pathway is significantly less favorable than the termination of the methoxy reaction, making the overall reaction more favorable for the methoxy reaction. It can be concluded that the methoxy pathway will be the most dominant pathway in the production of methanol. The simulated reaction enthalpy nicely matches the reaction enthalpy calculated from the formation enthalpies [40].

Figure 40 shows the transition state for key reactions in both the hydroxyl (figure 16a to 16c) and the methoxy (figure 16d to 16f) pathways. In this manner, a graphical comparison is made. It can be seen that the transition state for the formation of CHOH from CHO is less favorable than from COH to CHOH . This is because the oxygen is far away from the surface and in order to hydrogenate the oxygen from CHO , a hydrogen atom has to move far from the surface as well, resulting in the desorbing of the hydrogen atom before hydrogenating of the oxygen takes place. In the case of COH , the carbon, which must be hydrogenated in order to form CHOH , is close to the surface. The transition state is therefore more favorable, meaning that reaction through this pathway to form CHOH is lower in energy. The same holds true for the formation of CH_2OH . With CHOH , the carbon is closer to the surface and is therefore more easily hydrogenated. The oxygen in CH_2O is, like CHO , too far from the surface to hydrogenate easily. So, for this reaction, the transition state lies high in energy as well. The formation of methanol proceeds easier via the hydrogenation on the oxygen. This can be explained when looking at figures 16c and 16f. Both the CH_2OH as well as the CH_3O species are bound to the surface via the oxygen. This suggests that, in the case of CH_2OH , it may not be the most favorable configuration, since the transition state for reaction 18 is high in energy. However, CH_3O is easily hydrogenated to methanol, which leads to the conclusion that the transition state for reaction 15 is more favorable.

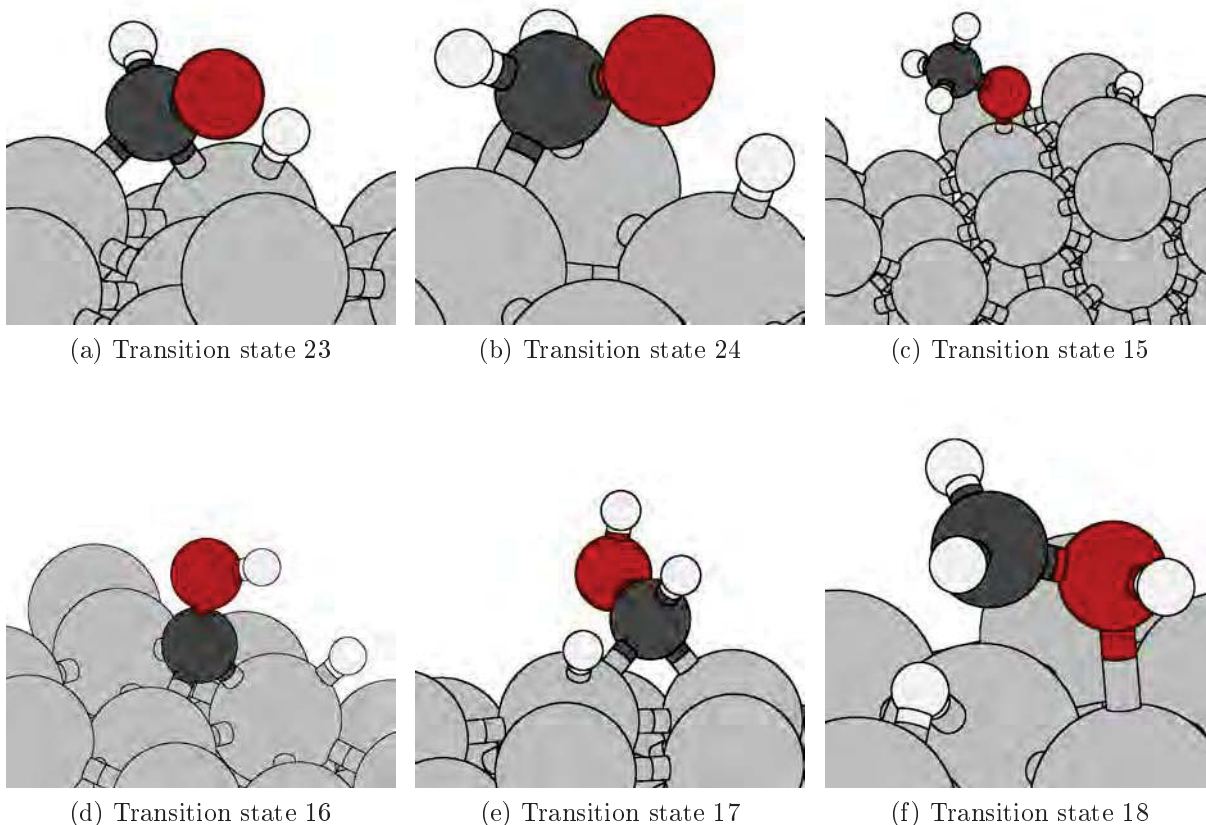


Figure 16: Graphical representation of transition states of formation of CHOH , CH_2OH , and CH_3OH .

Table 4 shows the comparison between activation energies from own calculations, compared to calculation on a stepped surface [34] and a Rh(111) surface [43] from Literature. From table 4 we see that the reaction of CO proceeds to a different species, comparing the stepped surface and the planer surface from the Literature. Hence, the path towards COH is preferred on the stepped surface, while the path to CHO is preferred on the planer surface. Own calculations show a preferred pathway for the CHO species, while, when comparing with the Literature, the stepped surface shows a preferableness for the COH species. The most probable explanation for this is the high activation energy for the formation of COH species. When looking at the most probable path from the CHO species, it can be seen that on both stepped and planer surface, the reaction to CH_2O requires less energy. This compares with the results from own calculations. Starting at CH_2O , hydrogenation can then proceed according to two possible reaction pathways. The reaction that requires the least energy on the stepped surface, as well as the planer surface, is the formation of CH_3O . This does not compare with our own calculations. However, the termination step was found to be much lower than the Literature. When comparing the reaction energies from the CH_3O added to reaction energy of the termination step to CH_3OH , the difference in total energy between own calculations and

the Literature is only 1 kJ/mol. This means that there are several ways to produce methanol.

Table 4: Elementary reaction steps as calculated for the methanol synthesis.

| # | Elementary Reaction Steps | E_f^a [kJ/mol] | E_b^a [kJ/mol] | E_f^b [kJ/mol] | E_b^b [kJ/mol] | E_f^c [kJ/mol] | E_b^c [kJ/mol] |
|----|---|---------------------|---------------------|---------------------|---------------------|---------------------|---------------------|
| 3 | $\text{CO}^* + \text{H}^*$ | 134 | 18 | 180 | 96 | 150 | 51 |
| 13 | $\text{C}\text{H}\text{O}^* + \text{H}^*$ | 75 | 4 | 37 | 16 | 59 | 0 |
| 14 | $\text{C}\text{H}_2\text{O}^* + \text{H}^*$ | 162 | 72 | 52 | 45 | 63 | 39 |
| 15 | $\text{C}\text{H}_3\text{O}^* + \text{H}^*$ | 28 | 7 | 92 | 75 | 81 | 69 |
| 2 | $\text{CO}^* + \text{H}^*$ | 175 | 68 | 94 | 11 | 217 | 120 |
| 16 | $\text{COH}^* + \text{H}^*$ | 91 | 15 | 49 | 12 | 104 | 38 |
| 17 | $\text{C}\text{H}\text{O}\text{H}^* + \text{H}^*$ | 69 | 4 | 0 | 11 | 77 | 63 |
| 18 | $\text{C}\text{H}_2\text{OH}^* + \text{H}^*$ | 200 | 148 | 75 | 68 | 88 | 72 |
| 19 | $\text{C}^* + \text{OH}^*$ | 204 | 170 | 139 | 115 | * | * |
| 20 | $\text{C}\text{H}^* + \text{OH}^*$ | 207 | 103 | 161 | 80 | * | * |
| 21 | $\text{C}\text{H}_2^* + \text{OH}^*$ | 141 | 38 | * | * | * | * |
| 22 | $\text{C}\text{H}_3^* + \text{OH}^*$ | 209 | 95 | 203 | 127 | * | * |
| 23 | $\text{C}\text{H}\text{O}^* + \text{H}^*$ | 175 | 109 | 90 | 49 | 93 | 29 |
| 24 | $\text{C}\text{H}_2\text{O}^* + \text{H}^*$ | 129 | 69 | 100 | 83 | 107 | 87 |
| 25 | $\text{C}\text{H}^* + \text{O}^*$ | 185 | 140 | 192 | 184 | * | * |
| 26 | $\text{C}\text{H}_2^* + \text{O}^*$ | 113 | 63 | 141 | 136 | * | * |
| 27 | $\text{C}\text{H}_3^* + \text{O}^*$ | 211 | 112 | 145 | 112 | * | * |

It is easier to distinguish the different possibilities on these surfaces comparing the energetically lowest pathways by means of a reaction energy diagram. The data for the methoxy pathway from own calculations were compared to data from Kapur et. al. [34]. The reaction energy diagrams are shown in figure 17 and 18.

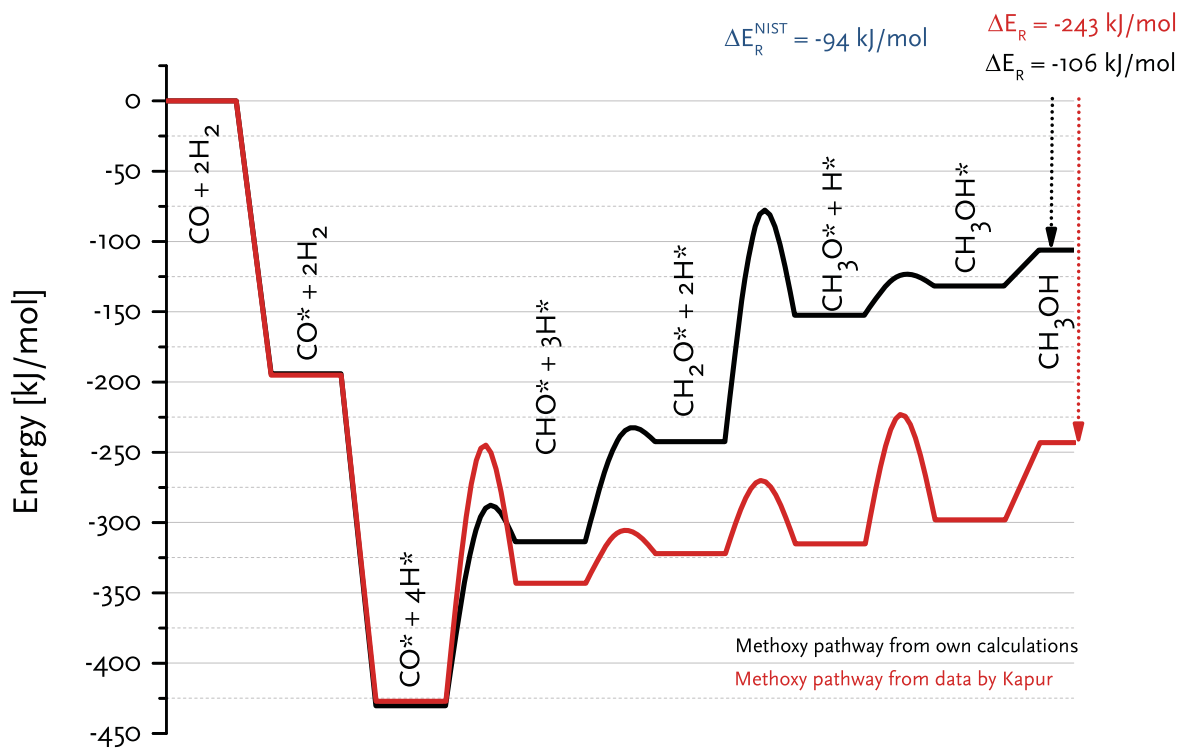


Figure 17: Reaction energy diagram for comparison of the methoxy pathways from the Literature [34] and from own calculations.

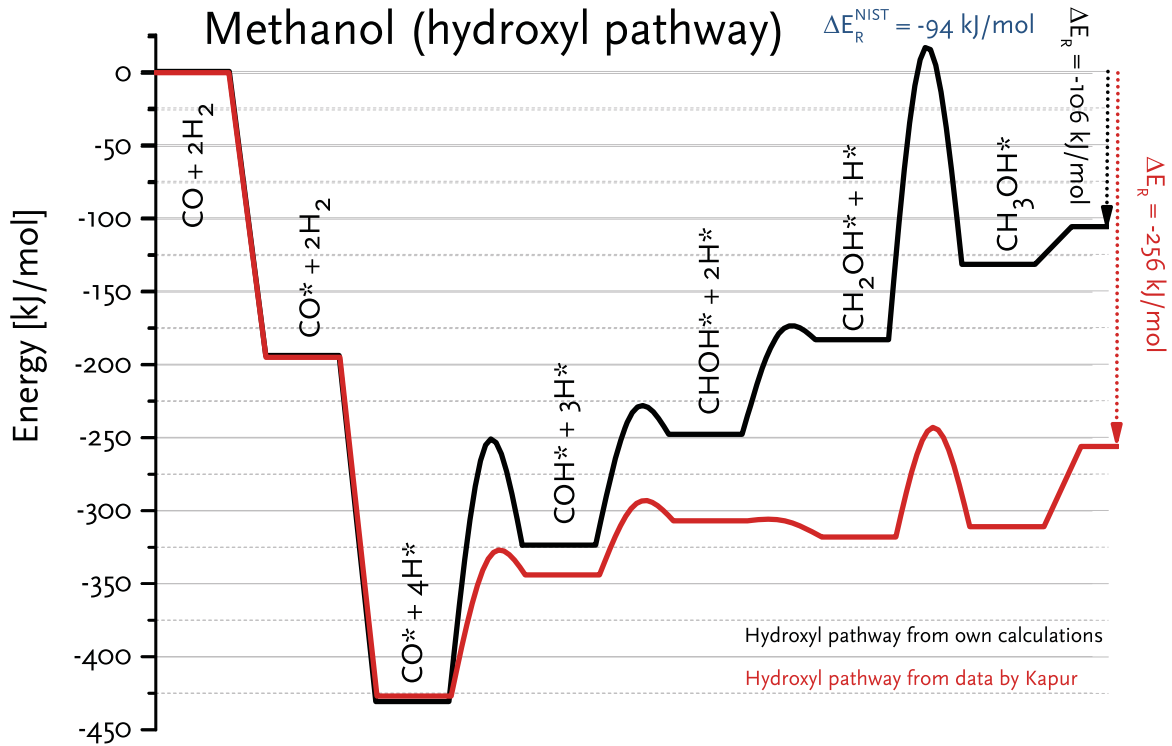


Figure 18: Reaction energy diagram for comparison of the hydroxyl pathways from the Literature [34] and from own calculations.

It can be seen in the reaction energy diagrams that the total energy of the reaction from syngas to methanol via methoxy pathway as well as the hydroxyl pathway are different from the reaction energy from our own calculations. The values from the Literature [34] do not match the experimental values [40]. It can also be noted that the data are not migration corrected, because the reaction energies for both hydroxyl and methoxy pathways do not coincide. From this we can conclude that there is probably something wrong with the migration correction on the data from the Literature.

More conclusions can be drawn from the key transition states, which were shown in figure 40. A difference in configuration can be found, when comparing the transition states with the transition states found by Kapur et. al. from reaction 23 and 24 with the corresponding transition states from Kapur and coworkers. The difference lies in the fact that the transition states, as shown by Kapur, are bound by the carbon as well as the oxygen. Therefore, the oxygen lies closer to the surface and is easier to hydrogenate. The rest of the transition states are much alike the ones from own work, with the exception of transition state 18. This transition state is bound by the carbon instead of the oxygen, making the transition state more stable and therefore lower in energy. This energy difference was already shown in table 4.

4.1.5 $\text{CH}_x\text{-CH}_y$ coupling reactions

In order to acquire longer chains, coupling reactions will need to take place. These couplings consist of $\text{CH}_x\text{-CH}_y$ coupling reactions, for the C_2 -hydrocarbons. These coupling reactions can take place between a CH_x and CH_y species. On the one hand, it is possible for these species to partially hydrogenate before coupling. On the other hand, they can also react without hydrogenation on forehand. which is the case for the coupling of two carbon species. These different possibilities have been investigated in a previous study, on the Quantummechanical analysis of the Carbide Fischer-Tropsch mechanism on Rh(211) [44]. This study showed that CH_2 species were not capable of coupling with other CH_x species. Therefore, only the plausible reactions from the previous study were taken into account in this study and recalculated in order to get the absolute energetic values from DFT. These energetic values are needed for a correct migration correction. These different reactions are shown in figure 19.

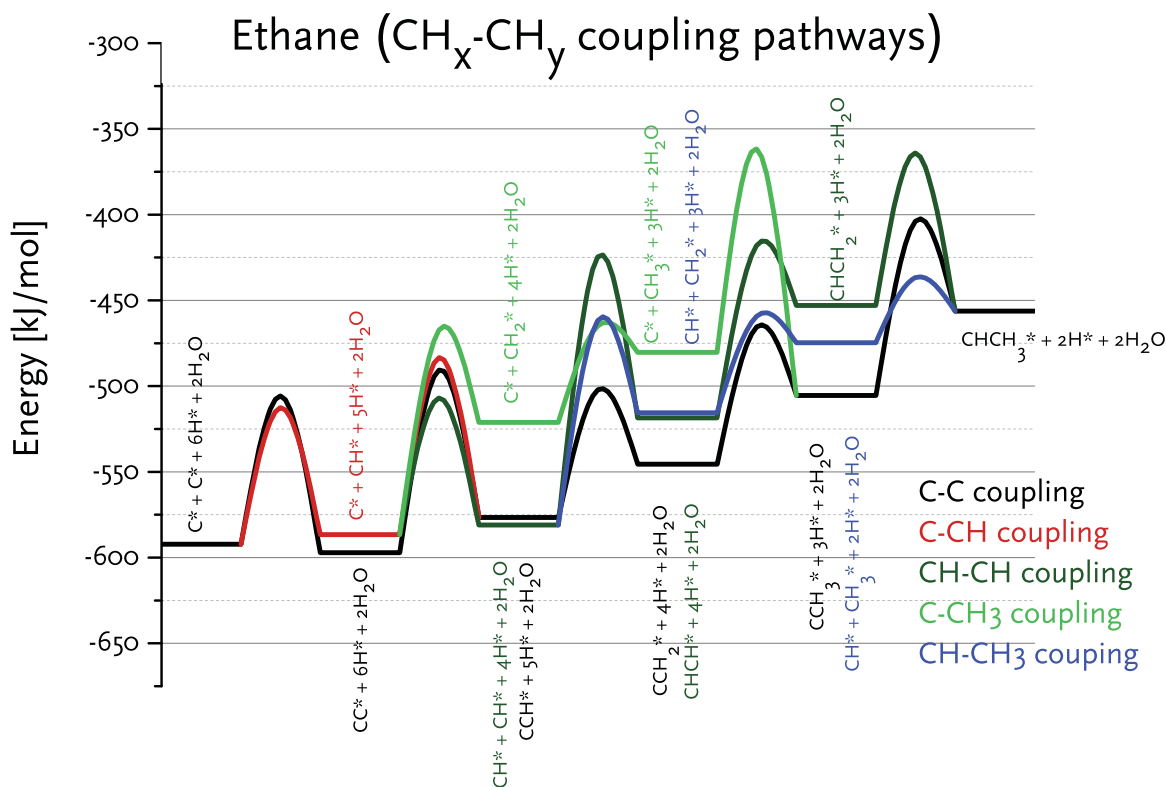


Figure 19: Reaction energy diagram for the studied C-C coupling reactions.

The above figure indicates that the coupling of two carbons is slightly more favorable than the coupling of a carbon and a CH species. This is a remarkable finding, since this is not true for these reactions on ruthenium. On ruthenium, the coupling of a carbon with a CH species is more favorable. It can also be noticed that the coupling of a carbon species to a CH_3 species is an endothermic process. The coupling of a carbon with a CH species and the coupling of two carbons is an almost thermo-neutral process. The

rest of the reactions are exothermic. The values of these elementary reaction steps, as well as a graphical representation of them, can be found in table 20 and 21 in section 8.5.

At first sight, the reaction energies seem to indicate that the C-C coupling pathway is the most dominant pathway. This pathway starts from a carbon on the surface and propagates to CHCH₃ where it has no energy barrier higher than 106 kJ/mol, while the other reactions have a reaction energy of at least 119 kJ/mol. However, from figure 19 we can conclude that the most probable manner to couple a CH_x species and a CH_y species is not via the C-C coupling reaction, but by means of the CH-CH₃ coupling reaction. This can not only be concluded because the coupling reaction itself is lowest in activation energy, but also because the overall energy barrier for the reaction is lowest in energy compared to the rest of the investigated coupling reactions. Nevertheless, the C-C coupling reaction remains a probability.

Comparisons between own calculations and calculations for activation energies on rhodium between own calculation and the Literature [42,45] can be found in table 5.

Table 5: Elementary reaction steps as calculated for the C-C coupling reactions from own calculations^a as well as from the Literature [45]^b [42]^c. Values of the backward reaction energies are not reported in the Literature. E_f stands for the forward reaction energy and E_b for the backward reaction energy. All energies are in kJ/mol.

| # | Elementary Reaction Steps | | | E_f [kJ/mol] ^a | E_b [kJ/mol] ^a | E_f [kJ/mol] ^b | E_f [kJ/mol] ^c |
|----|---------------------------------------|---|---------------------------------------|-----------------------------|-----------------------------|-----------------------------|-----------------------------|
| 28 | C* + C* | ↔ | CC* + * | 86 | 91 | 218 | 113 |
| 29 | C* + CH* | ↔ | CCH* + * | 103 | 93 | 160 | 90 |
| 30 | C* + CH ₃ * | ↔ | CCH ₃ * + * | 119 | 144 | 144 | 104 |
| 31 | CH* + CH* | ↔ | CHCH* + * | 156 | 94 | 139 | 117 |
| 32 | CH* + CH ₃ * | ↔ | CHCH ₃ * + * | 38 | 20 | 154 | 155 |
| 33 | CH ₂ * + CH ₂ * | ↔ | CH ₂ CH ₂ * + * | 75 | 136 | 83 | 91 |

Figure 44 shows the transition states of reaction 28, 29, and 32. These transition states can be compared to transition states reported in the Literature. These specific transition states were chosen for comparison because of the big energy difference in forward reaction energies.

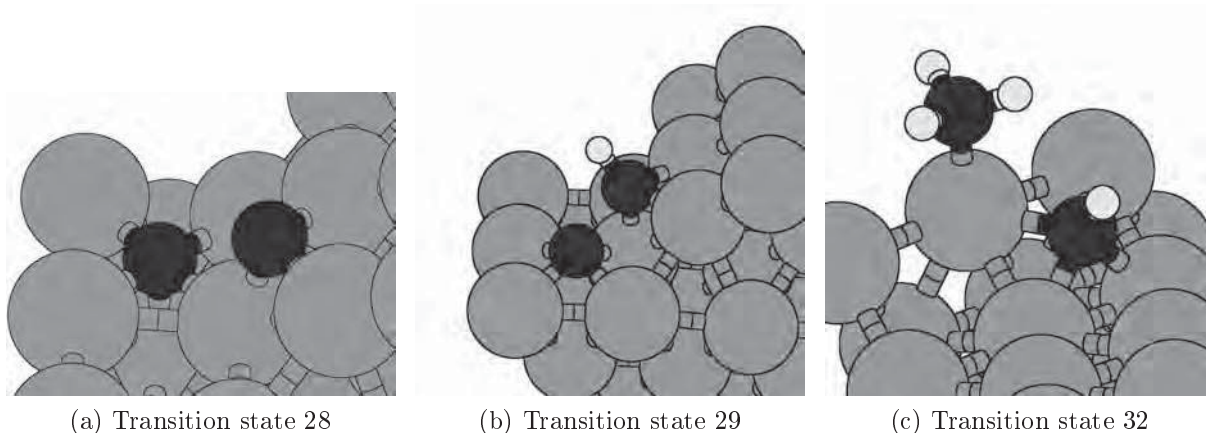


Figure 20: Graphical representation of transition states of $\text{CH}_x\text{-CH}_y$ coupling reactions.

When comparing the transition state from reaction 28 with the transition state as reported in the Literature, it can be seen that the C-C coupling takes place on the B5-site, where one of the carbon atoms starts bridged, while the other carbon starts in a three-fold position on the B5-site. In our own work, the first carbon starts in a 4-fold position in the B5-site, while the second carbon starts from the threefold position of the neighboring B5-site. In this manner, the C-C coupling proceeds via three rhodium atom, while the Literature states that the C-C coupling takes place over 2 rhodium atoms. It could be argued that, when the carbon is positioned on the neighboring B5-site, the carbon atoms are further apart, meaning that the repulsion between the two carbon species is lower. For the C-CH coupling, which proceeds in the same manner than the C-C coupling reaction, the reaction energies resemble the values as reported by Chen et. al. However, they do not match the values from Cheng et. al. This is due to the fact that the transition state from Chen and coworkers looks approximately the same, while the transition state from Cheng and coworkers do not match. Cheng and coworkers have a coupling over the same B5-site atoms, while Chen et. al. couple the C with CH in the same manner as in our own calculations. Apparently, it is more favorable to couple the C species with a CH species over three rhodium atoms, instead of two, as was the case with the C-C coupling reaction. The reaction energy for the CH- CH_3 coupling does not compare to the values from the Literature. The transition state proceeds over two rhodium atoms in the Literature, while it proceeds over 1 in our own calculations. The fact that CH_3 couples over 1 rhodium atom can be explained by the fact that CH_3 behaves as a hydrogen atom. Hence, a hydrogenation tends to proceed via a single rhodium atom.

4.1.6 Hydrogenations towards C_2 - Hydrocarbons

After $\text{CH}_x\text{-CH}_y$ coupling has taken place, the CH_xCH_y species can be further hydrogenated to stable C_2 - Hydrocarbons. In this study, the production of ethylene and ethane are investigated as products from the $\text{CH}_x\text{-CH}_y$ coupling reactions, as described in section 4.1.5. The two most probable ways to couple the two carbon species are shown in the reaction energy diagram in figure 21.

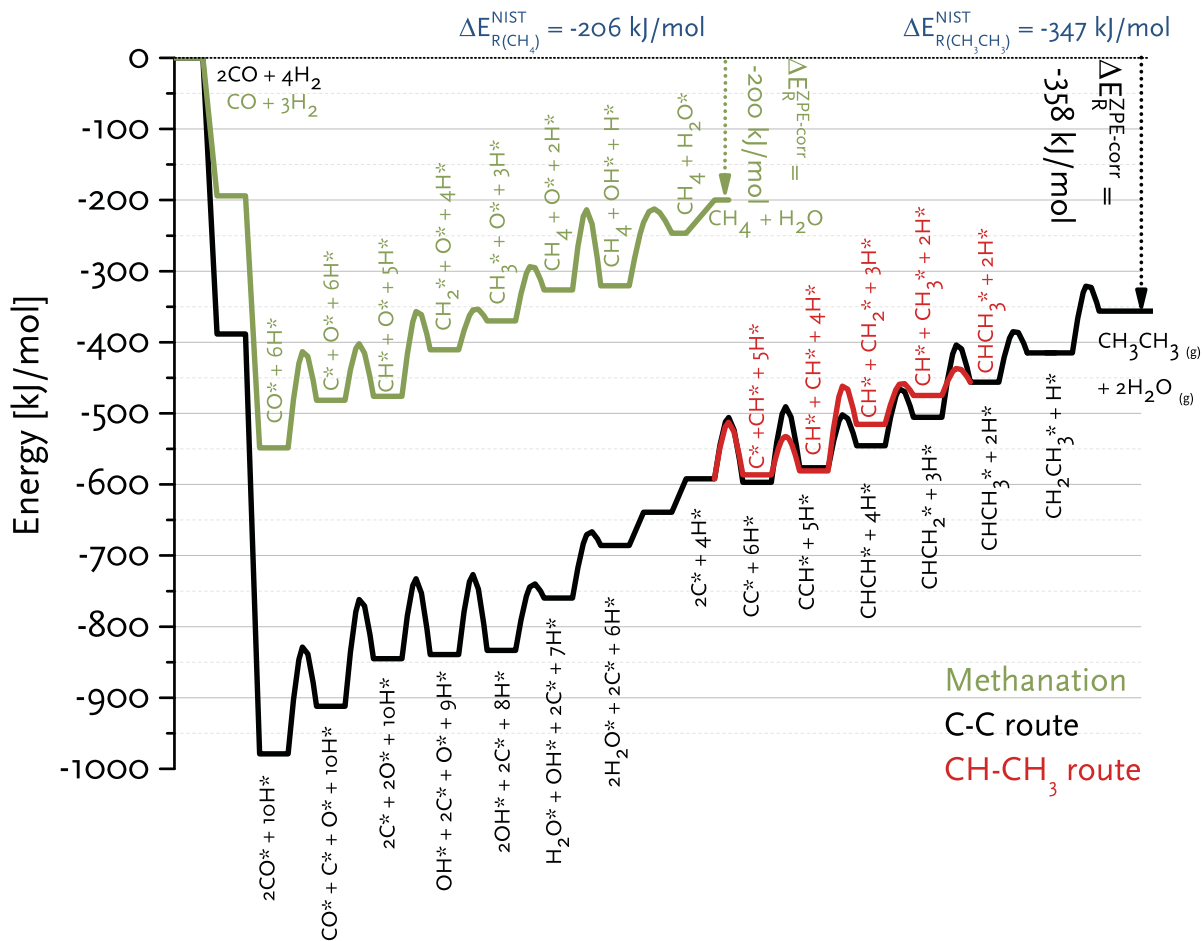


Figure 21: Reaction energy diagram for the production of ethane as compared to the production of ethane.

This figure shows the comparison between two routes for the formation of ethane as well as the formation of methane. It can be seen from the reaction that the production of ethane is far more endothermic than the reaction to methane. This is in good comparison with the values of experiments [40].

The same routes of the coupling reactions can be taken for the production of ethylene. Two different routes for the reactions that proceed via the C-C coupling are investigated. These routes are the direct and indirect pathway. Both pathways propagate to the CCH₂ species. The direct pathway then hydrogenates to a CHCH₂ species, while the indirect pathway hydrogenates to a CCH₃ species. The CHCH₂ species then terminates to ethylene, while the CCH₃ hydrogenates further to CH₂CH₃ before terminating to ethylene. These different pathways are shown in reaction energy diagram 22.

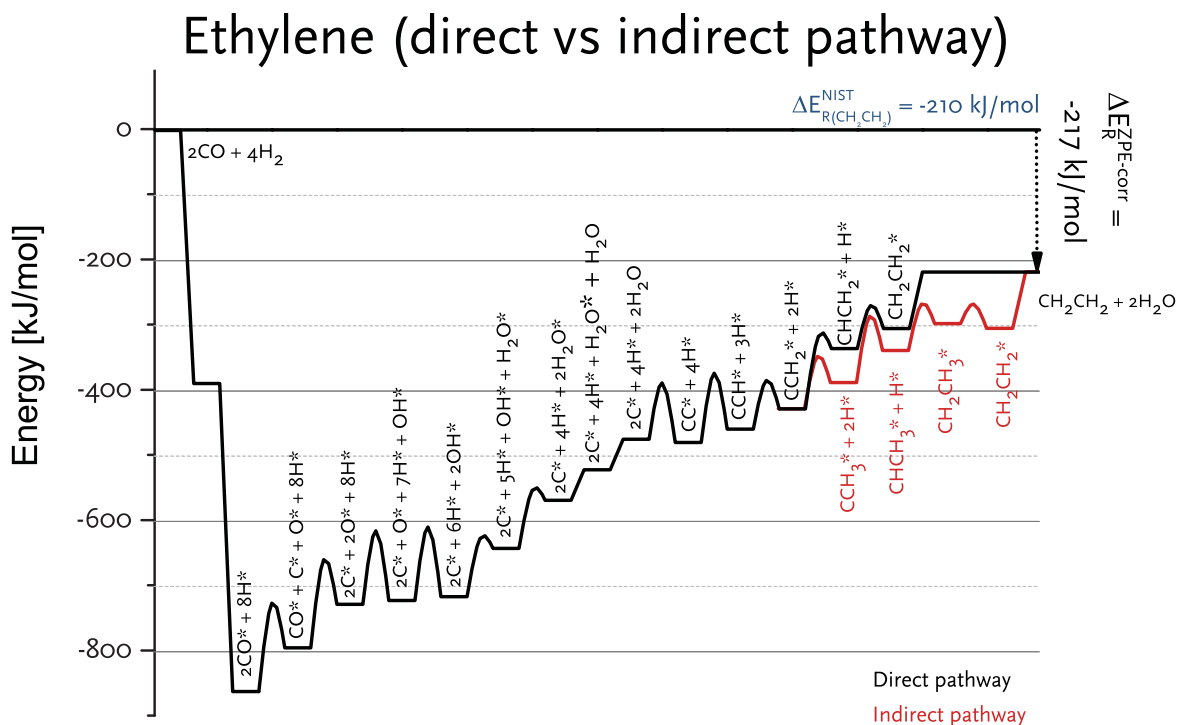


Figure 22: Reaction energy diagram for the indirect and the direct pathway for the production of ethylene.

Although the diagram shows that the indirect pathway proceeds to a more stable state, coming from CCH_2 , both pathways have approximately the same overall reaction energies, making them both likely to take place. It can also be seen that most reactions are exothermic, except for the termination step of the indirect pathway and the C-C coupling step, which are more or less thermo-neutral. The values of these elementary reaction steps towards ethane and ethylene, as well as a graphical representation of them, can be found in table 22 and 23 in section 8.6.

The comparison can be made for the ethylene reaction on rhodium and on ruthenium. This is shown in the reaction energy diagram in figure 23.

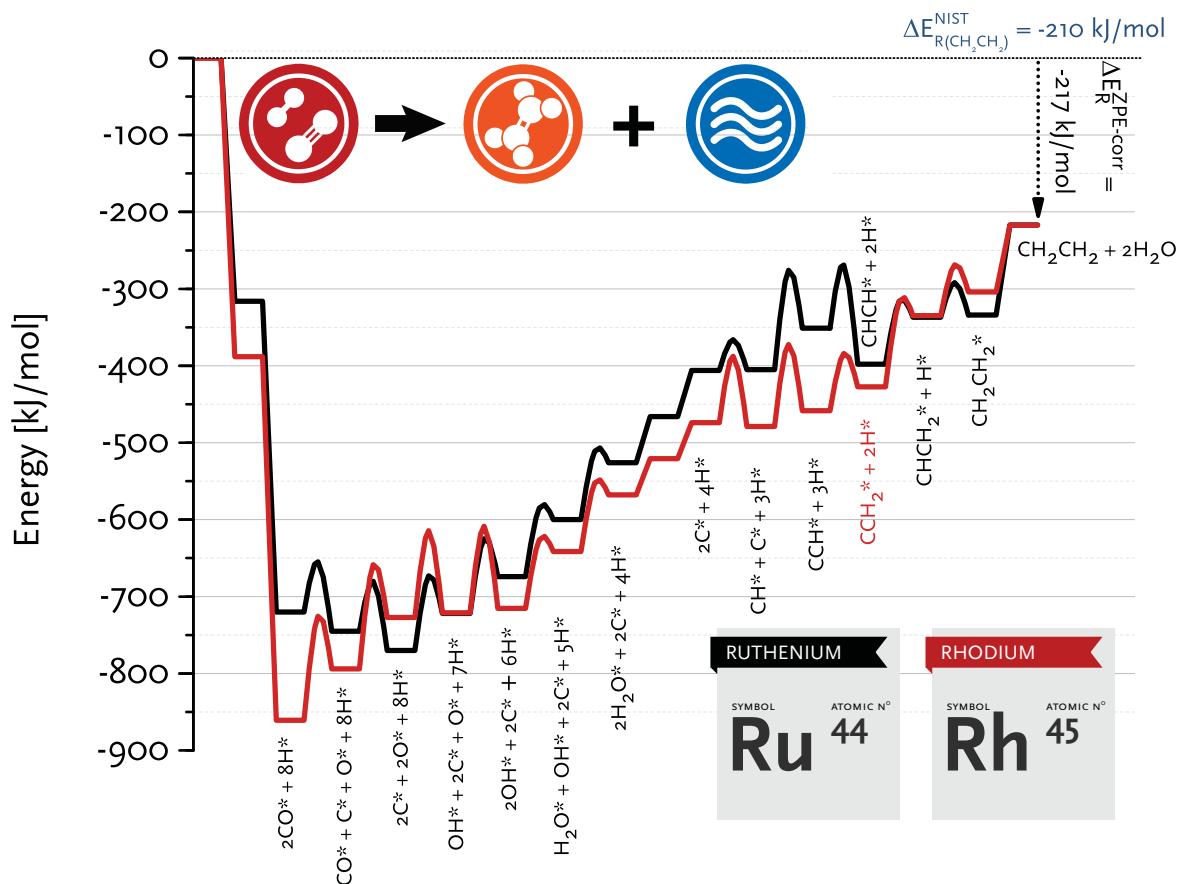


Figure 23: Reaction energy diagram for the comparison of the production of ethylene on rhodium and ruthenium.

It can be concluded from the reaction energy diagram, that adsorption reactions on ruthenium are less endothermic than on rhodium. In contrast, water formation, when ignoring the difference in adsorption energies, is energetically more favorable on ruthenium than on rhodium. It can also be seen that the desorption energy on ruthenium is higher than on rhodium, meaning that the desorption is more exothermic on ruthenium when compared to rhodium. It can also be seen that the reaction on rhodium proceeds via a different propagation step from the CCH species. On rhodium, CCH is propagated to CCH₂, while it is more favorable to propagate CCH to a CHCH species on ruthenium. Although the reactions differ quite a lot regarding their activation barriers, their overall energy barriers are about the same. No comparable calculations were found in the Literature for the hydrogenation reactions on a stepped rhodium surface.

4.1.7 CO insertion

In order to produce C₂-Oxygenates coupling has to take place between a CH_x species and a CO species. The hypothesis states that the formation of rhodium proceeds via a CO insertion mechanism. Since CO dissociation is not relatively easy or relatively difficult, the amount of CO species and the amount of carbon on the surface will probably

be in the same order of magnitude. Therefore, it makes sense that CO species couples with a CH_x species on the surface for the production of ethanol.

When looking at CO insertion, there are a few possibilities that could occur as a coupling reaction. The CO could couple with a C, CH, CH_2 or CH_3 species. All these possibilities were investigated. CH_3CO seemed to be unstable and was found to dissociate before the end of the run. The remaining possibilities are shown in the reaction energy diagram in figure 24

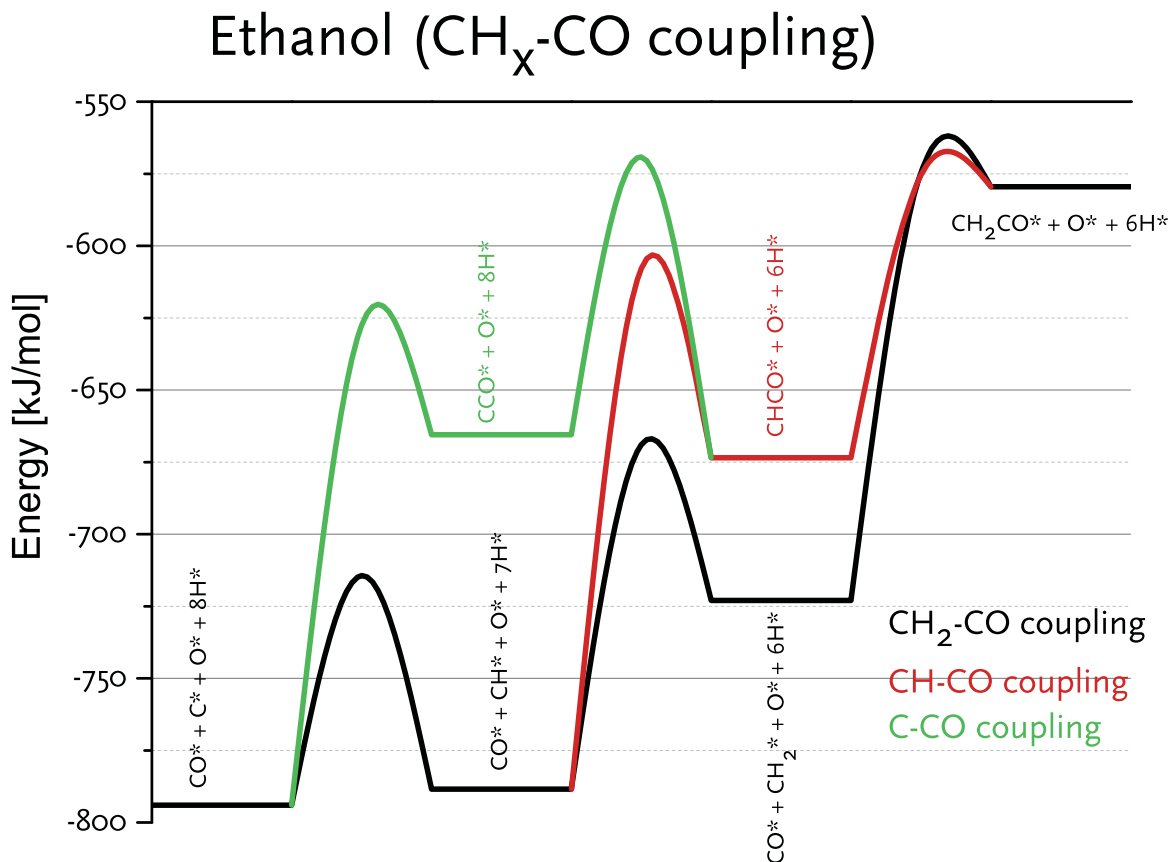


Figure 24: Reaction energy diagram for the different CO insertion reactions.

It can be seen from the reaction energy diagram that the CH_2 -CO coupling pathway has the lowest activation barrier for the elementary reaction step of the coupling reaction itself. However, this will probably not be the most dominant pathway, because its overall reaction energy is higher in energy than the CH-CO coupling pathway. Therefore, the CH-CO coupling pathway will probably be the most dominant CO insertion reaction on rhodium. It must be noted that the overall energy barriers for all coupling reactions to CH_2CO are close together. It can be conclude from this, that the coupling of a CO with a CH_x species does not depend the amount of hydrogen atoms bound to the CH_x species. The values of these elementary reaction steps for the CO insertion reactions, as well as a graphical representation of them, can be found in table 24 and 25 in section 8.7.

Comparisons between own calculations and calculations for activation energies on rhodium between own calculation and the Literature [12,34] can be found in table 6.

Table 6: Elementary reaction steps as calculated for the CO-insertion reactions from own calculations^a as well as from the Literature [12]^b [34]^c. Values of the backward reaction energies are not reported in the Literature. E_f stands for the forward reaction energy and E_b for the backward reaction energy. All energies are in kJ/mol. Data that was not calculated in the Literature is marked by a *.

| # | Elementary Reaction Steps | E_f^a [kJ/mol] | E_b^a [kJ/mol] | E_f^b [kJ/mol] | E_b^b [kJ/mol] | E_f^c [kJ/mol] | E_b^c [kJ/mol] |
|----|---|---------------------|---------------------|---------------------|---------------------|---------------------|---------------------|
| 45 | $C^* + CO^* \rightleftharpoons CCO^* + *$ | 166 | 38 | 134 | 91 | * | * |
| 46 | $CH^* + CO^* \rightleftharpoons CHCO^* + *$ | 181 | 66 | 138 | 42 | 160 | 64 |
| 47 | $CH_2^* + CO^* \rightleftharpoons CH_2CO^* + *$ | 148 | 5 | * | * | 70 | 16 |

From tabel 6 we can conclude that the CO insertion reaction is energetically the most favorable with CH_2 -CO coupling. This is shown from the Literature, as well as from our own calculations. It can also be concluded that the CH-CO coupling is the least favorable coupling pathway. Apart from the difference in energies, the general trends are the same for the different datasets.

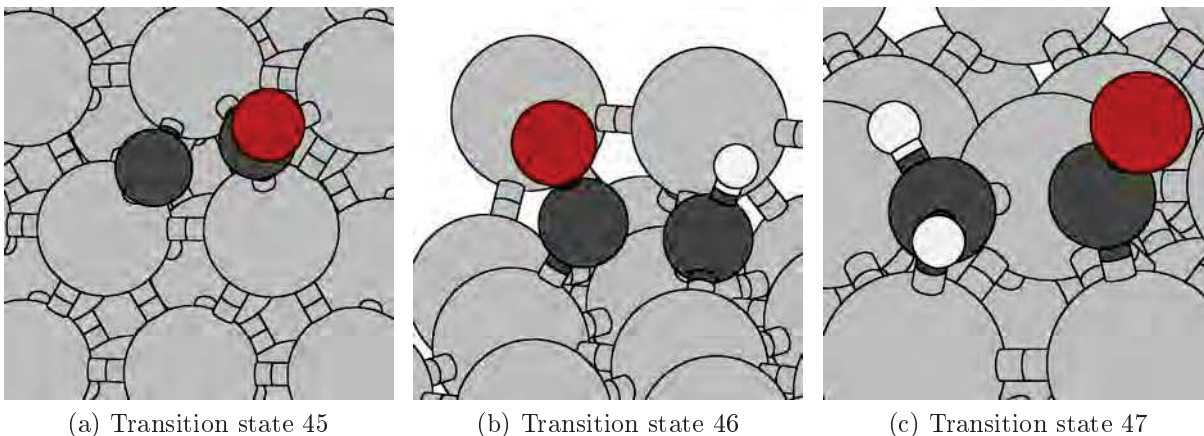


Figure 25: Graphical representation of transition states of the CH_k -CO coupling reactions.

When CO insertion proceeds via the C-CO coupling, C couples to a CO. The consequence of this is that the CO stays in a threefold configuration, while the carbon couples to the CO. When CO inserts into a C which is already partially hydrogenated, the CO moves, via a single rhodium atom, to the hydrogenated species. In the Literature, the CO is also coupled via a single rhodium atom, when CH-CO coupling takes place. For CH_2 -CO coupling, the CO moves via a bridged transition state. The C-CO coupling proceeds differently, according to the calculation from van Rijn et. al. [12], because

here, the CO stays in a fourfold position, while the CO reacts over one rhodium atom in order to couple to CCO. This is the origin of the difference in energies.

4.1.8 Hydrogenations towards C₂–Oxygenates

After CH-CO coupling has taken place, stable C₂–Oxygenates can be formed by means of hydrogenation reactions. The stable products, that were investigated in this study, are ethanol and acetaldehyde. Firstly, the production of ethanol via various pathways, namely the hydroxyl and ethoxy pathway, with each their own subset of pathways is described. Secondly, the reaction to acetaldehyde is discussed. The reactions to CH₃CO and hydrogenations of CH₃CO are not discussed, because the CH₃CO turned out to be unstable on the surface, splitting directly into a CH₃ species and a CO species. The values of the elementary reaction steps for the hydrogenation reactions of C₂–Oxygenates, as well accompanying graphical representations of these steps, are shown in table 26 and 27 in section 8.8.

The reaction towards ethanol can proceed via multifarious pathways. The pathways investigated are the ethoxy pathways and the hydroxyl pathways. In the ethoxy pathways, the carbon atoms of the CH_xCO propagate to CH₃CH₂OH, before termination to ethanol takes place. The hydroxyl pathway consists of reaction pathways at which the CH_xCO species hydrogenates to CH_xCOH before it proceeds with the propagation, resulting in two different termination pathways. In figure 26, the different possibilities for the production of ethanol via the hydroxyl pathways are shown.

All pathways start, as described in section 8.1, with a CH-CO coupling reaction. This is followed by the reaction towards CHCOH. From this point, the primary carbon can be hydrogenated to CH₂COH, as is shown in pathways 1 and 2. When CH₂COH is formed, the species can be hydrogenated again on the primary and on the secondary carbon, resulting in the production of CH₃COH and CH₂CHOH, respectively. The formation of CH₂CHOH is represented by pathway 1, while formation of CH₃COH is produced following pathway 2. These two pathways come together again with the formation of the CH₃CHOH species. Only termination to ethanol rests from this point on.

The other possibility is the hydrogenation of the secondary carbon, which proceeds in the formation of CHCHOH, as is shown in pathways 3 and 4. From this CHCHOH species, it is possible to hydrogenate the primary carbon, producing CH₂CHOH, or the secondary carbon, producing CHCH₂OH. Pathway 3 can cross at this point when hydrogenation on the primary carbon occurs. When hydrogenation of the secondary carbon occurs, pathway 3 results in CH₂CH₂OH. Pathway 4 can only be hydrogenated on the primary carbon, so evidently the CH₂CH₂OH is formed. From here, both pathway 3 and 4 terminate by hydrogenation of the primary carbon to ethanol.

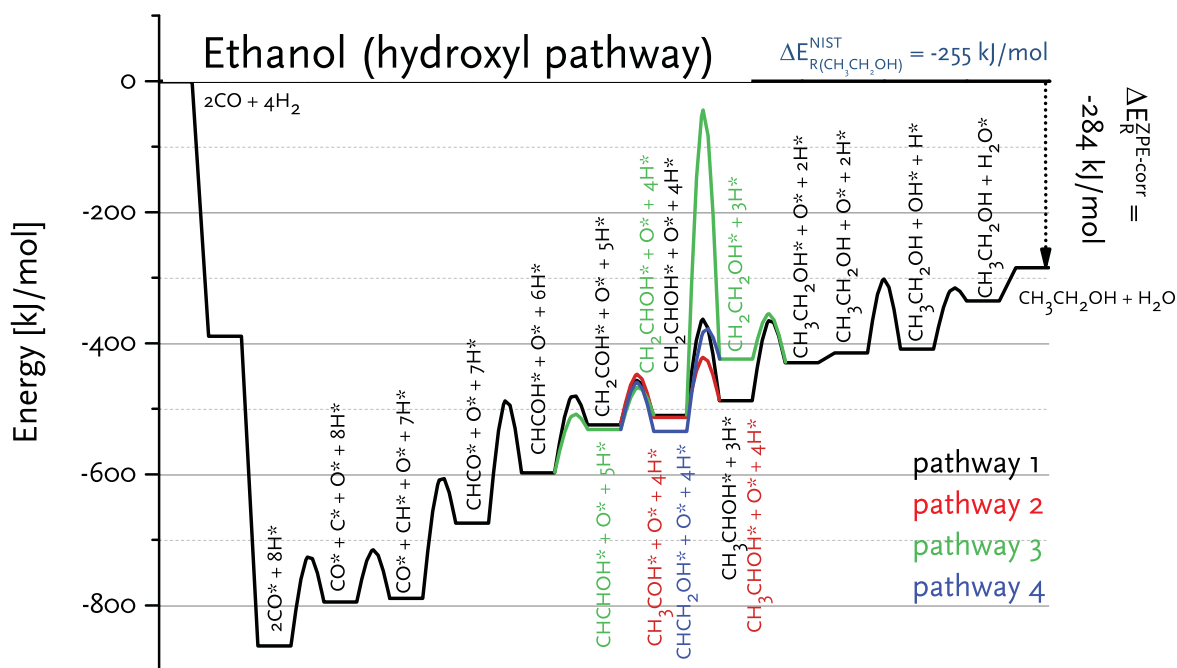


Figure 26: Reaction energy diagram for the different hydroxyl pathways for the production of ethanol.

The ethoxy pathway can proceed via three different routes. All three possibilities are shown in the reaction energy diagram in figure 27. The possible pathways start with the CH-CO coupling, as it does with the hydroxyl pathways. The ethoxy pathways are represented by the termination step, which is the same for all possible ethoxy pathways, namely the termination from $\text{CH}_3\text{CH}_2\text{O}$ to ethanol.

When coupling has taken place, the CHCO species can be hydrogenated on the primary carbon and on the secondary carbon. When hydrogenated on the primary carbon, CH_2CO is formed, as shown in pathway 1 and 2. When CH_2CO is hydrogenated on the primary carbon to CH_3CO , it follows pathway 1. This species can then only be hydrogenated to $\text{CH}_3\text{CH}_2\text{O}$, before terminating to ethanol. Hydrogenation of CH_2CO on the secondary carbon species leads to a CH_2CHO species. From here, hydrogenation can follow pathway 1, when hydrogenated on the primary carbon. When the CH_2CHO species is hydrogenated on the secondary carbon, $\text{CH}_2\text{CH}_2\text{O}$ is formed, as described by pathway 2. This species propagates to $\text{CH}_3\text{CH}_2\text{O}$, before terminating to ethanol.

On the other hand, when CHCO is hydrogenated on the secondary carbon, CHCHO is formed. This CHCHO is then either hydrogenated on the primary carbon to CH_2CHO , or hydrogenated on the secondary carbon to CHCH_2O . CH_2CHO can react further via pathway 1, or pathway 2, as discussed before. On the other hand, CHCH_2O can only react to $\text{CH}_2\text{CH}_2\text{O}$, proceeding via pathway 2 from this point on.

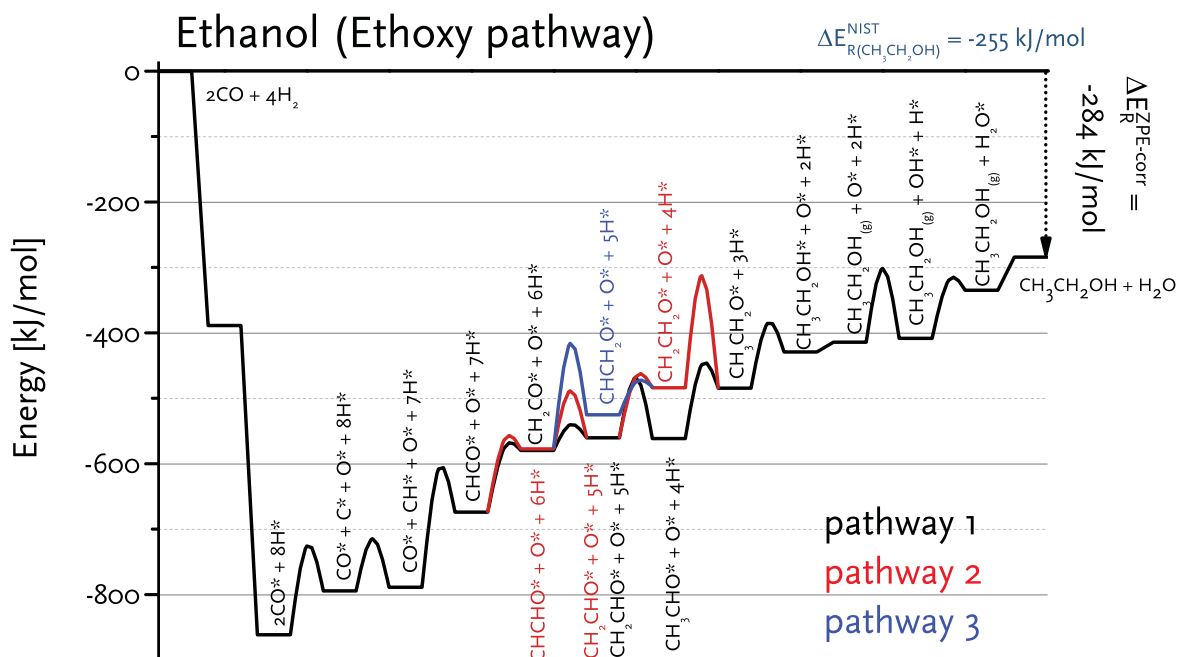


Figure 27: Reaction energy diagram for the different ethoxy pathways for the production of ethanol.

Formation of acetaldehyde proceeds via the previously discussed ethoxy pathway. Also within the formation of acetaldehyde, there are two possible pathways. The first pathway (CH₂CO route) hydrogenates the primary carbon of CHCO to CH₂CO. From here, it propagates further to CH₃CHO before desorbing. The second pathway (CHCHO route), hydrogenates the secondary carbon of CHCO to CHCHO. From here, it propagates further to CH₂CHO and proceeds via the first pathway from this point. The different pathways are shown in the reaction energy diagram in figure 28. The simulated reaction enthalpies for both hydroxyl and ethoxy mechanisms match the reaction enthalpy calculated from the formation enthalpies [40] reasonably.

Table 7: Elementary reaction steps as calculated for the CO-insertion reactions from own calculations^a as well as from the Literature [34]^b [46]^c. Values of the backward reaction energies are not reported in the Literature. E_f stands for the forward reaction energy and E_b for the backward reaction energy. All energies are in kJ/mol. Data that was not calculated in the Literature is marked by a *.

| # | Elementary Reaction Steps | E_f^a [kJ/mol] | E_b^a [kJ/mol] | E_f^b [kJ/mol] | E_b^b [kJ/mol] | E_f^c [kJ/mol] | E_b^c [kJ/mol] |
|----|--|---------------------|---------------------|---------------------|---------------------|---------------------|---------------------|
| 54 | $\text{CH}_2\text{CO}^* + \text{H}^*$ | 187 | 110 | * | * | 130 | 85 |
| 60 | $\text{CH}_2\text{CO}^* + \text{H}^*$ | 40 | 20 | 38 | 32 | * | * |
| 65 | $\text{CH}_2\text{COH}^* + \text{H}^*$ | 116 | 43 | * | * | 14 | 49 |
| 70 | $\text{CH}_2\text{CHO} + \text{H}^*$ | 92 | 94 | 59 | 63 | * | * |
| 71 | $\text{CH}_2\text{CHO}^* + \text{H}^*$ | 93 | 17 | 70 | 27 | * | * |
| 72 | $\text{CH}_2\text{CHO}^* + \text{H}^*$ | 93 | 42 | 99 | 87 | * | * |
| 73 | $\text{CH}_2\text{COH}^* + \text{H}^*$ | 76 | 66 | * | * | 68 | 46 |
| 80 | $\text{CH}_3\text{CHO}^* + \text{H}^*$ | 113 | 36 | 58 | 39 | * | * |
| 81 | $\text{CH}_3\text{CHO}^* + \text{H}^*$ | 90 | 15 | 105 | 81 | * | * |
| 82 | $\text{CH}_3\text{COH}^* + \text{H}^*$ | 92 | 65 | 53 | 52 | 158 | 44 |
| 83 | $\text{CH}_2\text{CH}_2\text{O}^* + \text{H}^*$ | 171 | 171 | 28 | 55 | * | * |
| 84 | $\text{CH}_2\text{CH}_2\text{O}^* + \text{H}^*$ | 147 | 93 | 91 | 67 | * | * |
| 88 | $\text{CH}_3\text{CH}_2\text{O}^* + \text{H}^*$ | 99 | 44 | 76 | 73 | * | * |
| 89 | $\text{CH}_3\text{CHOH}^* + \text{H}^*$ | 122 | 64 | 65 | 61 | 218 | 64 |
| 90 | $\text{CH}_2\text{CH}_2\text{OH}^* + \text{H}^*$ | 75 | 74 | 42 | 84 | * | * |

From table 7 we can conclude that the reaction to CHCOH differs from the value reported in the Literature. It may be the case that there is a more favorable pathway for the production of this species. Another possibility is that the difference in energy is compensated further on in the pathway. This could be the case here, since the reaction barrier from the termination reaction by Zhang et. al. is significantly higher compared to our own calculation. This is probably due to the fact that Reactions 60, and 71 are more in line with the values presented by Kapur et. al. Reactions 70, 72, 80, 81, and 84 show the same trends with respect to the thermicity of the reactions. However, this is not true for reaction 82, 83, and the termination reactions 88 and 90.

Some key transition states are shown in figure 29. All transition states can be compared with the transition states as reported by Kapur et. al. In transition state 80 it is seen that the oxygen is the only atom bound to the surface. When looking at the results of the intermediate from Kapur and coworkers, it can be seen that their transition state is bound by the oxygen as well as the adjacent carbon atom. This lowers the energy of the transition state, lowering the activation energies for the reaction. Comparing the transition state from reaction 83 with the transition state from the Literature, it is shown that the reaction energy decreases enormously, when the α -C is bound to the surface as well. The same holds for the transition state from reaction 84, where the oxygen could also be bound to the surface, making the transition state lower in energy.

For the termination reactions the transition states are shown in figure 29d to 29f

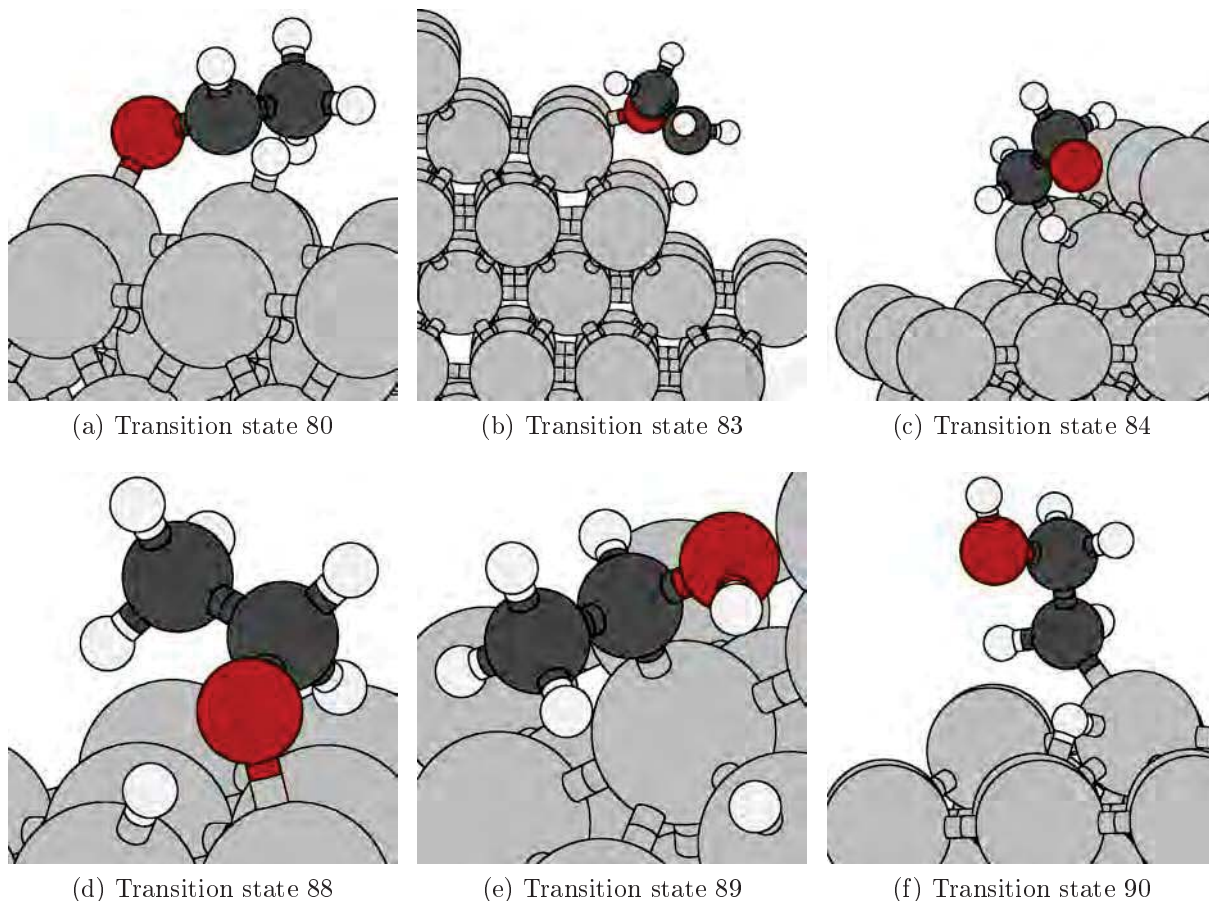


Figure 29: Graphical representation of transition states for the formation of key intermediates, as well as all termination reactions.

4.1.9 Towards the formation of C₃-Oxygenates

Not only the possibility for the formation of C₂-Oxygenates was investigated, but also the possibility for the formation of C₃-Oxygenates was looked at. For C₃-Oxygenates to take place, the CH_xCH_yO species must first undergo a CO dissociation to CH_xCH_y and O, before another CO insertion can take place. Therefore, several CH_xCH_yO dissociations have been investigated. CO insertion on a CHCH₃ has been investigated, because this is comparable with the CO insertion on a CH₂ species, because a methyl group behaves itself as a hydrogen group when looking at CO insertion. Since the CH₂-CO coupling is the most favorable coupling reaction for C₂-Oxygenates, we can assume that for the production of C₃-Oxygenates, this will probably also hold true. Therefore, the CHCH₃-CO coupling reaction is calculated as well for the production of C₃-Oxygenates. The energies of the dissociation reactions as well as a CO insertion reaction to CHCH₃ can be found in table 28.

Table 8: Elementary reaction steps as calculated needed for formation of C₃-Oxygenates.

| # | Elementary Reaction Steps | E_f [kJ/mol] | E_b [kJ/mol] |
|----|---|----------------|----------------|
| 91 | $\text{CH}_2\text{CO}^* + * \longleftrightarrow \text{CH}_2\text{C}^* + \text{O}^*$ | 188 | 289 |
| 92 | $\text{CH}_2\text{CHO}^* + * \longleftrightarrow \text{CH}_2\text{CH}^* + \text{O}^*$ | 124 | 152 |
| 93 | $\text{CHCH}_3^* + \text{CO}^* \longleftrightarrow \text{CH}_3\text{CHCO}^* + *$ | 209 | 106 |

It is shown that dissociation of CO is possible from a CH₂CHO species. However, even if CO dissociation takes place, it is not feasible to insert a CO into the growing chain. This leads to the conclusion that C₃-Oxygenates will probably not be formed during the FT reaction on rhodium.

4.2 Thermodynamic analysis

For the different gasphase species, the following standard enthalpy of formations were obtained from NIST Standard Reference Database Number 69 ($\Delta_f H_{\text{NIST}}^\theta$) [40] and from DFT ($\Delta_f H_{\text{DFT}}$) calculations. These are shown in table 9.

Table 9: Enthalpie of formation calculated at standard conditions and using DFT.

| Species | $\Delta_f H_{\text{NIST}}^\theta$ [kJ/mol] | $\Delta_f H_{\text{DFT}}$ [kJ/mol] |
|-----------------------------------|---|---------------------------------------|
| H_2 | 0.00 | -632.52 |
| CO | -110.53 | -1411.03 |
| H_2O | -241.83 | -1311.98 |
| CH_4 | -74.80 | -2196.59 |
| CH_3OH | -205.00 | -2782.20 |
| CH_2CH_2 | 52.4 | -2945.62 |
| CH_3CH_3 | -84.00 | -3720.93 |
| CH_3CHO | -170.70 | -3637.18 |
| $\text{CH}_3\text{CH}_2\text{OH}$ | -234.00 | -4324.61 |

Using the values from table 9 and equation 39, we acquire the following enthalpies of formation:

Table 10: Reaction enthalpies from NIST Standard Reference Database Number 69 and as calculated with DFT.

| Reaction | $\Delta_r H_{\text{NIST}}^\theta$ [kJ/mol] | $\Delta_r H_{\text{DFT}}$ [kJ/mol] |
|--|---|---------------------------------------|
| $\text{CO} + 3 \text{H}_2 \rightleftharpoons \text{CH}_4 + \text{H}_2\text{O}$ | -206 | -200 |
| $\text{CO} + \text{H}_2 \rightleftharpoons \text{CH}_2\text{O}$ | -5 | -26 |
| $\text{CO} + 2 \text{H}_2 \rightleftharpoons \text{CH}_3\text{OH}$ | -96 | -106 |
| $2 \text{CO} + 4 \text{H}_2 \rightleftharpoons \text{CH}_2\text{CH}_2 + 2 \text{H}_2\text{O}$ | -210 | -217 |
| $2 \text{CO} + 5 \text{H}_2 \rightleftharpoons \text{CH}_3\text{CH}_3 + 2 \text{H}_2\text{O}$ | -347 | -358 |
| $2 \text{CO} + 3 \text{H}_2 \rightleftharpoons \text{CH}_3\text{CHO} + \text{H}_2\text{O}$ | -191 | -226 |
| $2 \text{CO} + 4 \text{H}_2 \rightleftharpoons \text{CH}_3\text{CH}_2\text{OH} + \text{H}_2\text{O}$ | -255 | -284 |

It can be seen from table 10 that all reactions, except for the reaction to acetaldehyde, are within a sensible range of 30 kJ/mol.

All activation barriers for the construction of the Reaction Energy Diagrams from chapter 4.1 are calculated by means of DFT. Therefore, it would make sense to use the reaction enthalpies from DFT as reference point. However, the ultimate goal is to reproduce experimental results, which would imply using the NIST values. Previous results showed that the temperature dependence of the reaction enthalpy seemed to be relatively small. For instance, at a temperature of 500K, the difference in energy was approximately be 10% or less.

4.3 Microkinetic simulations

The data, as was shown in section 4.1, was used to determine the surface coverages, product distributions, activation energies, order parameters of the reagents, and the determination of rate-limiting and rate-inhibiting steps, as a function of the temperature.

4.3.1 The Methanation reaction

For the microkinetic modeling of the methanation reaction, data from section 4.1.3 was used. Figure 30 shows the production of the products, as well as the reagents, for the methanation reaction on both rhodium 30a and ruthenium 30b.

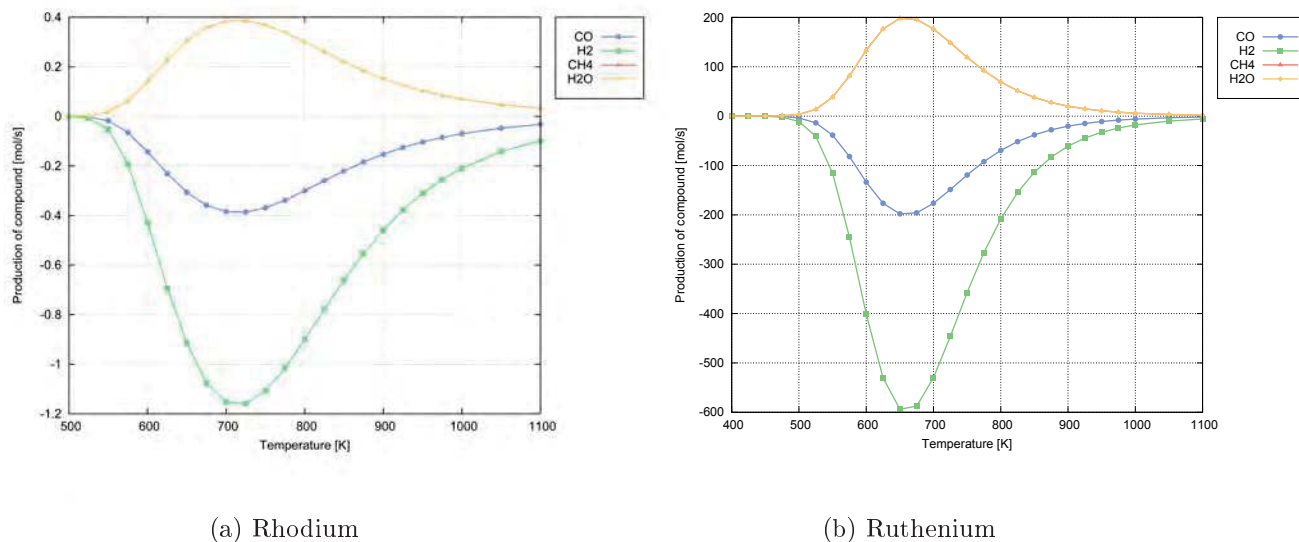
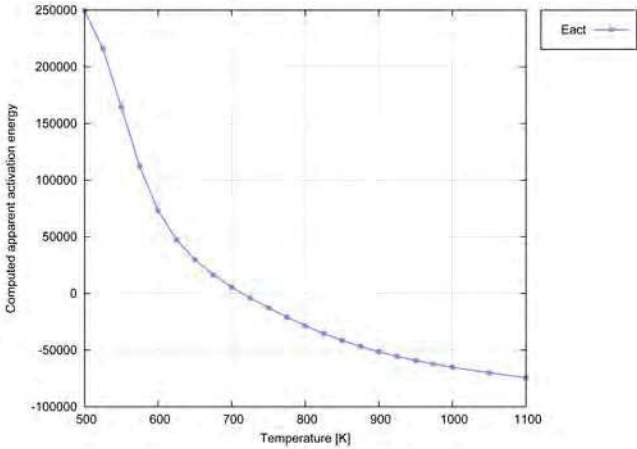


Figure 30: Production plots as a function of the temperature for the methanation reaction, acquired via microkinetic modeling for both rhodium and ruthenium.

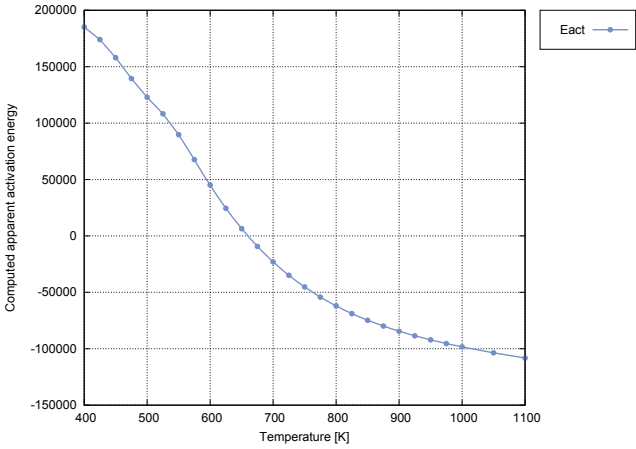
The products are formed, so production of them is positive. The reagents are being used in the reaction, so their production is negative. From the production plot, we can see no line for methane. The reason for this is that an equimolar amount of H₂O and CH₄ is formed, so the line for methane is lying exactly beneath the line for water. It can also be seen that the amount of H₂, which is consumed during the methanation reaction, is exactly three times the amount of the CO, which is being consumed. This coincides with the amount needed for the methanation reaction, since the ratio of CO to H₂ is one to three in the methanation reaction. The top of the production graph lies at around 720 K, which is rather high, but nevertheless a representable value for the methanation reaction.

When comparing the methanation reaction on rhodium with the methanation on ruthenium, it can be seen from the production plot that the production overall is higher. This is because ruthenium is much more active when it comes to breaking of the CO

bond. Because the CO bond is more easily broken, the methanation reaction can proceed faster, so the amount of product is higher than on rhodium. It can also be seen that the optimum for the methanation reaction on rhodium lies about 50 K higher than on ruthenium. This is due to the fact that the bond between carbon and ruthenium is stronger than the bond between rhodium and carbon.



(a) Rhodium

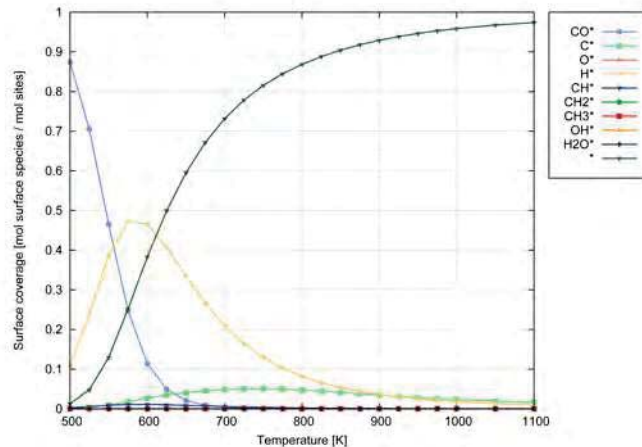


(b) Ruthenium

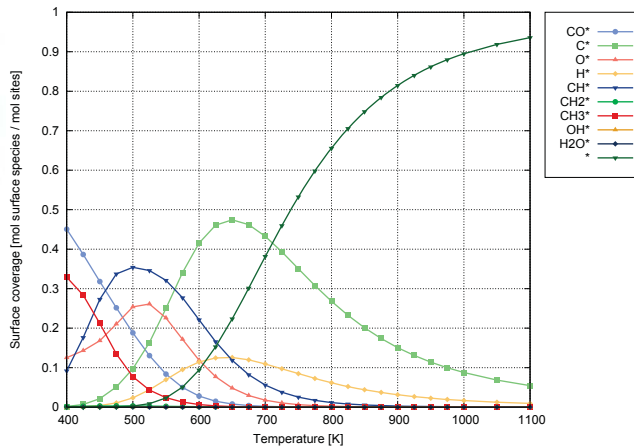
Figure 31: Activation energies as a function of the temperature for the methanation reaction, acquired via microkinetic modeling for both rhodium and ruthenium.

Figure 31 shows the activation energies of the reaction. From the activation energy plot, it can be seen that the plot will probably start horizontally. This maximum will lie above 250 kJ for rhodium and somewhere around the 200 kJ for ruthenium. This means that more than 250 kJ is needed for the reaction on rhodium to take place at low temperatures. This value is higher than the maximum reaction energy barrier, because there is a lot of CO on the surface at low temperature. In order to break this CO, an additional free site is needed. With low temperatures, the surface is full of CO and reaction cannot take place. So, unless a CO is desorbed to create a vacant site, the CO dissociation will not take place. This additional energy is due to this CO desorption. Moreover, it is shown that the apparent activation energy for rhodium is higher than for ruthenium. This also shows that the methanation reaction is more favorable on ruthenium than it is on rhodium. This coincides with the results that were already shown in the production plot in figure 30.

Figure 32 shows the surface coverage with respect to the temperature.



(a) Rhodium



(b) Ruthenium

Figure 32: Surface coverage of the different species as a function of the temperature for the methanation reaction, acquired via microkinetic modeling for both rhodium and ruthenium.

At low temperatures, the surface is predominantly covered by CO molecules. Also some atomic hydrogen is present on the surface. When temperature increases, the amount of empty sites increases. This makes it possible to split CO into C and O. Only direct CO dissociation is taken into account, so the methanation reaction proceeds from carbon only. The fact that only CO is present for low temperatures means that CO dissociation is rate limiting in this regime. This is also shown in figure 33a. At higher temperatures, the amount of hydrogen on the surfaces decreases significantly, making it harder to hydrogenate surface species like CH₃ and OH. Therefore, formation of water and methane become rate limiting at high temperatures. This coincides with the results shown in figure 33a.

In the case of ruthenium, there are already different species present at low temperatures on the surface. This means that CO dissociation happens relatively easy and is not a rate limiting step at low temperatures. CH₃ is present at low temperatures. This means that the formation of methane and the formation of water are rate limiting at low temperatures. With increasing temperature, the O species increases to a peak around 525 K, which coincides with the degree of rate control plot. It is shown in figure 33b that the water formation is rate limiting in this same regime. As was the point with rhodium, with ruthenium the hydrogen coverage decreases at higher temperatures as well. This has the same result, making both termination to water and methane rate limiting. This is also shown in figure 33b.

Figure 33 shows the rate limiting and rate-inhibiting reactions when the values are positive and negative, respectively.

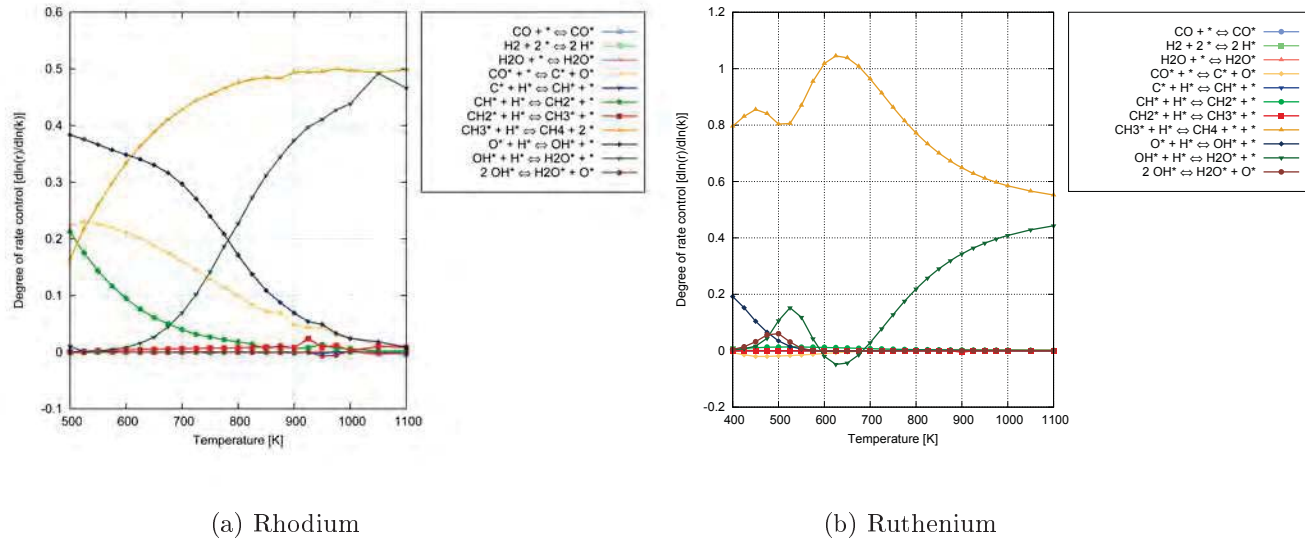
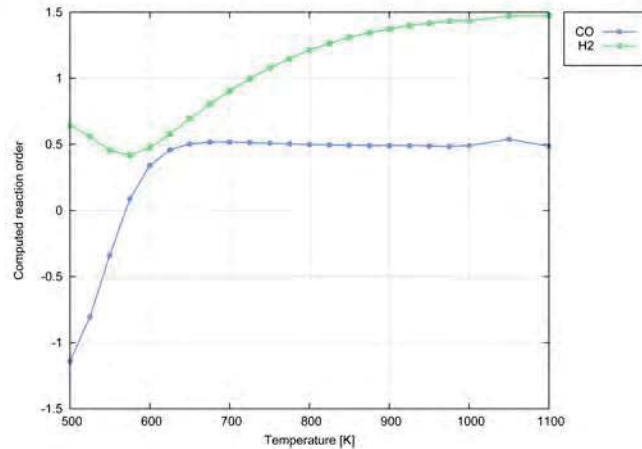


Figure 33: Degree of rate control as a function of the temperature for the methanation reaction, acquired via microkinetic modeling for both rhodium and ruthenium.

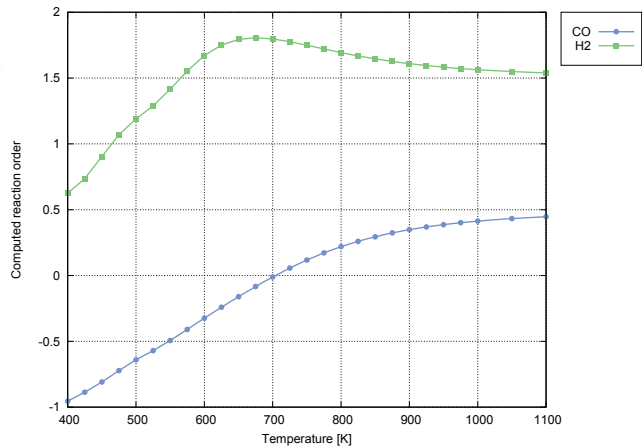
From the degree of rate control for rhodium, as shown in figure 33b, we can conclude that OH and CH₂ formations are rate limiting when the temperature is low. Because of the low temperatures, there is a large amount of CO adsorbed and only a small amount of hydrogen. Furthermore, there is very limited O on the surface to hydrogenate. This is also shown in the surface coverage plot. Next to OH and CH₂ formation, the CO dissociation is rate limiting at low temperatures as well. This is due to the small amount of vacant sites on the surface, because CO needs an additional site in order to dissociate. At higher temperatures, OH hydrogenation is rate limiting, as well as methane formation. These two reactions are in competition for the hydrogen, since the hydrogen content decreases after 800 K beneath 10 percent, as shown in the surface coverage plot. Therefore, both reactions have a value of 0.5 for the degree of rate control. Furthermore, it can be noticed that there are no rate-inhibiting reactions in the methanation reaction, since all degree of rate control values are positive.

For ruthenium at low temperatures, only the methane formation and the OH formation are rate limiting, since hydrogen species are not yet present on the surface. CH₃ is readily formed, because CO dissociation can already take place for low temperatures. For high temperatures, the rate limiting steps are the same as for rhodium, because the surface coverage of hydrogen is low on ruthenium as well. Therefore, there is competition for the hydrogen, resulting in a degree of rate control of 0.5 for water and methane formation, as well.

Figure 34 shows the orders in H₂ and CO as a function of the temperature.



(a) Rhodium

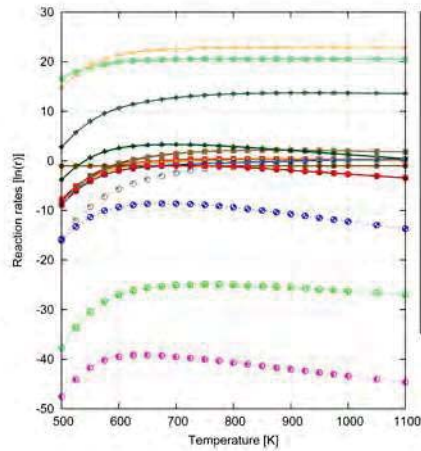


(b) Ruthenium

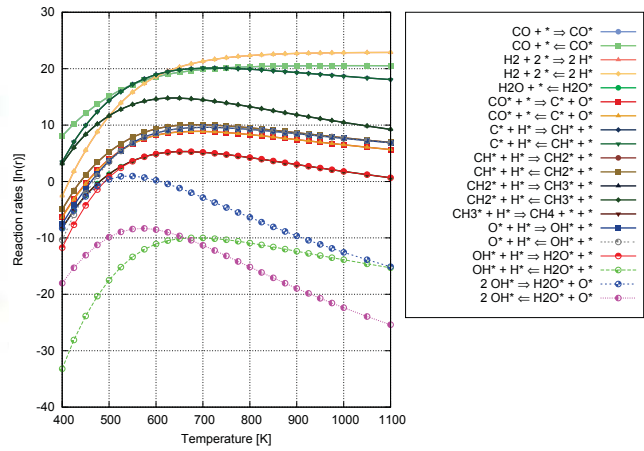
Figure 34: Orders as a function of the temperature for the methanation reaction, acquired via microkinetic modeling for both rhodium and ruthenium.

From figure 34a and 34b, it can be seen that the reaction order in CO starts at around -1. This is due to the fact that CO dissociation is at this point a rate limiting step, since there are nearly no vacant sites at lower temperature. The order in CO will increase to 0.5, as would be expected. The order in H₂ starts at 0.5 at low temperature. For high temperatures, the order will increase to 1.5. Hence, for the formation of methane, the order in hydrogen is 2, since it CH₄ formation is the rate limiting step. The order is determined by the rate limiting step, and the reactions leading to this rate limiting step. All steps after the rate limiting step are kinetically irrelevant. For the formation of water, the order in hydrogen is 1. Since both reactions are rate limiting for high temperatures, the order in hydrogen becomes the averaged value of both orders, which is 1.5. This is the same for rhodium as well as ruthenium, since for both reactions the rate limiting steps are the same at high temperatures.

Figure 35 shows the natural logarithm of the reaction rate. Values that are negative do not occur frequently, while positive reaction rates mean that the according reaction is dominant. This is a powerful tool to check the most dominant reactions.



(a) Rhodium



(b) Ruthenium

Figure 35: Reaction rates as a function of the temperature for the methanation reaction, acquired via microkinetic modeling for both rhodium and ruthenium.

It can be concluded from figure 35, that most reaction rates coincide for both transition metals. It is shown that the formation of two hydroxy species from water and oxygen is the least occurring reaction in the methanation reaction, followed by the production of hydrogen and a hydroxy species from water. It can also be seen that the adsorption and desorption reactions are the most dominant reactions, followed by the CH formation. The rest of the reactions lie in between.

The methanation reaction on rhodium was also investigated for the case of hydrogen assisted CO dissociation. These results were found to match with the direct CO dissociation. It can be seen that this is the case when comparing the rates involving the direct CO dissociation to the hydrogen assisted CO dissociation pathways, as was done in figure 36.

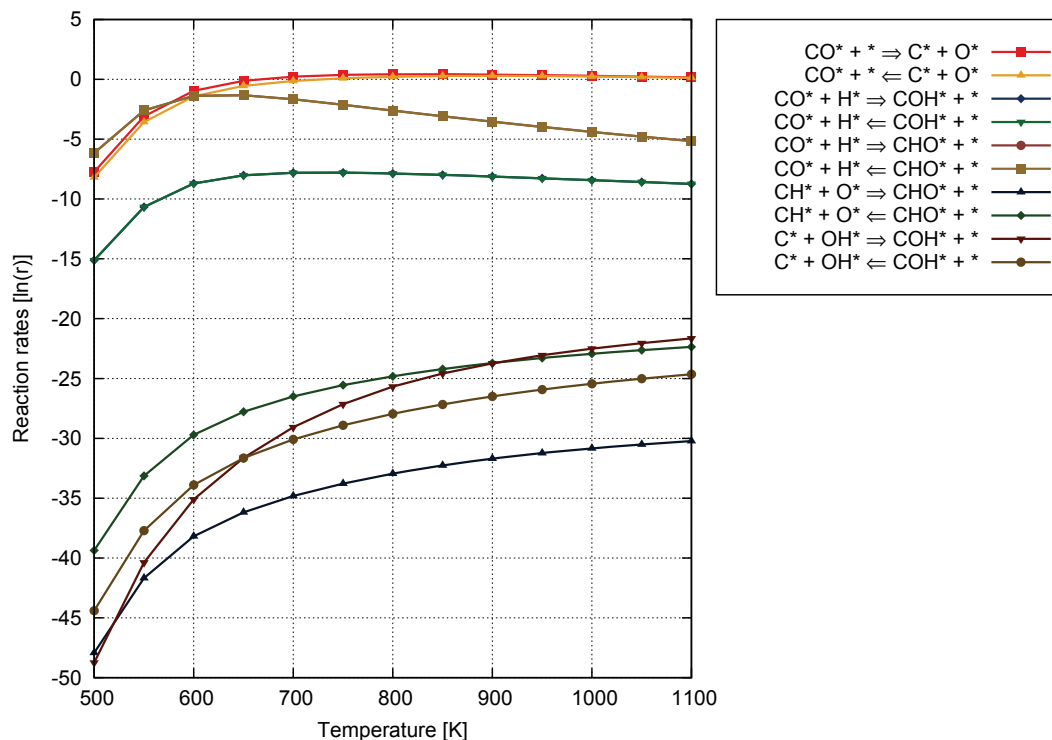


Figure 36: Reaction rates as a function of the temperature for the methanation reaction, acquired via microkinetic modeling for the hydrogen assisted CO dissociation on rhodium.

It can be seen that the rates for direct CO dissociation are far higher than the rates for the hydrogen assisted CO dissociation. This was already shown from DFT calculations in section 8.1 and is confirmed by microkinetics. From this the conclusion can be drawn that the CO dissociation on stepped rhodium proceeds via the direct CO dissociation pathway.

4.3.2 The production of Methanol

For the microkinetic modeling of the reaction towards methanol, data from section 8.4 was used. With these data, no methanol was produced. Therefore, some reconsiderations were made regarding the reaction energies. It was also considered a condensed phase for methanol under the pressures and temperatures, which were used. Therefore, a new value of -147 kJ/mol was calculated as this new reaction enthalpy. By comparing the reaction energy diagrams for methane and methanol, CH_2O was set more stable by 40 kJ/mol. Also the reaction from CH_2O to CH_3O was adjusted downwards in forward and backward reaction energy. The termination reaction from CH_3O was set higher in energy for the forward reaction energy. These reconsiderations were made, based on

values reported from the Literature. When formation of methane is less energetically favorable, the production of methanol can take place. This is also graphically shown in figure 37. The reconsidered data are shown in table 11.

Table 11: Reconsiderations of some elementary reaction steps for the formation of methanol.

| # | Elementary Reaction Steps | E_f [kJ/mol] | E_b [kJ/mol] |
|----|---|----------------|----------------|
| 91 | $\text{CH}_2\text{O}^* + \text{H}^* \leftrightarrow \text{CH}_2\text{O}^* + *$ | 75 | 44 |
| 92 | $\text{CH}_2\text{O}^* + \text{H}^* \leftrightarrow \text{CH}_3\text{O}^* + *$ | 48 | 12 |
| 93 | $\text{CH}_3\text{O}^* + \text{H}^* \leftrightarrow \text{CH}_3\text{OH}^* + *$ | 68 | 7 |

These reconsidered data can be plot against the data for methane formation in a reaction energy diagram. This reaction energy diagram is shown in figure 37.

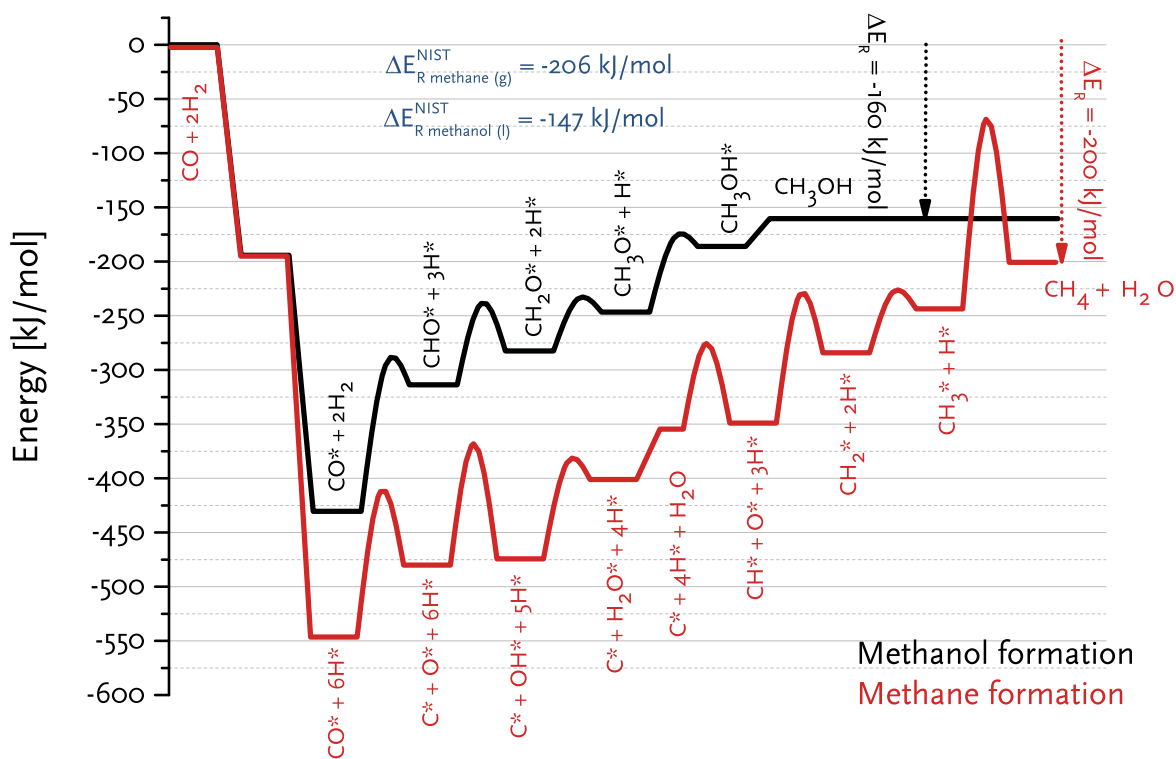
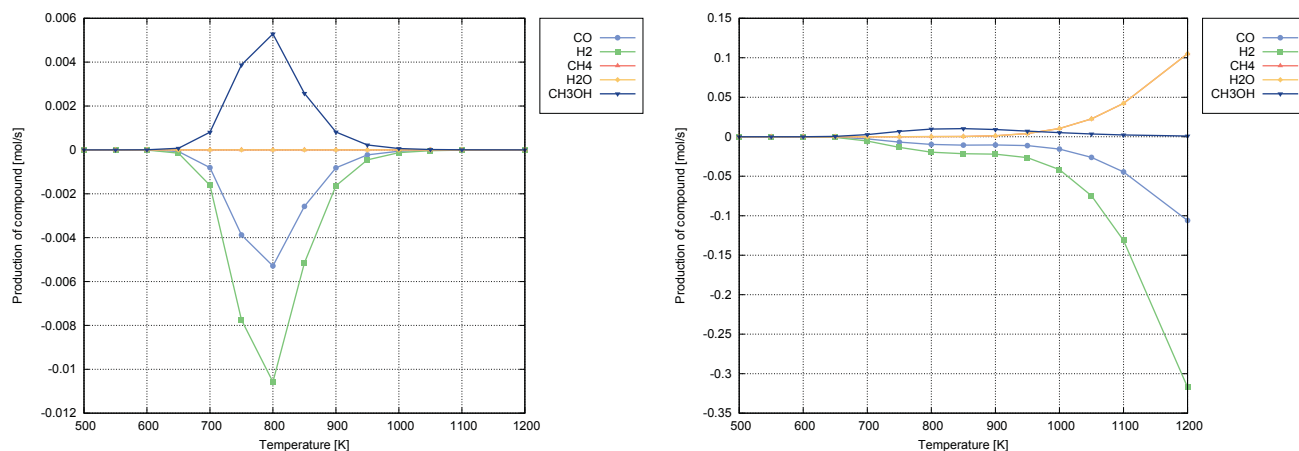


Figure 37: Reaction energy diagram for methanation and the formation of methanol.

It can be seen that, next to the values that have been changed for methanol, also the termination step of methane was changed by 100 kJ/mol. This was done, because the difference in total forward reaction energy for methane (275 kJ/mol) and methanol (350 kJ/mol) is approximately 75 kJ/mol. Since the methane energy diagram lies higher in energy then the energy diagram for methanol, it is now thermodynamically possible to produce methanol in a microkinetic model.

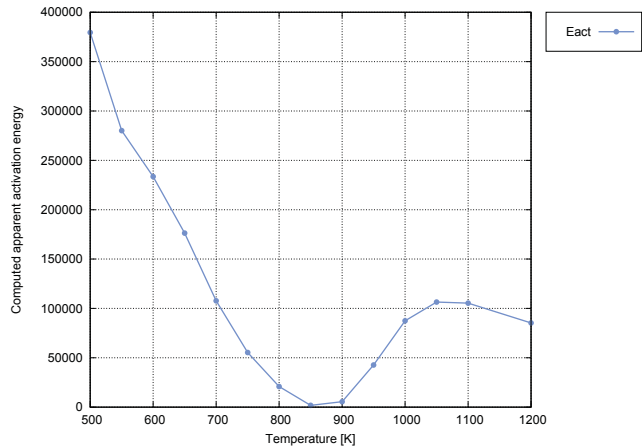
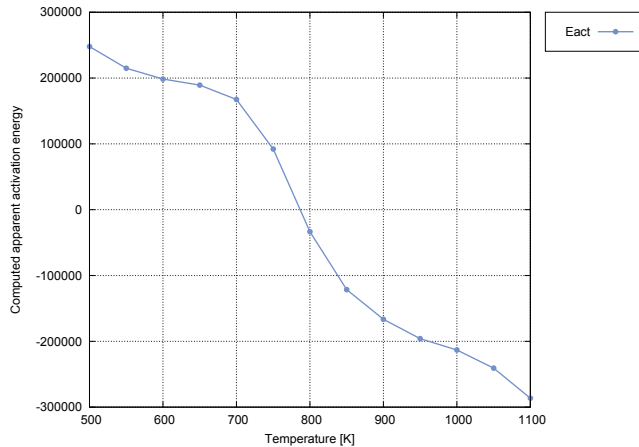
Figure 38 shows the production of the products, as well as the reagents, for the reaction to methanol rhodium. Figure 38a shows the hydrogenation of CO, without CO dissociation, thus without methanation, and figure 38b shows the full set of equations for the production of methanol and methane..



(a) The production of methanol via CO hydrogenation (b) The production of methanol via all possible pathways

Figure 38: Production plots as a function of the temperature for the reaction towards methanol, acquired via microkinetic modeling for both the hydrogenation of CO as the full set of reactions.

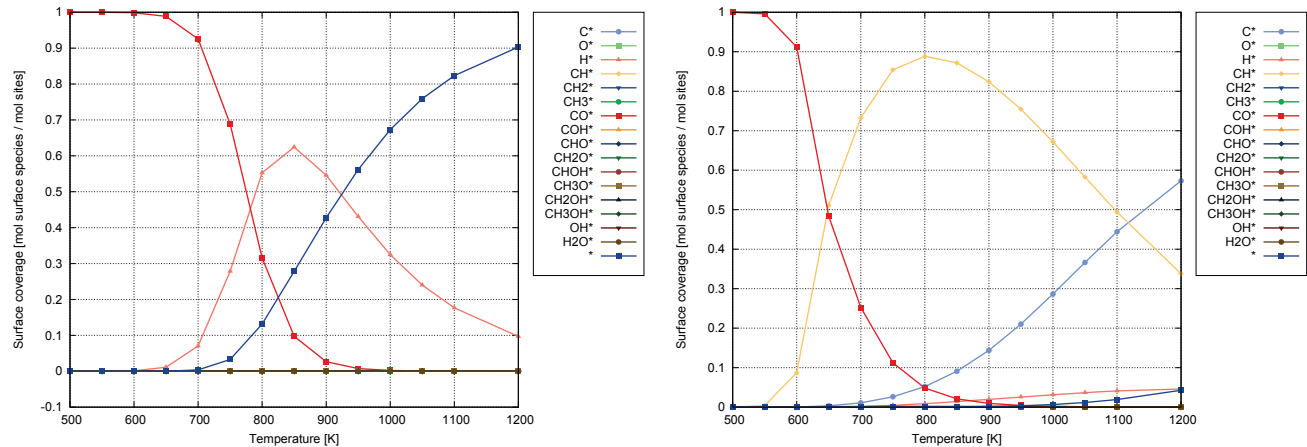
From the production plot it can be seen that the optimum lies around 800 K for the CO hydrogenation and around the 850 for the production of methanol via different pathways. The production of methanol is roughly the same for both graphs. The consumption of reagents lies higher at a higher temperature regime, when looking at the production plot from figure 38b. This is because in this system, besides from methanol, also methane is formed. Methane production starts off later, since at the lower temperature regime, all CO is hydrogenated instantly and no methane is being formed, because there are no empty sites for CO dissociation, while there is hydrogen on the surface to generate methanol. When empty sites occur on the surface, the production of methane sets in. In figure 40b it can be seen that the first vacant sites occur at 900 K, which coincides with the first production of methane in the production plot.



(a) Activation energy for the production of methanol via CO hydrogenation (b) Activation energy for the production of methanol via all possible pathways

Figure 39: Activation energy as a function of the temperature for the reaction towards methanol, acquired via microkinetic modeling for both the hydrogenation of CO as the full set of reactions.

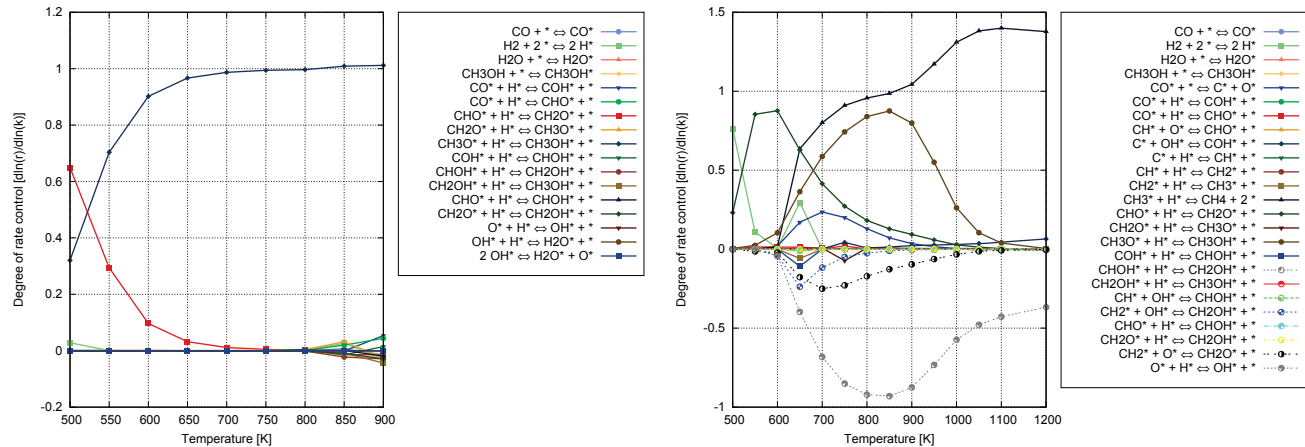
It can be seen from the activation energies, that the direct hydrogenation occurs more easily, since the activation energy is not as high. We can also see from figure 39a that the optimum lies at approximately 780 K, since the graph passes 0 at this temperature. Figure 39b will show two points at which the activation energy will be 0, since the graph from figure 38b shows two peaks; one for the formation of methanol and one for the methane formation. The occurrence of these two peaks lies in the fact that the concentrations are considerably low, so the microkinetic equations become harder to solve for the program. This is the main problem for doing microkinetics in the regime, where productions are small. For these calculations, the solver needs to be very accurate, since the concentrations can get as low as the tolerance of the solver. When concentrations get below this tolerance, the solver can break.



(a) The surface coverage for the production of methanol via CO hydrogenation (b) The surface coverage for the production of methanol via all possible pathways

Figure 40: The surface coverage as a function of the temperature for the reaction towards methanol, acquired via microkinetic modeling for both the hydrogenation of CO as the full set of reactions.

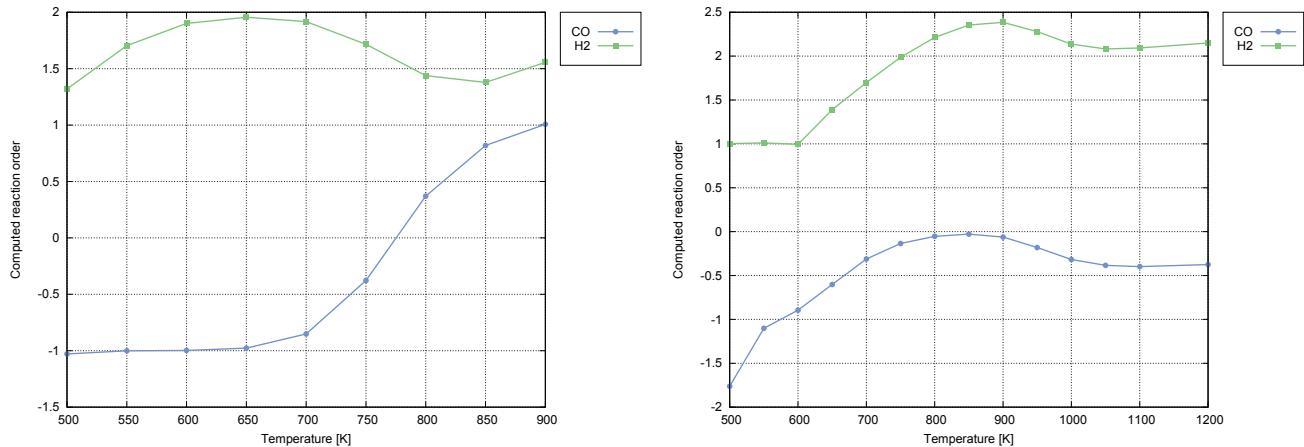
From the surface coverage plot, we can see the dominant species that are present on the surface. When looking at figure 40a, the dominant product at low temperatures is CO. This is because CO dissociation cannot take place because of the lack of vacant sites. Around the optimum, there is approximately the same amount in CO as is in hydrogen, which can be expected. With higher temperatures, the surface is almost empty, which is as expected. From the surface coverage plot in figure 40b we can see that there is a lot of CO at lower temperatures. This CO is probably dissociated via the CHO species, since this species has become more stable with the alterations in the dataset and therefore the most probable manner to split CO. Since there is no hydrogen present on the surface, and there are hydrogenated species present at lower temperatures, all hydrogen is immediately used for hydrogenation of CO to CHO. The CHO then continues its path to methanol at lower temperatures, since it is produced at lower temperatures, and at higher temperatures, it will split in CH and O. From this point on, it can be hydrogenated to methane and water, which are produced at higher temperatures.



(a) Degree of rate control for the production of methanol via CO hydrogenation (b) Degree of rate control for the production of methanol via all possible pathways

Figure 41: Degree of rate control for the production plots as a function of the temperature for the reaction towards methanol, acquired via microkinetic modeling for both the hydrogenation of CO as the full set of reactions.

For the degree of rate control for the CO hydrogenation, as shown in figure 41a, it can be seen that the CH_2O production is rate limiting at lower temperatures. This is because there is only a little amount of hydrogen adsorbed on the surface, since the surface is almost completely covered with CO. At higher temperatures the termination reaction gets rate limiting. Hydrogen is also needed for this reaction. At higher temperatures there is no hydrogen left on the surface, so desorption will become rate limiting. It can further be noticed that there are no real rate inhibiting steps. The degree of rate control for the case of methanation and methanol formation, as shown in figure 41b, becomes more complicated. At lower temperatures it is shown that, next to hydrogen adsorption, also the CH_2O formation is rate limiting. The latter formation was also rate limiting in the case of CO hydrogenation. around the optimum for methanol formation, the rate limiting reactions become the termination from CH_3O to methanol, as was the case for CO hydrogenation. Besides from the termination to methanol, also the termination to methane is becoming to get more rate limiting at this temperature. Next to the rate limiting steps, also a rate inhibiting step, which is the OH formation, is present at this temperature. This reaction becomes rate inhibiting at this temperature, because it competes for oxygen with the methanol, so reaction to OH will slow the reaction down. If OH formation would be less favorable at this temperature, the methanol formation would be higher. At higher temperatures, methane formation is becoming the sole rate limiting step. This was also one of the rate limiting steps in the methanation reaction in figure 33a. The removal of oxygen is not rate limiting anymore, since oxygen reacts easily to methanol.



(a) Orders for the production of methanol via CO hydro- (b) Orders for the production of methanol via all
 generation possible pathways

Figure 42: Orders in hydrogen and CO as a function of the temperature for the reaction towards methanol, acquired via microkinetic modeling for both the hydrogenation of CO as the full set of reactions.

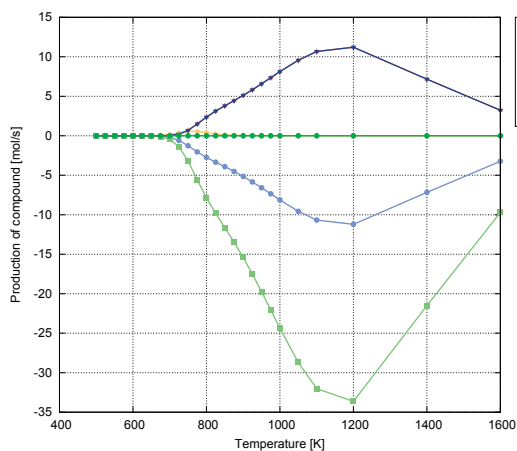
The order plot shows that the order in CO starts at -1 and the order in hydrogen at around 1. At low temperatures, CHO hydrogenation is rate limiting at low temperatures. This corresponds with the order in CO, since CHO hydrogenation is dependent on CO by a factor of one. There is no hydrogen adsorbed on the surface at low temperatures. At higher temperatures, the order in CO is 1, since there is no CO left on the surface at these temperatures. The order in hydrogen goes to 1 as well at higher temperatures. For the order plot from figure 42b, Hydrogen starts at 1 as well, because also in this dataset, hydrogen is not yet adsorbed. The order in CO probably starts at -1 as well, since the first point in the order plot is an outlier. The fact that the order is -1 in CO is due to the same fact as was in the case with the CO hydrogenation case from figure 42a. At high temperatures, the order in H₂ becomes 2, while the order in CO becomes -0.5. The fact that the order for hydrogen becomes two has to do with the fact that the termination step to methane is rate limiting at higher temperatures. Since this termination is dependent on 3 reactions that are dependent on hydrogen as well, the total order for termination is 2 in hydrogen. The order in CO is -0.5 at higher temperatures. At this temperature regime, termination of methane is rate limiting and the formation of OH is rate inhibiting. The rate inhibiting step has a great influence on the order in CO, since the order in CO would be 0.5 if there was no rate inhibiting step, as was the case for the methanation reaction, as seen in figure 34a.

4.3.3 The production of C₂–Oxygenates

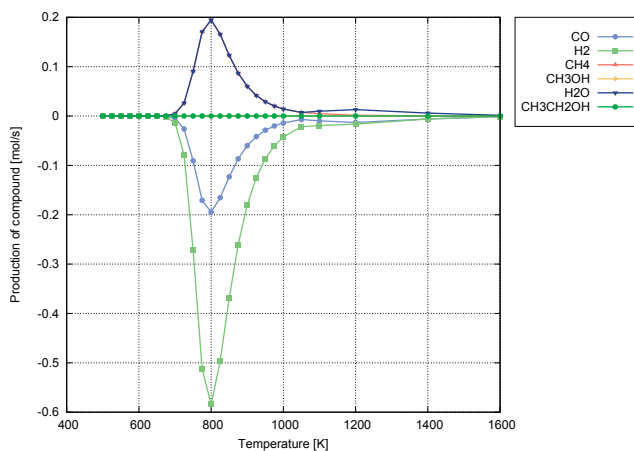
For the production of ethanol, the dataset from van Rijn et. al. [12], as well as our own data, was checked. This dataset consisted of three different papers with values for

the production of ethanol, methanol and methane. As suggested, the adsorption and desorption reactions were performed with Hertz-Knudsen kinetics instead of Arrhenius equations. This gave reasonable different results from the microkinetic model as presented in her thesis.

Two different datasets, denoted as dataset E5 and E6, were looked at. The production plots of these datasets are shown in figure 43. It can be seen in figure 43a, that there is formation of methanol at lower temperatures, which peaks around 750 K. This is in good agreement with the data from van Rijn et. al. Although there is some formation of ethanol, it is not in good comparison to the results from van Rijn et. al. The fact that methane formation starts later is in agreement, as is the fact that methane formation is approximately 50 times more at its maximum. It can be seen from dataset E6 in figure 43b, that the optimum lies much lower in energy. However, there is no production of oxygenates apart from water visible in the graph. This means that the production of methanol and ethanol is low or even absent.



(a) The production plot for dataset E5

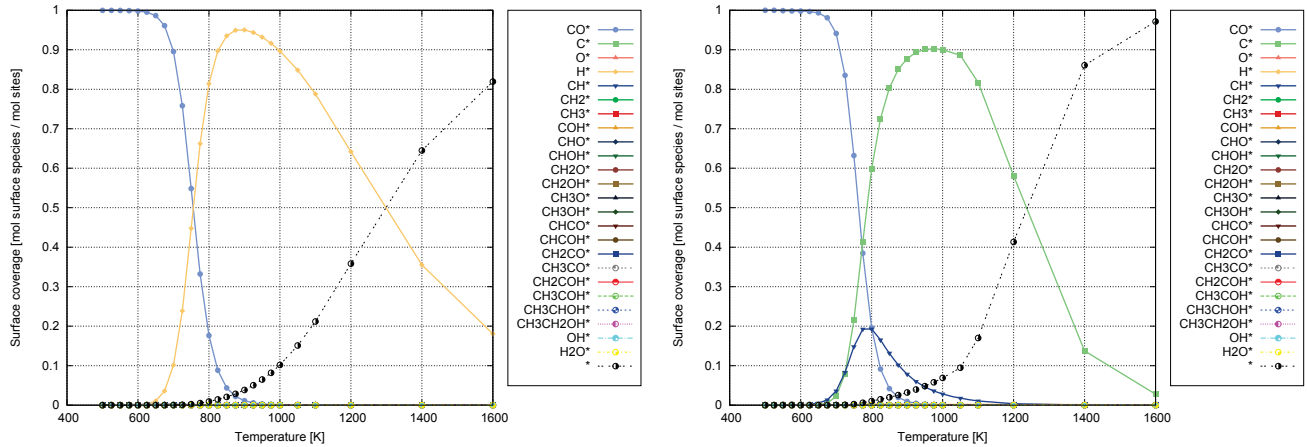


(b) The production plot for dataset E6

Figure 43: Production plots as a function of the temperature for dataset E5 and E6 taken from van Rijn et. al. [12], acquired via microkinetic modeling for both the hydrogenation of CO as the full set of reactions.

Figure 44 shows the orders in H_2 and CO as a function of the temperature. In the case that there is formation of methanol, the amount of free sites is zero, while there is CO and hydrogen on the surface. From this we can conclude that the hydrogenation of CO will probably be the most probable pathway for low temperatures. When the amount of free sites increases, the CO dissociation can start to take place, resulting in the formation of methane. After the optimum temperatures, the surface becomes empty. This is as would be expected. In the case of dataset E6, there is a considerable amount of carbon on the surface. This means that CO dissociation has taken place at lower

temperatures, so the hydrogenation of CO did not occur as much as in the case of dataset E5. Therefore, no methanol was seen in the production plot from dataset E6. At the optimum temperature, the hydrogen coverage is at its peak, which is as expected. After this temperature, the amount of hydrogen drops. At high temperatures, the surface becomes empty again.

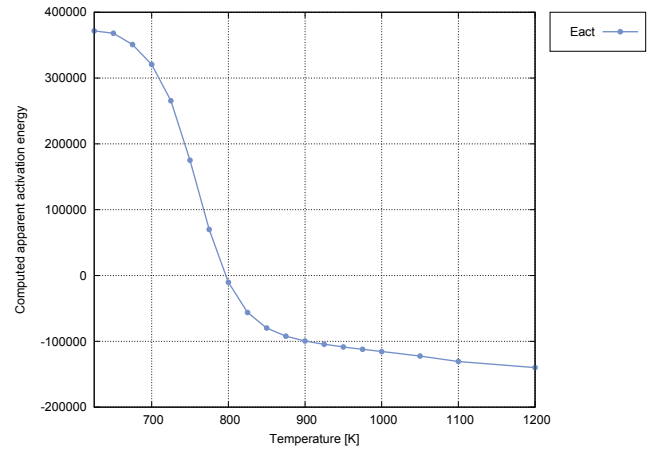
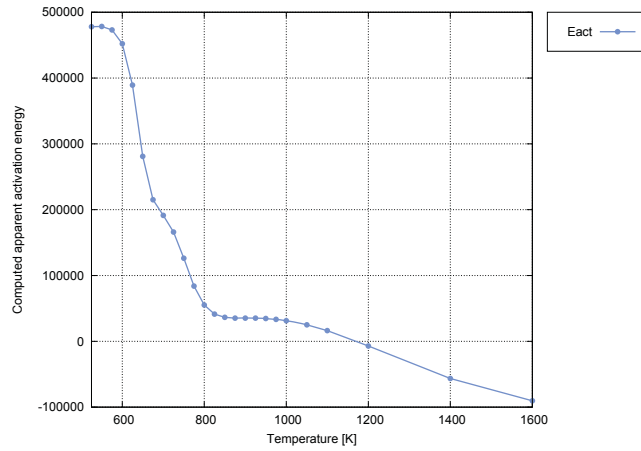


(a) The surface coverage for dataset E5

(b) The surface coverage for dataset E6

Figure 44: The surface coverage as a function of the temperature for dataset E5 and E6 taken from van Rijn et. al. [12], acquired via microkinetic modeling for both the hydrogenation of CO as the full set of reactions.

Figure 45 shows the orders in H_2 and CO as a function of the temperature. From the order plot it can be seen that the optimum for dataset E5 lies around 1200 K, while the optimum for dataset E6 lies at 800 K, which coincides with the production plots in figure 43. It can further be noted that the activation energy at dataset E5 lies considerably higher than the activation energy in dataset E6, with a difference of 100 kJ/mol. From this it can be concluded that more energy is needed for the reaction towards methanol.

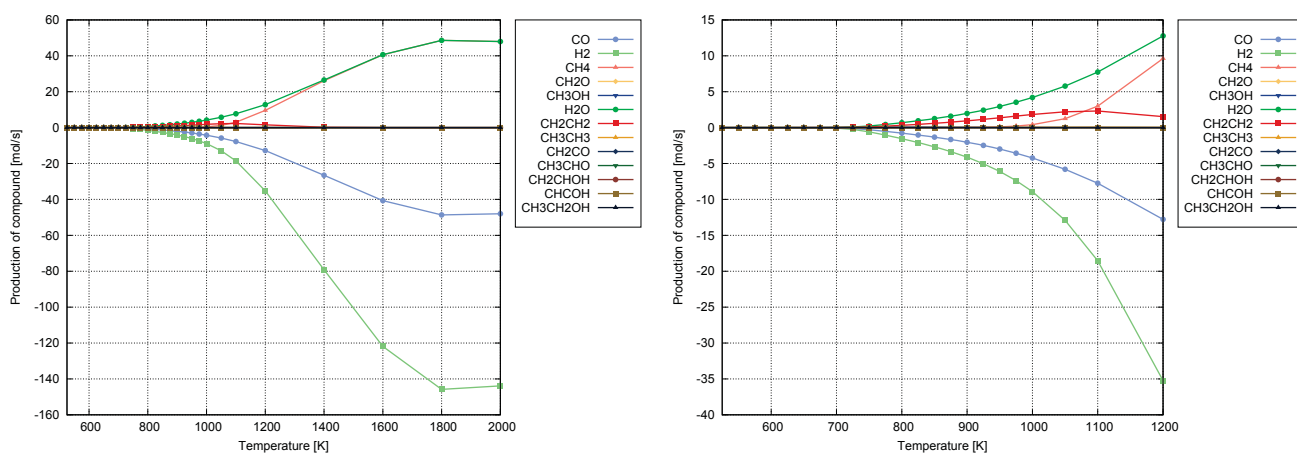


(a) The activation energy for dataset E5

(b) The activation energy for dataset E6

Figure 45: The activation energy as a function of the temperature for dataset E5 and E6 taken from van Rijn et. al. [12], acquired via microkinetic modeling for both the hydrogenation of CO as the full set of reactions.

Our own results were also put in a microkinetic model. Reaction energies were not changed, except for the desorption of methane, which was increased by 100 kJ/mol. Otherwise, all microkinetic calculations would only yield methane. It can be seen from figure 46 that the production of methane is dominant, as was seen from the microkinetic simulations from van Rijn et. al. Figure 46b shows the same data the 46a, but in a smaller temperature range. From figure 46b we can see that ethylene is product at lower temperatures. There is only little production of oxygenates. From this we can conclude that the coupling of two carbon species is more favorable then the insertion of a CO or the hydrogenation of CO, to produce ethanol and methanol, respectively. At higher temperatures, methane is being produced. It must be noted that the temperatures at which the production of the compounds takes place is not very realistic, since the surface should be empty around 1000 K.

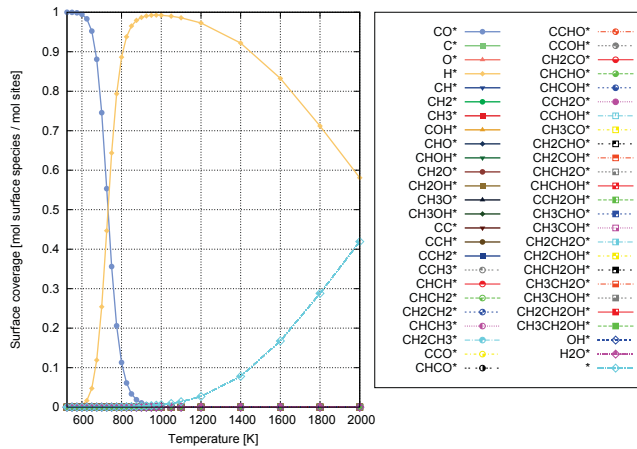


(a) Full temperature range

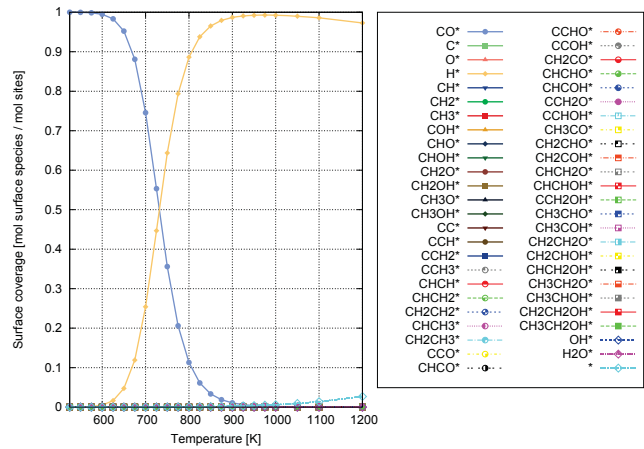
(b) Temperature regime to 1200 K

Figure 46: Production plots as a function of the temperature for the full temperature range and a zoom in, acquired via microkinetic modeling for both the hydrogenation of CO as the full set of reactions.

From figure 48 it can be seen that at low temperatures, the surface is covered with CO. When temperatures increase, the surface is predominantly covered by hydrogen. This hydrogen is desorbed only at high temperatures, where empty sites are being created. The hydrogen desorption is not very representable, since desorption starts after 1000 K, while in reality, the surface would be empty.



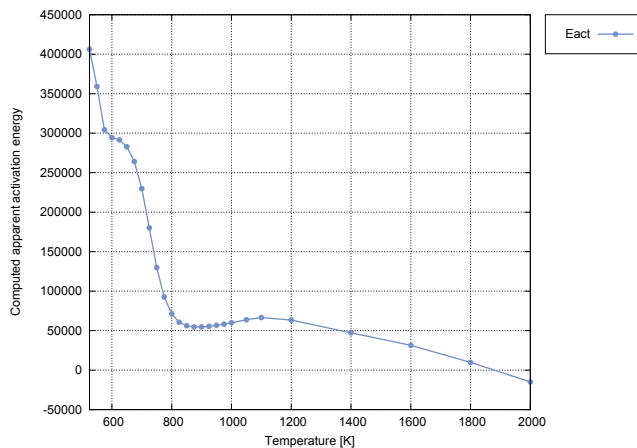
(a) Full temperature range



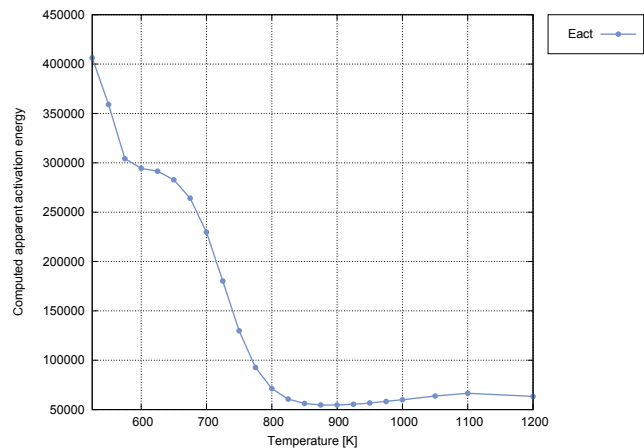
(b) Temperature regime to 1200 K

Figure 47: Surface coverage plots as a function of the temperature for the full temperature range and a zoom in, acquired via microkinetic modeling for both the hydrogenation of CO as the full set of reactions.

As can be seen from the activation energy plots, there is a slight increase in activation energy between 800 K and 1100 K. This is due to the optimum for ethylene formation, which does not coincide with the optimum for methanation. It can further be seen that the total activation energy starts around 300 kJ/mol, since the first point is an outlier.



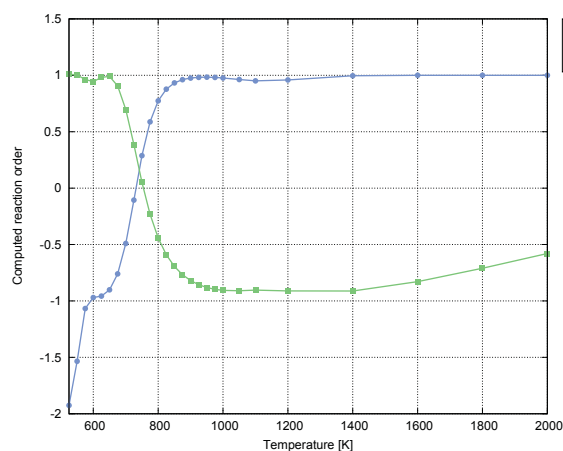
(a) Full temperature range



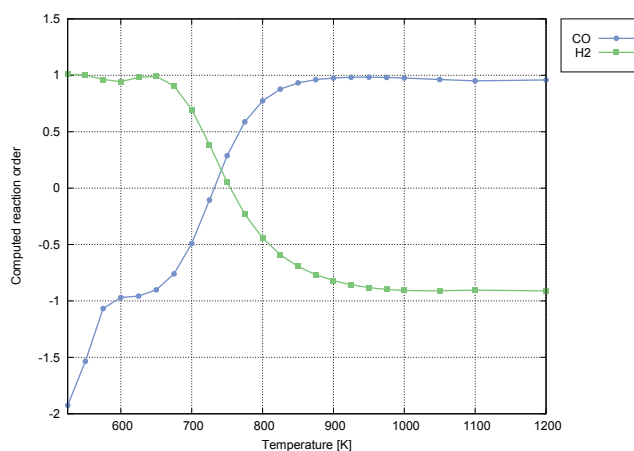
(b) Temperature regime to 1200 K

Figure 48: The activation energy as a function of the temperature for the full temperature range and a zoom in, acquired via microkinetic modeling for both the hydrogenation of CO as the full set of reactions.

The plots of the orders in hydrogen and CO are shown in figure 49. It can be seen that in the low temperature regime, the order for hydrogen equals 1. This is because at low temperatures, there is no hydrogen adsorbed on the surface. The order in CO starts at -1, from which we can conclude that the surface is full with CO, which is not able to desorb or react, since there are no free sites or hydrogen present at these temperatures. When looking at the high temperatures, there is almost no difference between the order in CO. The order in CO for high temperatures is 1, since there is no more CO present on the surface. For hydrogen, it can be seen that the order is around the -1 and starts to increase slightly for temperatures higher than 1400 K. From here the desorption of hydrogen starts to take place.



(a) Full temperature range



(b) Temperature regime to 1200 K

Figure 49: Orders in hydrogen and CO as a function of the temperature for the full temperature range and a zoom in, acquired via microkinetic modeling for both the hydrogenation of CO as the full set of reactions.

5 Conclusions

In this study, the synthesis of C_2 -Oxygenates on Rh-catalyzed Fischer-Tropsch synthesis, as well as C_2 -Hydrocarbons, C_1 -Oxygenates, and methane from syngas was looked at by DFT and by microkinetic modeling. By doing all DFT calculations, the problem of combining the right thermodynamics from different datasets can be resolved. The goal is to determine the most favorable pathways for the formation of these products, look at the rate limiting steps in the reaction scheme, try to reproduce the production of the species formed in experiments and to check the reported values from the Literature.

The DFT calculations help to find the most energetically favored intermediates and show the most dominant pathways. It is also shown from the DFT calculations, that the position of the adsorbed species on the catalyst plays an important role, when looking at the reaction energy. As important are the coupling sites and the manner in which the species are adsorbed to the surface.

The first conclusion that can be drawn from the DFT calculations arises from the calculations for the CO dissociation, since the CO dissociation is a key reaction for the formation of ethanol, as well as methane and C_2 -Hydrocarbons. CO bond scission was proven to be easier for the CHO species. However, the direct CO dissociation had a lower overall barrier for the production to CH_2 species. This leads to the conclusion that CO dissociation on stepped rhodium will proceed via a direct CO-dissociation and not via a hydrogen assisted pathway.

The next conclusions that may be drawn from DFT were about the methanation reaction on rhodium, which was compared to the methanation reaction on ruthenium. From this comparison it was shown that the CO species on rhodium, in contrary to what is the case on ruthenium, is more stable than the C and CH species. Therefore, the production of C_2 -Oxygenates is a possibility, since CO insertion is needed for this reaction.

The production of formaldehyde was shown to proceed via the hydrogenation of CO and not via a CO dissociation, combined with a C-O or C-OH coupling. The production of methanol proceeds via the methoxy pathway, where the termination step is the hydrogenation of the oxygen. Comparing the formation of methanol with the Literature showed flaws on both sides. The total reaction energy from the Literature was not close to the experimental value, as was the case for own calculations, while some reactions in the Literature were found to be energetically more favorable. In the Literature, the values for the formation of methanol were not migration corrected. This was found when comparing both hydroxyl and methoxy pathways. Therefore, it is hard to compare both datasets.

Earlier work showed that it was not possible to couple two carbon species on the surface and form CC. This turned out to be the most favorable coupling that can be made on stepped rhodium. For ethane formation, the CC coupling pathways to $CHCH_3$ were taken into account, since this is a common intermediate. It was shown that for the

formation of this species, the CH-CH₃ coupling was the most favorable pathway. For the production of ethylene, it was found that the indirect route, via CH₂CH₃ was also a feasible pathway.

For the formation of longer oxygenates, the coupling of a CO to a CH species is necessary. There is no real dominant CH_x-CO coupling pathway, since the coupling of CH₂-CO needs the least energy, but the formation of CH₂ species needs more energy than the formation of C or CH species. The overall energy barriers lie close to each other. Therefore, CHCO is the most probably manner to insert CO, since it has the lowest overall energy barrier to CH₂CO species. For the production of ethanol, the ethoxy pathway 1 was found to be overall the least in energy demanding. The total energy for this reaction still was found to be higher than the total energy of reaction for ethylene or methane. With these data, it is not possible to simulate the production of ethanol, when species are taken with at an infinite distance to each other, as was done with our migration correction. Co-adsorption must be taken into account in order to get more reliable data, because with co-adsorption, all surface species are less stable on the surface, making it possible to access otherwise inaccessible states. It is also proven that the conformation of the surface species plays an important role. A better conformation of these species can lead to a more favorable reaction.

By microkinetic modeling, the rate limiting and rate inhibiting steps were determined, as well as the surface coverage, reaction orders in the reagents, activation energy, reaction rates, and the production rates of the different reaction components. By modeling of the full set of reactions, it was shown that the formation of methane was the most dominant pathway in general. When methane formation is set taken significantly (100 kJ/mol) less favorable, ethylene was dominant with lower temperatures. This indicates that there must be another coupling pathway, at which ethanol is formed. This leads to the conclusion that propagation probably proceeds through CO insertion, while termination to oxygenates goes via the coupling of an oxygen.

6 Outlook

It is not only important to look back at what is done in this study, but it is also valuable to look forward and make recommendations for further research.

For future DFT calculations, it will be wise to check other sites for coupling reactions, not only the lowest coordinated sites, as was done in this thesis. Since ethylene is quite easily formed, one can also look at the coupling between C₂-hydrocarbons and oxygen or hydroxide species. It may also be possible to check whether COH insertion takes place. Another possibility is that co-adsorption can help to make previously inaccessible states more accessible by lessening the binding strength of the surface with the adsorbed species. Also the lateral interactions can be taken into account. Final suggestion is to check the possibility for the CH₃-CO coupling and its hydrogenation possibilities, since this reaction was not taken into account. It might also be a good idea to check whether there are possible coupling reactions of C₂-hydrocarbons with oxygen or hydroxyl species, for the coupling of a oxygen species with CHCH₂ turned out to be in the same range as the insertion of a CO.

It may be possible to do a more extensive microkinetic study, since only a fraction of what could be done is studied. Microkinetic simulations themselves could be improved with a CO fit function, which was present in the previously used matlab script. It also turned out to be quite helpful to look at the degree of rate control, to get insights into the rate limiting steps of the system.

Another method which could be performed is a BEP analysis. This can relate changes made in the adsorption reaction with all following reaction steps. Further research could give more insights into the mechanisms as described in this thesis.

7 Acknowledgements

I would like to thank my supervisor, Ivo Filot, for the guidance he has given me during this project. You learned me a lot about DFT and microkinetic modeling, as well as doing research itself. It was nice that you always made some time for helping me. I would also like to thank him for the nice conversations, which were not related to this project, and for the trips we have made and will be making in the future.

I would also like to thank Emiel Hensen, for welcoming me in his research group and for giving me this interesting research topic. I would like to thank him for letting me participate in the NCCC conference for two years, in the summer school at Rolduc abbey, and in the winter school at Han-sur-Lesse. These gatherings were a welcome addition to my scientific knowledge about catalysis, environmental issues and theoretical physics. I would like to thank him, Rutger van Santen and Xander Nijhuis for being part of the advising committee of my graduation project.

I would also like to thank Bart Zijlstra, who was always ready to discuss about the results and read through my work, as it was in progress.

Next, I would like to thank my friends for listening to conversations about my research and giving other topics to talk and to think about. It was very helpful to get my mind of the problems every once in a while.

A final and special thanks to my my brother, for some fruitful discussions and for giving me tips and tricks regarding my English grammar, and to my parents, for replenishing my motivation and energy in the weekends. Your support helped me a great deal in accomplishing this thesis and getting me where I am in the first place.

Bibliography

- [1] Bruce, C. G. and Helmut, K. *Advances in catalysis*. Academic Press, (2011). Chapter 3: Mechanistic Issues in Fischer-Tropsch Catalysis by R.A. van Santen and I.M. Ciobîcă and E. van Steen and M.M. Ghouri.
- [2] Schulz, H. *Applied Catalysis A: General* **186**(1-2), 3–12 (1999).
- [3] Dry, M. E. *Catalysis Today* **71**(3-4), 227–241 (2002).
- [4] van Santen, R. A., Ghouri, M. M., Shetty, S., and Hensen, E. J. M. *Catalysis, Science and Technology* **1**(6), 891–911 (2011).
- [5] van Santen, R. A., Markvoort, A. J., Ghouri, M. M., Hilbers, P. A. J., and Hensen, E. J. M. *J. Phys. Chem. C* **117**(9), 4488–4504 (2013).
- [6] van Santen, R. A. and Markvoort, A. J. *ChemCatChem* **5**(11), 3387–3397 (2013).
- [7] Loveless, B. T., C.Buda, Neurock, M., and Iglesia, E. *J. Am. Chem. Soc* **135**(16) (2013).
- [8] Bezemer, G. L., Bitter, J. H., Kuipers, H. P. C. E., Oosterbeek, H., Holewijn, J. E., Xu, X., Kapteijn, F., van Dillen, A. J., and de Jong, K. P. *J. Am. Chem. Soc* **128**(12), 3956–3964 (2006).
- [9] den Breejen, J. P., Radstake, P. B., Bezemer, G. L., Bitter, J. H., Frøseth, V., Holmen, A., and de Jong, K. P. *J. Am. Chem. Soc* **131**(12), 7197–7203 (2009).
- [10] Biloen, P. and Sachtler, W. M. H. *Adv Catal* **30**(1), 165–216 (1981).
- [11] Pichler, H., Schulz, H., and Hojabri, F. *Brennstoff-Chemie; Zeitschrift für Chemie und chemische Technologie der Brennstoffe und ihrer Nebenprodukte* **45**, 215 (1964).
- [12] van Rijn, J. (2013).
- [13] Born, R. and Oppenheimer, R. *Annalen der Physik* **389**(20) (1927).
- [14] Hohenberg, P. and Kohn, W. *Physical Review* **136** (1964).
- [15] Kohn, W. and Sham, L. J. *Physical Review* **140** (1965).
- [16] Eisenschitz, R. and London, F. *Zeitschrift für Physik* **60**, 491–257 (1930).
- [17] Blöchl, P. E. *Phys. Rev. B* **50**(24), 17953–17979 (1994).
- [18] Shustorovich, E. M. *J. Am. Chem. Soc.* **106**, 6479–6481 (1984).
- [19] van Santen, R. A. *Recl. Trav. Chim. Pays-Bas* **109**, 59–63 (1990).
- [20] Henkelman, G. and Jónsson, H. *J. Chem. Phys.* **113**(22) (2000).

- [21] http://www.theochem.uni-stuttgart.de/~kaestner/images_large/nudged_elastic_band_big.jpg.
- [22] Breitkopf., C. Lectures at Fritz-Haber-Institut, (2004).
- [23] <http://www.mkmcxx.nl>.
- [24] Eyring, H. *J. Chem. Phys* **3**(2), 107–115 (1935).
- [25] Brønsted, J. N. *Chem. Rev.* **5**(3), 231–338 (1928).
- [26] Evans, M. G. and Polanyi, M. *Trans. Faraday. Soc.* **34**, 11–24 (1938).
- [27] Stegelmann, C. and Campbell, A. A. T. *J. Am. Chem. Soc.* **311**(23), 8077–8082 (2009).
- [28] Methfessel, M. and Paxton, A. T. *Phys. Rev. B.* **40**, 3616–3621 (1989).
- [29] Zhu, T., van Grootel, P. W., Filot, I. A. W., Sun, S., van Santen, R. A., and Hensen, E. J. M. *Journal of Catalysis* **279**, 227–235 (2013).
- [30] van Santen, R. A. *J. Am. Chem. Soc.* **131**, 12874–12875 (2009).
- [31] Andersson, M. P., Abild-Pedersen, F., Remediakis, I. N., Bligaard, T., Jones, G., Engbæk, J., Lytken, O., Horch, S., Nielsen, J. H., Sehested, J., Rostrup-Nielsen, J. R., Nørskov, J. K., and Chorkendorff, I. *Journal of Catalysis* **255**, 6 – 19 (2008).
- [32] and I.M. Ciobîcă and van Santen, R. A. *J. Am. Chem. Soc.* **131**, 12874–12875 (2009).
- [33] v Grootel, P. *Thesis Theoretical Study on the Structure Dependence of the Steam Methane Reforming Reaction by Rhodium*. PhD thesis, (2012).
- [34] Kapur, N., Hyun, J., Shan, B., Nicholas, J. B., and Cho, K. *J. Phys. Chem. C.* **114**, 10171–10182 (2010).
- [35] Bernal, S., Calvino, J. J., Cifredo, G. A., Rodriguez-Izquierdo, J. M., Perrichon, V., and Laachir, A. *J. Chem. Soc., Chem. Commun.* , 460–462 (1992).
- [36] Bhasin, M., Bartley, W., Ellgen, P., and Wilson, T. *Journal of Catalysis* **54**(2), 120 – 128 (1978).
- [37] Kip, B., Hermans, E., Wolput, J. V., Hermans, N., Grondelle, J. V., and Prins, R. *Applied Catalysis* **35**(1), 109 – 139 (1987).
- [38] Turner, M., Byers, P., and Maitlis, P. *Catalysis Letters* **26**(1-2), 55–60 (1994).
- [39] Vannice, M. *Journal of Catalysis* **37**(3), 462 – 473 (1975).
- [40] US Secretary of commerce on behalf of the United States. <http://webbook.nist.gov/chemistry/>, (2011).

- [41] van Santen, R. A., Markvoort, A. J., Filot, I. A. W., and Hensen, E. J. M. *Phys. Chem. Chem. Phys.* **15**, 17038–17063 (2013).
- [42] Chen, J. and Liu, Z. *J. Am. Chem. Soc.* **130**, 7929–7937 (2008).
- [43] Jiang, R., Guo, W., Li, M., Zhu, H., Zhao, L., Lu, X., and Shan, H. *Journal of Molecular Catalysis A: Chemical* **344**, 99–110 (2011).
- [44] van Heugten, G. (2013).
- [45] Cheng, J., Hu, P., Ellis, P., French, S., Kelly, G., and Lok, C. M. *J. Phys. Chem. C.* **112**, 6082–6086 (2008).
- [46] Zhang, J., Cao, X. M., Hu, P., Zhong, Z., Borgna, A., and Wu, P. *J. Phys. Chem. C.* **115**, 22429–22437 (2011).

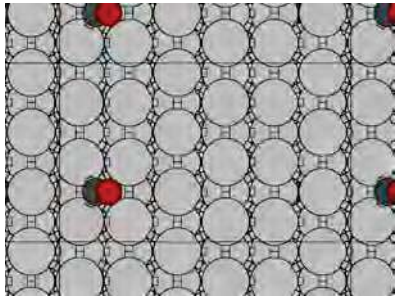
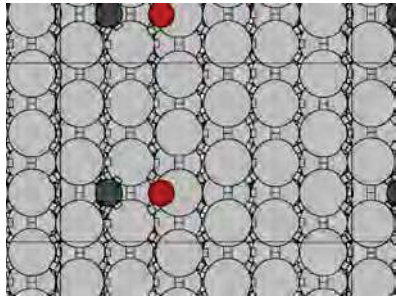
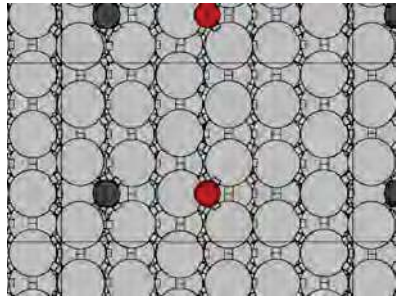
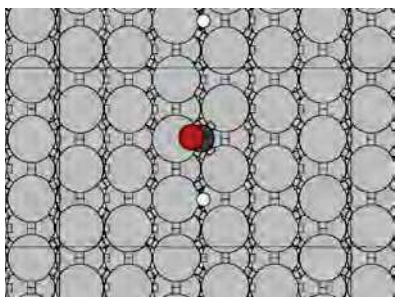
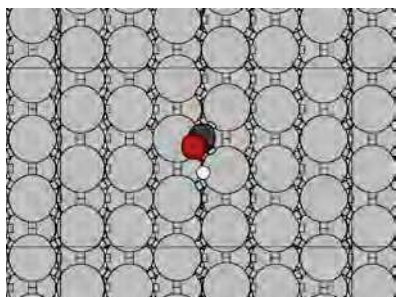
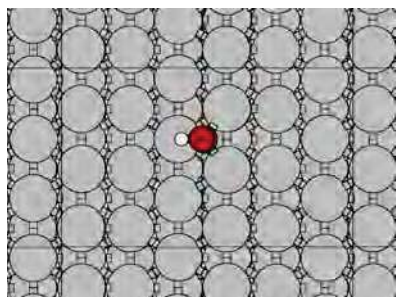
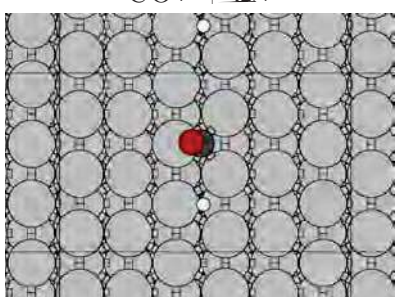
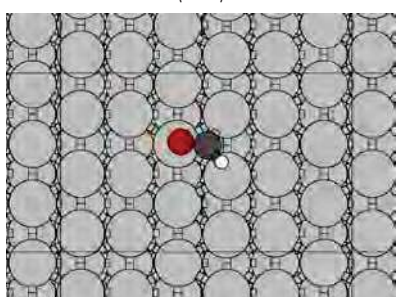
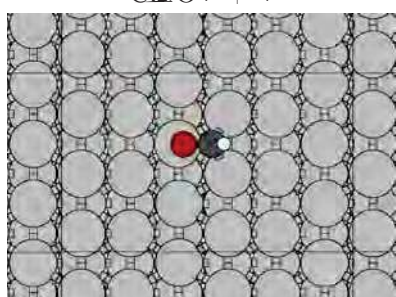
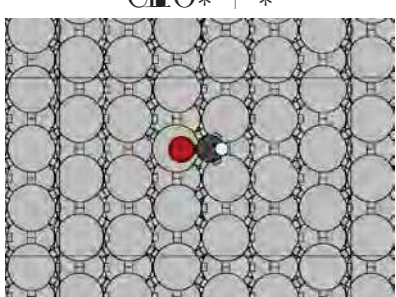
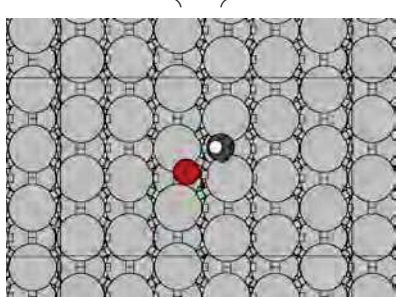
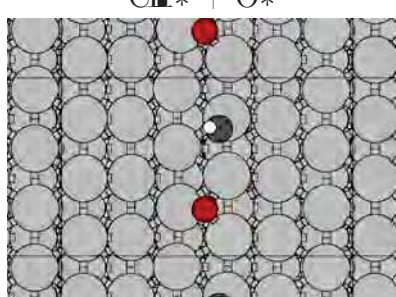
8 Appendix

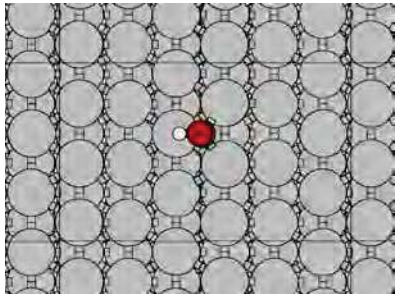
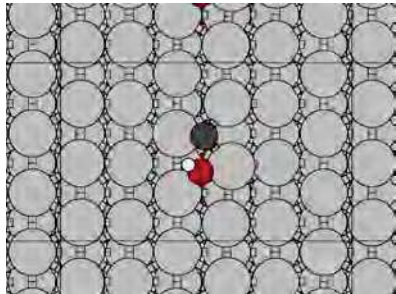
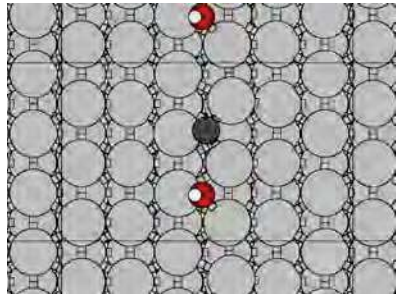
8.1 CO dissociation reactions

Table 12: Elementary reaction steps as calculated for the direct and hydrogen assisted CO dissociation reactions.

| # | Elementary Reaction Steps | ν_f [s ⁻¹] | E_f [J/mol] | ν_b [s ⁻¹] | E_b [J/mol] |
|---|--|----------------------------|---------------|----------------------------|---------------|
| 1 | CO* + * \longleftrightarrow C* + O* | 5.00e+12 | 1.50e+05 | 6.30e+12 | 8.31e+04 |
| 2 | CO* + H* \longleftrightarrow COH* + * | 5.39e+12 | 1.75e+05 | 1.50e+13 | 6.84e+04 |
| 3 | CO* + H* \longleftrightarrow CH*O* + * | 2.21e+12 | 1.34e+05 | 1.14e+13 | 1.76e+04 |
| 4 | CH*O* + * \longleftrightarrow CH* + O* | 2.26e+11 | 1.40e+05 | 2.49e+07 | 1.85e+05 |
| 5 | COH* + * \longleftrightarrow C* + OH* | 1.29e+11 | 1.70e+05 | 3.12e+10 | 2.04e+05 |

Table 13: Elementary reaction steps as calculated for the direct and hydrogen assisted CO dissociation.

| Initial state | Transition state | Final state |
|---|---|---|
| $\text{CO}^* + *$  | \longleftrightarrow  | $\text{C}^* + \text{O}^*$  |
| $\text{CO}^* + \text{H}^*$  | \longleftrightarrow  | $\text{COH}^* + *$  |
| $\text{CO}^* + \text{H}^*$  | \longleftrightarrow  | $\text{CHO}^* + *$  |
| $\text{CHO}^* + *$  | \longleftrightarrow  | $\text{CH}^* + \text{O}^*$  |

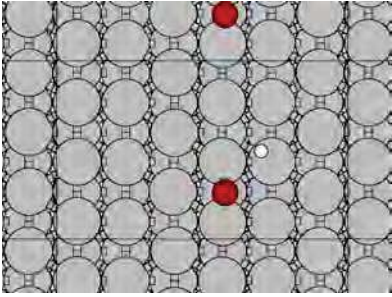
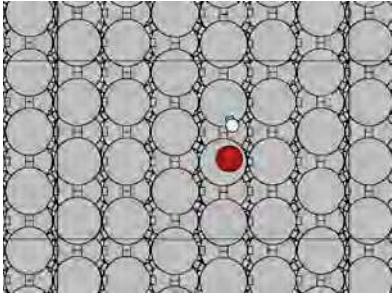
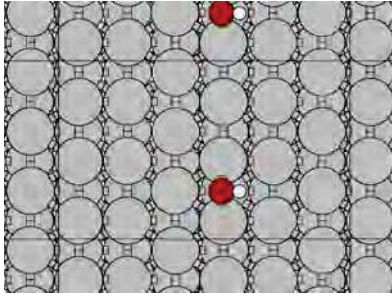
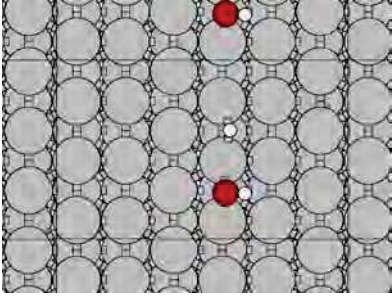
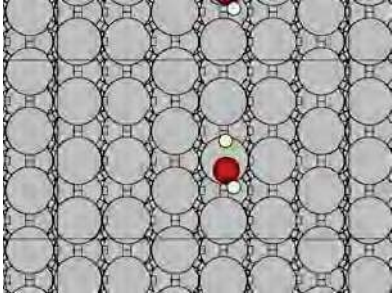
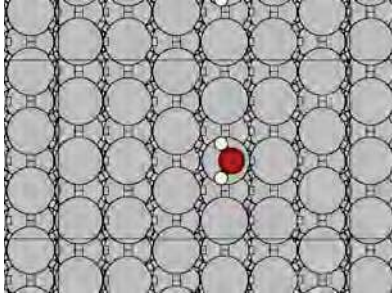
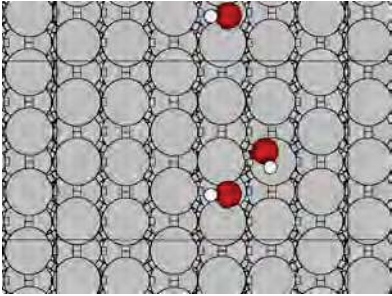
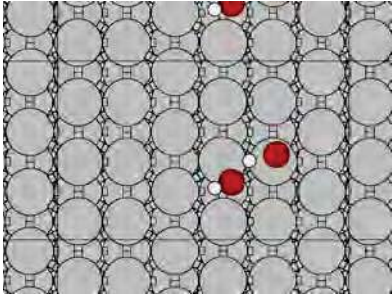
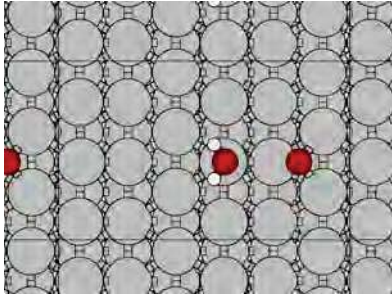
| Initial state | Transition state | Final state |
|---|--|---|
| <p style="text-align: center;">$\text{CO}^{\ddagger*} + *$</p>  | <p style="text-align: center;">\longleftrightarrow</p>  | <p style="text-align: center;">$\text{C}^* + \text{O}^{\ddagger*}$</p>  |

8.2 water formation

Table 14: Elementary reaction steps as calculated for the formation of water.

| # | Elementary Reaction Steps | ν_f [s ⁻¹] | E_f [J/mol] | ν_b [s ⁻¹] | E_b [J/mol] |
|---|--|----------------------------|---------------|----------------------------|---------------|
| 6 | $O^* + H^* \rightleftharpoons OH^* + *$ | 1.80e+15 | 1.13e+05 | 4.50e+13 | 1.07e+05 |
| 7 | $OH^* + H^* \rightleftharpoons H_2O^* + *$ | 2.90e+13 | 5.40e+04 | 6.20e+11 | 6.00e+04 |
| 8 | $2 OH^* \rightleftharpoons H_2O + O^*$ | 3.90e+12 | 7.70e+04 | 6.20e+11 | 6.10e+04 |

Table 15: Elementary reaction steps as calculated for the formation of water.

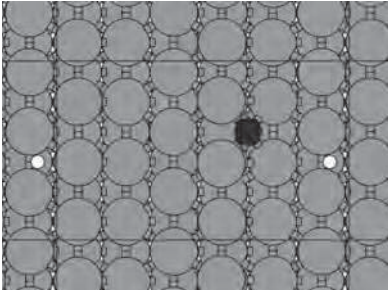
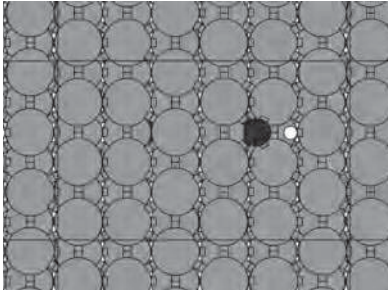
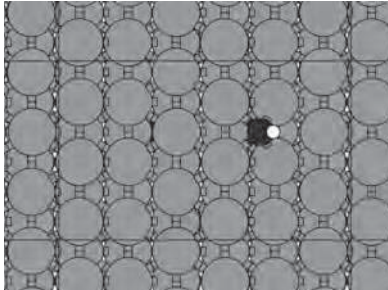
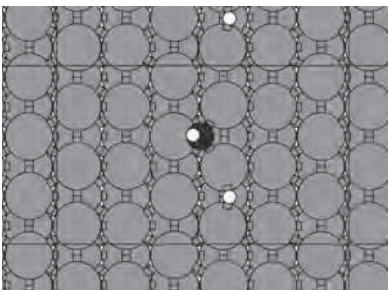
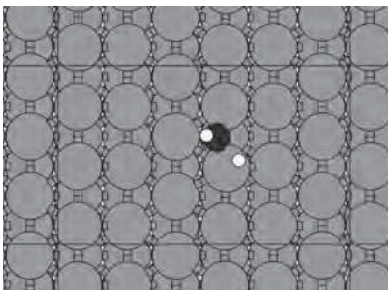
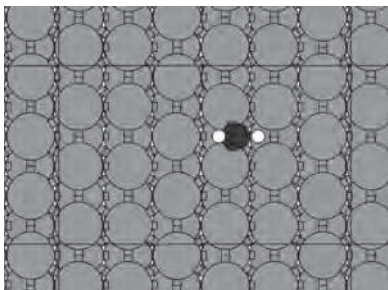
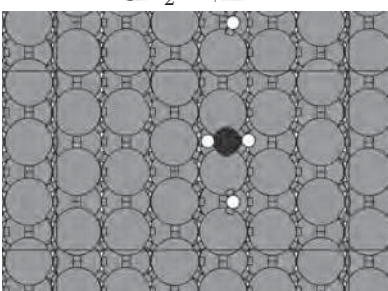
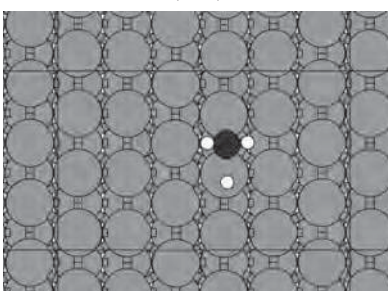
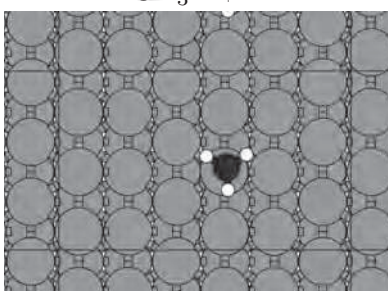
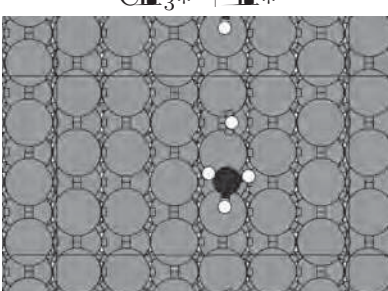
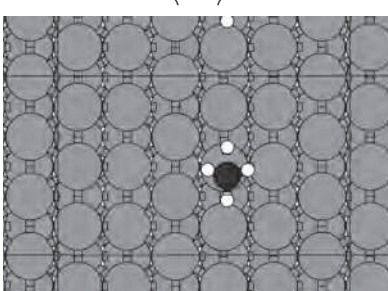
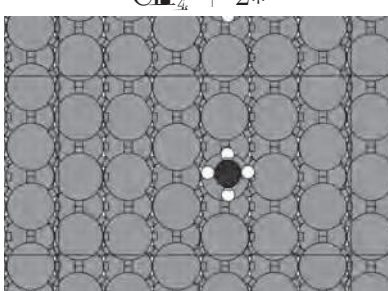
| Initial state | Transition state | Final state |
|---|---|---|
| $O^* + H^*$  | \longleftrightarrow  | $OH^* + *$  |
| $OH^* + H^*$  | \longleftrightarrow  | $H_2O^* + *$  |
| $2 OH^*$  | \longleftrightarrow  | $H_2O + O^*$  |

8.3 Elementary Reaction Steps with kinetic parameters for the Methanation reaction

Table 16: Elementary reaction steps as calculated for the methanation reaction.

| # | Elementary Reaction Steps | ν_f [s ⁻¹] | E_f [J/mol] | ν_b [s ⁻¹] | E_b [J/mol] |
|----|--|----------------------------|---------------|----------------------------|---------------|
| 9 | $C^* + H_2^* \rightleftharpoons CH_2^* + *$ | 3.18e+13 | 7.96e+04 | 2.82e+13 | 7.40e+04 |
| 10 | $CH_2^* + H_2^* \rightleftharpoons CH_4^* + *$ | 2.88e+12 | 1.19e+05 | 1.77e+11 | 5.39e+04 |
| 11 | $CH_2^* + H_2^* \rightleftharpoons CH_3^* + *$ | 5.85e+12 | 1.55e+04 | 1.25e+11 | 5.64e+04 |
| 12 | $CH_3^* + H_2^* \rightleftharpoons CH_4^* + 2 *$ | 1.92e+14 | 7.63e+04 | 2.43e+10 | 3.29e+04 |

Table 17: Elementary reaction steps as calculated for the methanation reaction.

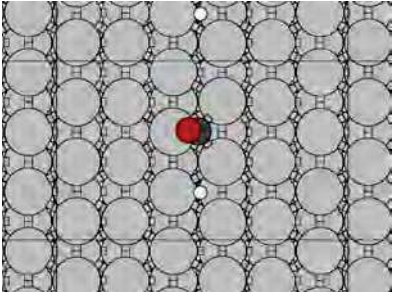
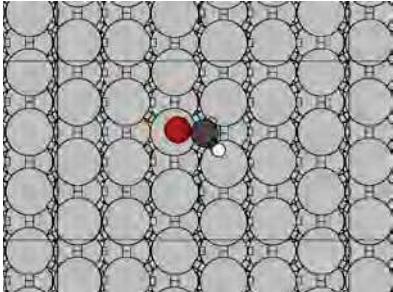
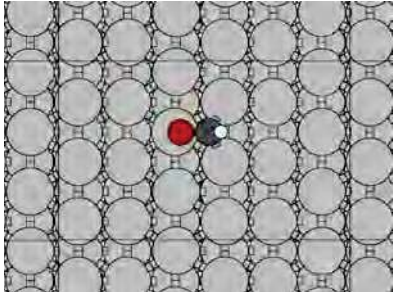
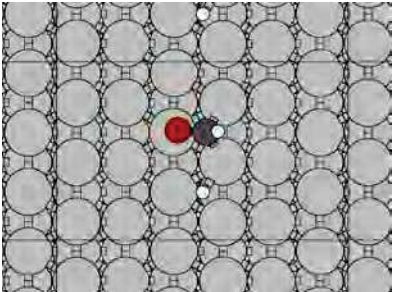
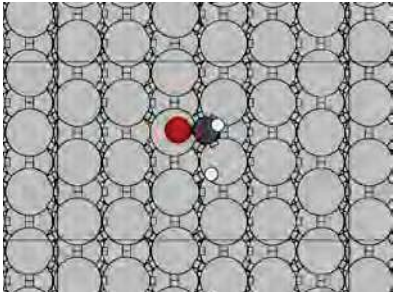
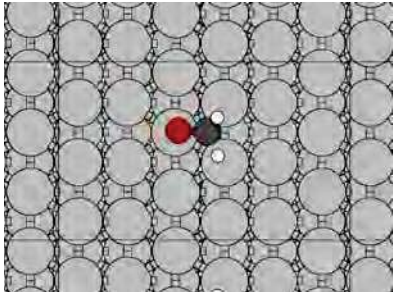
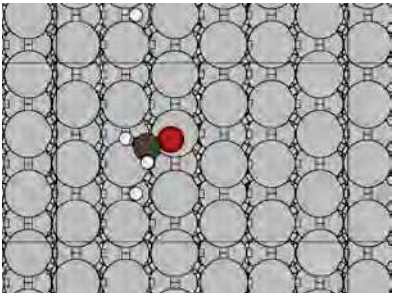
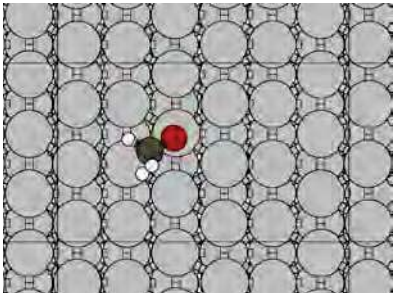
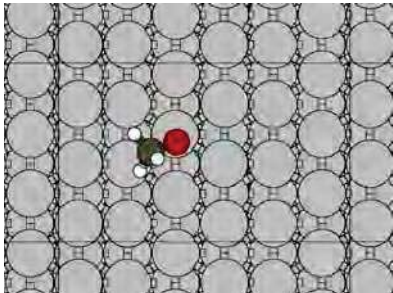
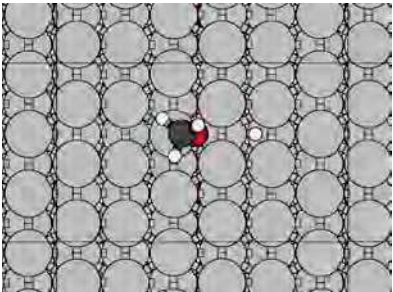
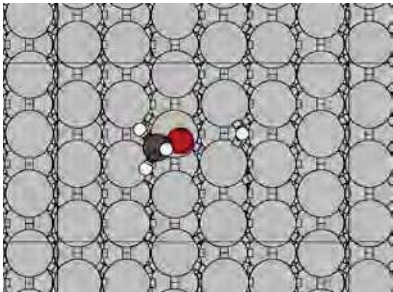
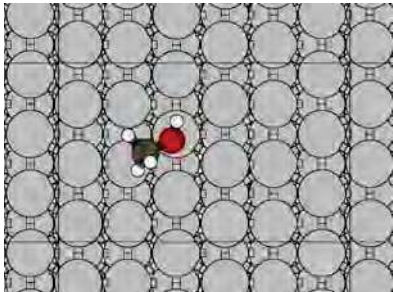
| Initial state | Transition state | Final state |
|---|---|---|
| $C^* + H_2^*$  | \longleftrightarrow  | $CH^* + *$  |
| $CH^* + H_2^*$  | \longleftrightarrow  | $CH_2^* + *$  |
| $CH_2^* + H_2^*$  | \longleftrightarrow  | $CH_3^* + *$  |
| $CH_3^* + H_2^*$  | \longleftrightarrow  | $CH_4 + 2*$  |

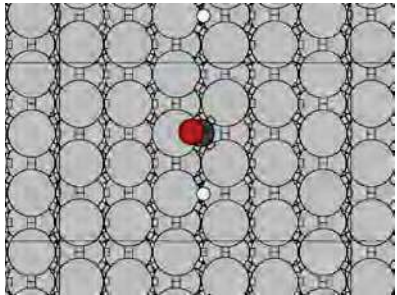
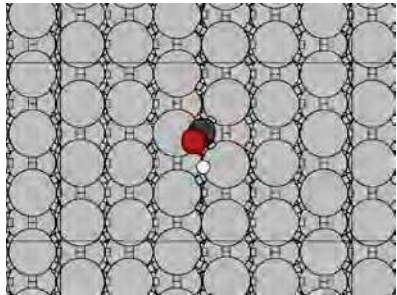
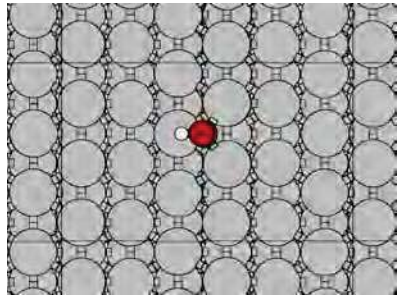
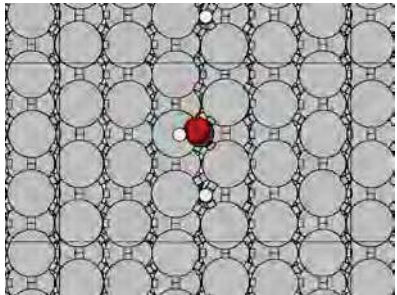
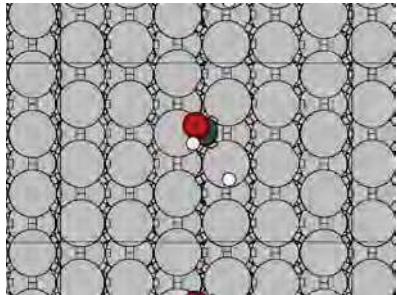
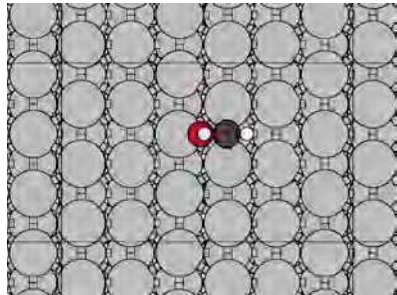
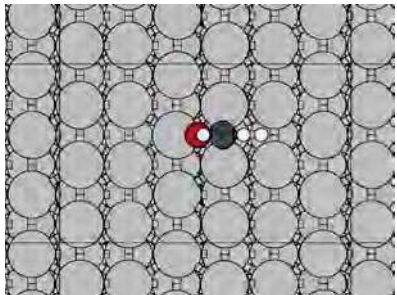
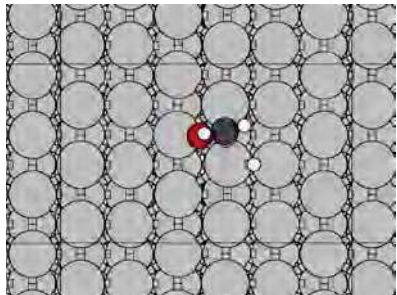
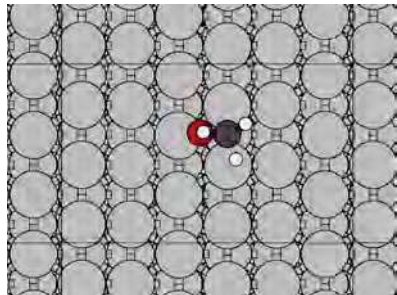
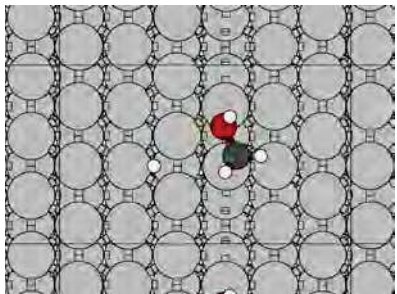
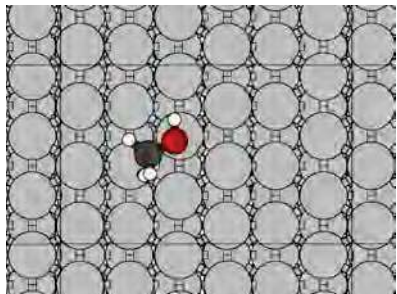
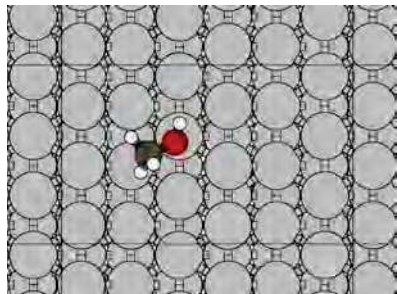
8.4 Elementary reaction steps as calculated for the reaction towards methanol

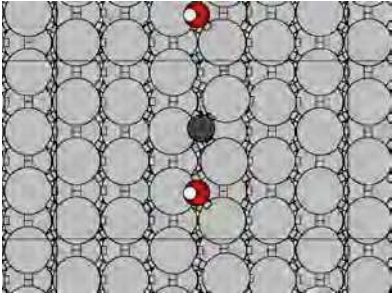
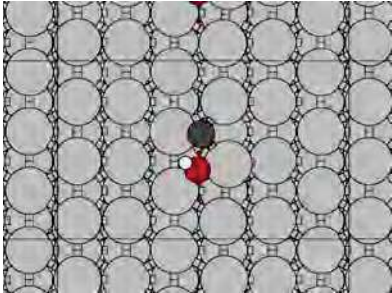
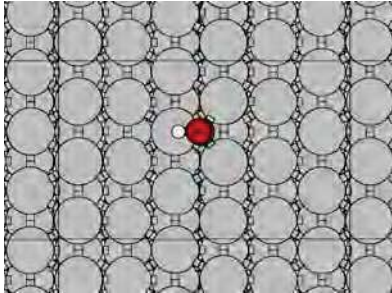
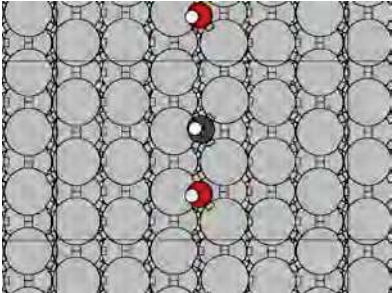
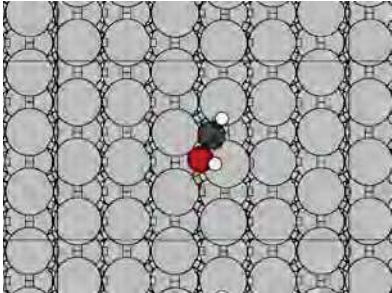
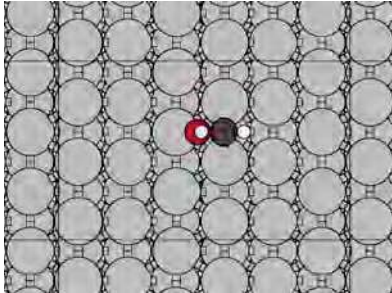
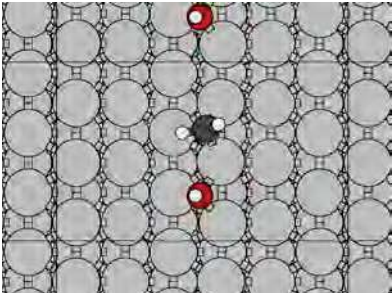
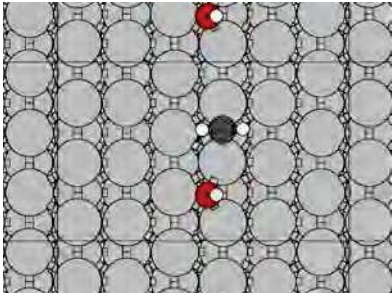
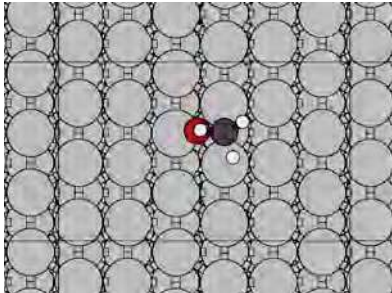
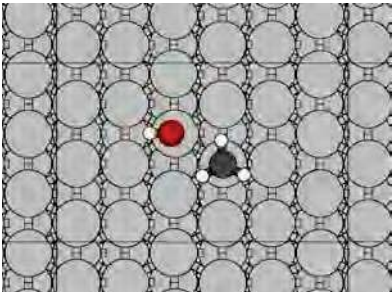
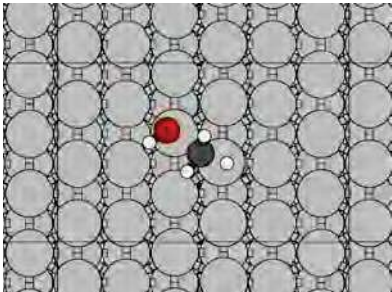
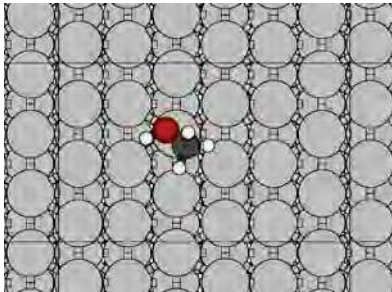
Table 18: Elementary reaction steps as calculated for the methanol synthesis.

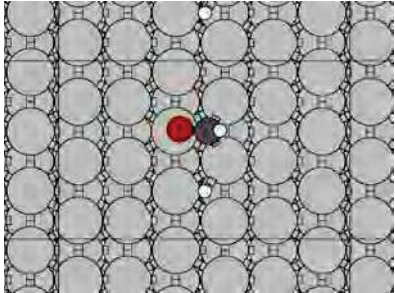
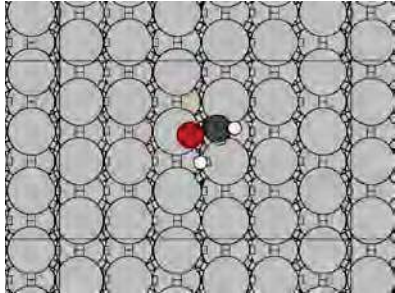
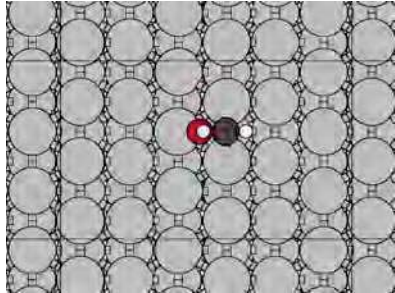
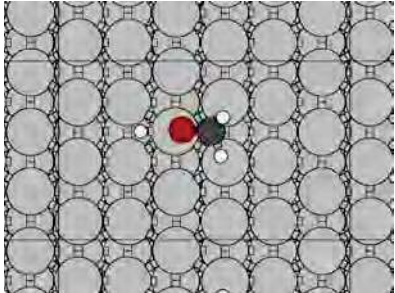
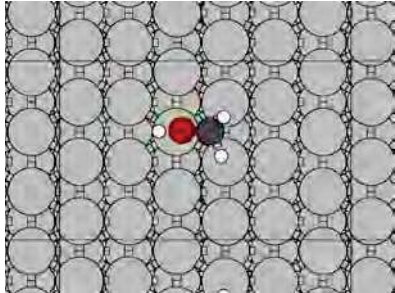
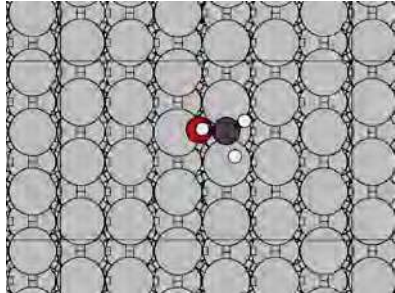
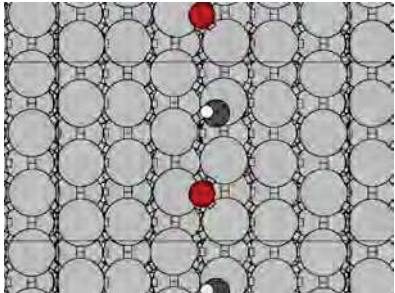
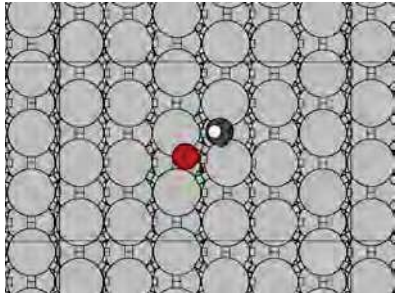
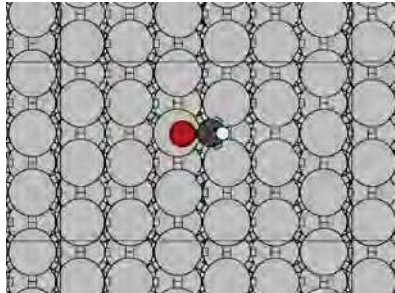
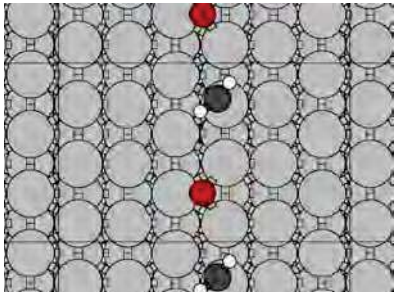
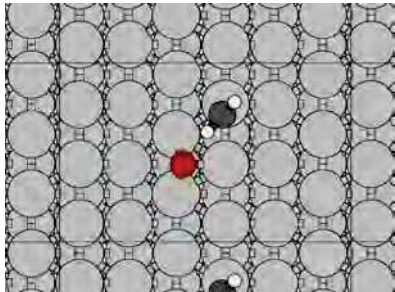
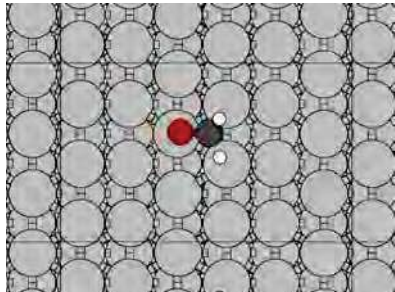
| # | Elementary Reaction Steps | ν_f [s ⁻¹] | E_f [J/mol] | ν_b [s ⁻¹] | E_b [J/mol] |
|----|--|----------------------------|---------------|----------------------------|---------------|
| 3 | CO* + H* \longleftrightarrow CH ₂ O* + * | 2.21e+12 | 1.34e+05 | 1.14e+13 | 1.76e+04 |
| 13 | CH ₂ O* + H* \longleftrightarrow CH ₃ O* + * | 1.32e+13 | 7.52e+04 | 1.26e+13 | 3.90e+03 |
| 14 | CH ₂ O* + H* \longleftrightarrow CH ₃ O* + * | 1.91e+11 | 1.62e+05 | 8.19e+13 | 7.19e+04 |
| 15 | CH ₃ O* + H* \longleftrightarrow CH ₃ OH* + * | 1.76e+11 | 2.82e+04 | 1.03e+14 | 7.36e+03 |
| 2 | CO* + H* \longleftrightarrow COH* + * | 5.39e+12 | 1.75e+05 | 1.50e+13 | 6.84e+04 |
| 16 | COH* + H* \longleftrightarrow CH ₂ OH* + * | 3.22e+12 | 9.06e+04 | 2.79e+10 | 1.49e+04 |
| 17 | CH ₂ OH* + H* \longleftrightarrow CH ₃ OH* + * | 1.67e+11 | 6.89e+04 | 3.98e+13 | 4.26e+03 |
| 18 | CH ₂ OH* + H* \longleftrightarrow CH ₃ OH* + * | 2.76e+11 | 2.00e+05 | 6.00e+10 | 1.48e+05 |
| 19 | C* + OH* \longleftrightarrow COH* + * | 3.12e+10 | 2.04e+05 | 1.29e+11 | 1.70e+05 |
| 20 | CH* + OH* \longleftrightarrow CH ₂ OH* + * | 2.73e+12 | 2.07e+05 | 2.77e+11 | 1.03e+05 |
| 21 | CH ₂ * + OH* \longleftrightarrow CH ₃ OH* + * | 7.39e+12 | 1.41e+05 | 2.03e+13 | 3.77e+04 |
| 22 | CH ₃ * + OH* \longleftrightarrow CH ₃ OH* + * | 3.11e+13 | 2.09e+05 | 5.06e+15 | 9.50e+04 |
| 23 | CH ₂ O* + H* \longleftrightarrow CH ₃ OH* + * | 2.18e+12 | 1.75e+05 | 6.41e+10 | 1.09e+05 |
| 24 | CH ₂ O* + H* \longleftrightarrow CH ₃ OH* + * | 7.48e+09 | 1.29e+05 | 9.42e+11 | 6.94e+04 |
| 25 | CH ₂ * + O* \longleftrightarrow CH ₂ O* + * | 2.49e+07 | 1.85e+05 | 2.26e+11 | 1.40e+05 |
| 26 | CH ₂ * + O* \longleftrightarrow CH ₂ O* + * | 7.86e+12 | 1.13e+05 | 5.01e+12 | 6.34e+04 |
| 27 | CH ₃ * + O* \longleftrightarrow CH ₃ O* + * | 1.28e+15 | 2.11e+05 | 2.04e+13 | 1.12e+05 |

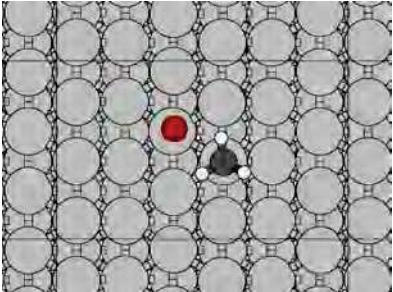
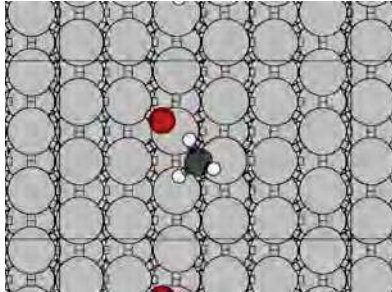
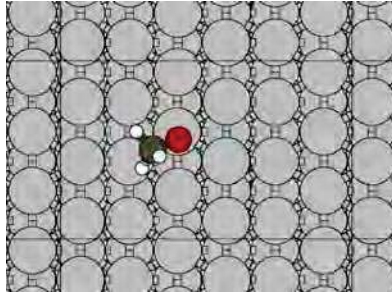
Table 19: Elementary reaction steps as calculated for the methanol synthesis.

| Initial state | Transition state | Final state |
|---|---|---|
| $\text{CO}^* + \text{H}^*$  | \longleftrightarrow  | $\text{CHO}^* + *$  |
| $\text{CHO}^* + \text{H}^*$  | \longleftrightarrow  | $\text{CH}_2\text{O}^* + *$  |
| $\text{CH}_2\text{O}^* + \text{H}^*$  | \longleftrightarrow  | $\text{CH}_3\text{O}^* + *$  |
| $\text{CH}_3\text{O}^* + \text{H}^*$  | \longleftrightarrow  | $\text{CH}_3\text{OH}^* + *$  |

| Initial state | Transition state | Final state |
|--|---|---|
| $\text{CO}^* + \text{H}^*$  | \longleftrightarrow  | $\text{COH}^* + *$  |
| $\text{COH}^* + \text{H}^*$  | \longleftrightarrow  | $\text{CHOH}^* + *$  |
| $\text{CHOH}^* + \text{H}^*$  | \longleftrightarrow  | $\text{CH}_2\text{OH}^* + *$  |
| $\text{CH}_2\text{OH}^* + \text{H}^*$  | \longleftrightarrow  | $\text{CH}_3\text{OH}^* + *$  |

| Initial state | Transition state | Final state |
|--|---|---|
| $C^* + OH^*$  | \longleftrightarrow  | $COH^* + *$  |
| $CH^* + OH^*$  | \longleftrightarrow  | $CH_2OH^* + *$  |
| $CH_2^* + OH^*$  | \longleftrightarrow  | $CH_2OH^* + *$  |
| $CH_3^* + OH^*$  | \longleftrightarrow  | $CH_3OH^* + *$  |

| Initial state | Transition state | Final state |
|---|---|--|
| $\text{CH}_2\text{O}^* + \text{H}^*$  | \longleftrightarrow  | $\text{CH}_2\text{OH}^* + *$  |
| $\text{CH}_2\text{O}^* + \text{H}^*$  | \longleftrightarrow  | $\text{CH}_2\text{OH}^* + *$  |
| $\text{CH}_2^* + \text{O}^*$  | \longleftrightarrow  | $\text{CHO}^* + *$  |
| $\text{CH}_2^* + \text{O}^*$  | \longleftrightarrow  | $\text{CH}_2\text{O}^* + *$  |

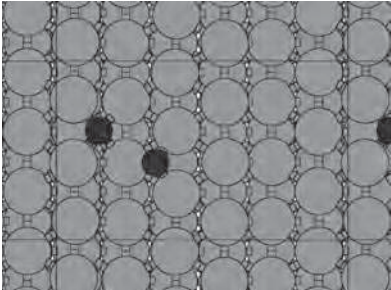
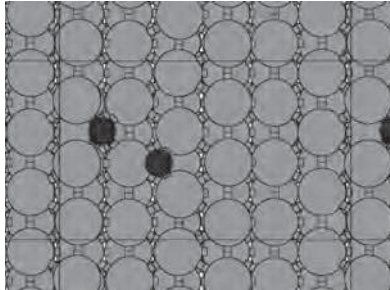
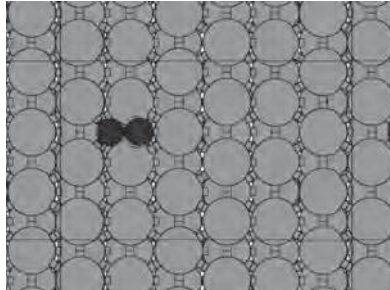
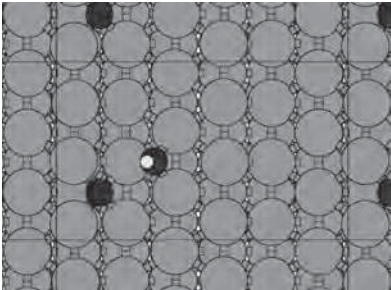
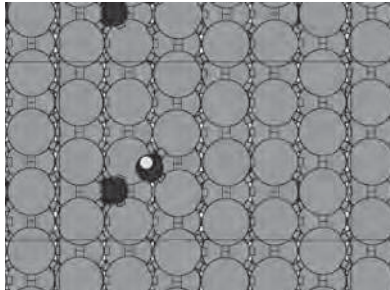
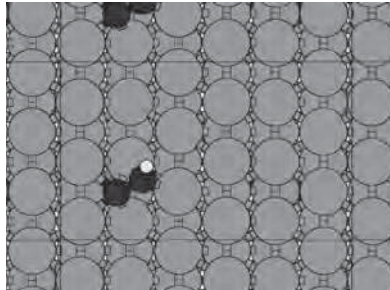
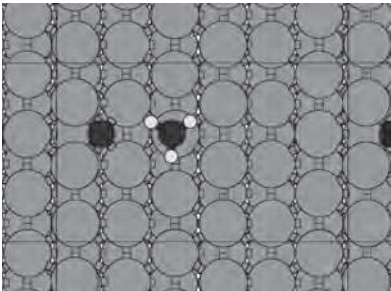
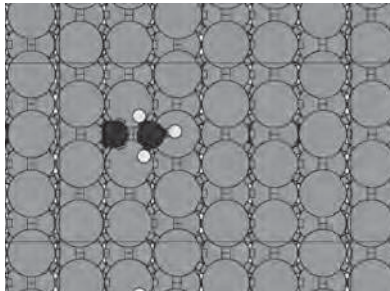
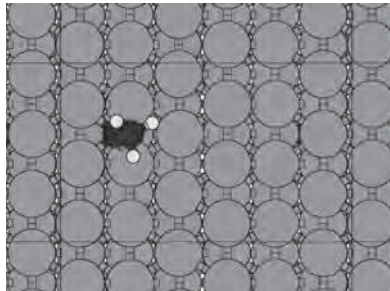
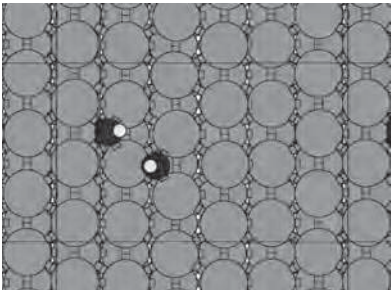
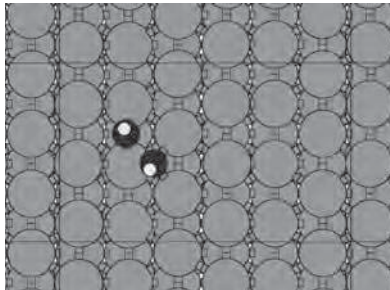
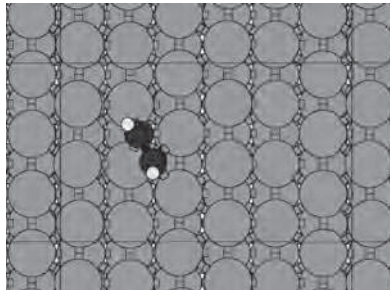
| Initial state | Transition state | Final state |
|---|---|--|
| $\text{CH}_3^* + \text{O}^*$  | \longleftrightarrow  | $\text{CH}_3\text{O}^* + *$  |

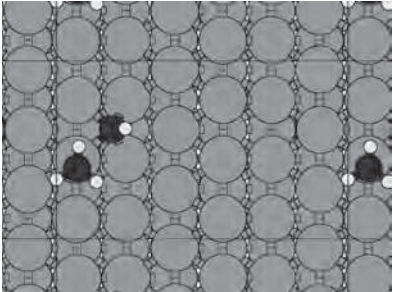
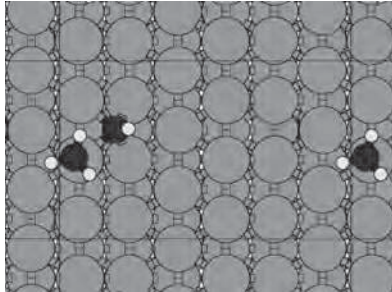
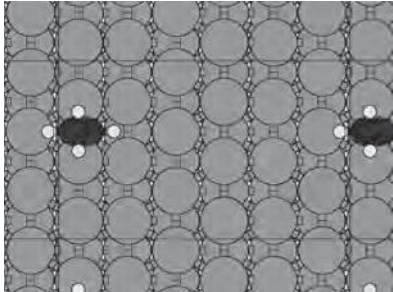
8.5 Elementary reaction steps as calculated for the C-C coupling reactions

Table 20: Elementary reaction steps as calculated for the C-C coupling reactions.

| # | Elementary Reaction Steps | | | ν_f [s ⁻¹] | E_f [J/mol] | ν_b [s ⁻¹] | E_b [J/mol] |
|----|---------------------------|-----------------------|-------------------------|----------------------------|---------------|----------------------------|---------------|
| 28 | C* + C* | \longleftrightarrow | CC* + * | 7.56e+12 | 8.64e+04 | 2.55e+12 | 9.14e+04 |
| 29 | C* + CH* | \longleftrightarrow | CHC* + * | 1.44e+13 | 1.03e+05 | 4.26e+12 | 9.33e+04 |
| 30 | C* + CH ₃ * | \longleftrightarrow | CH ₃ C* + * | 9.42e+12 | 1.19e+05 | 1.14e+13 | 1.44e+05 |
| 31 | CH* + CH* | \longleftrightarrow | CHCH* + * | 4.33e+13 | 1.56e+05 | 5.60e+12 | 9.39e+04 |
| 32 | CH* + CH ₃ * | \longleftrightarrow | CHCH ₃ * + * | 1.10e+14 | 3.80e+04 | 2.26e+13 | 1.95e+04 |

Table 21: Elementary reaction steps as calculated for the C-C coupling reactions.

| Initial state | Transition state | Final state |
|---|---|---|
| $C^* + C^*$  | \longleftrightarrow  | $CC^* + *$  |
| $C^* + CH^*$  | \longleftrightarrow  | $CHCH^* + *$  |
| $C^* + CH_3^*$  | \longleftrightarrow  | $CH_3CH^* + *$  |
| $CH^* + CH^*$  | \longleftrightarrow  | $CHCH^* + *$  |

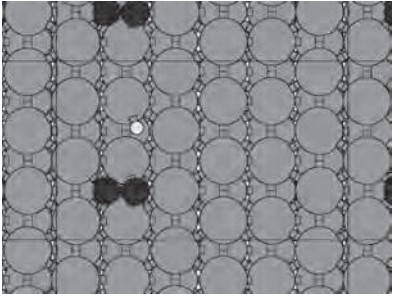
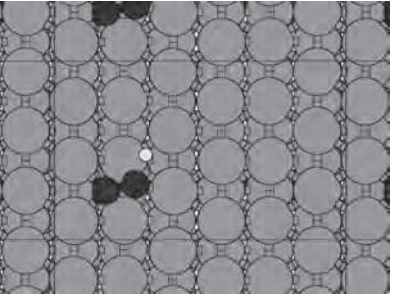
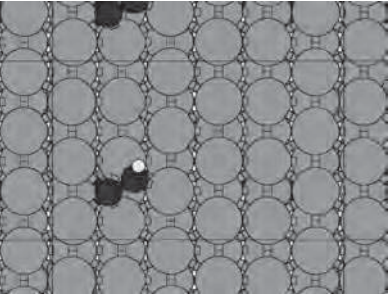
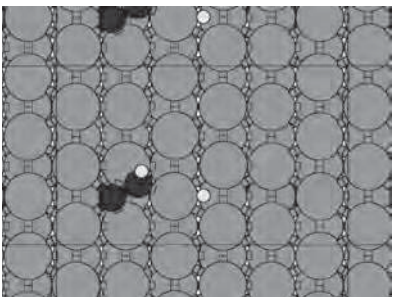
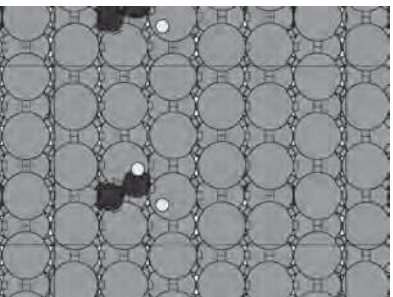
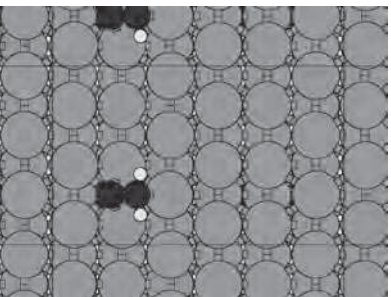
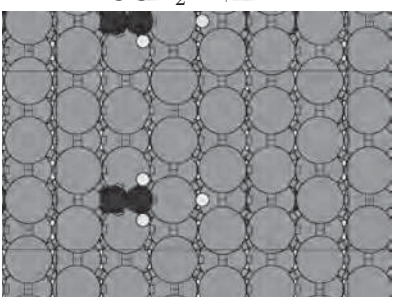
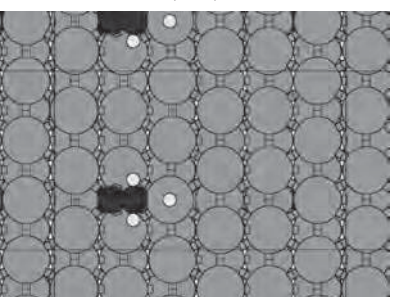
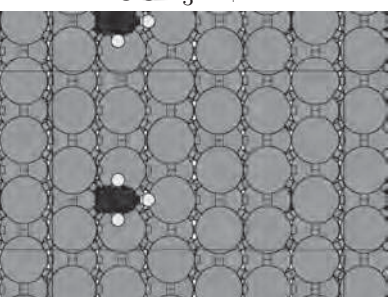
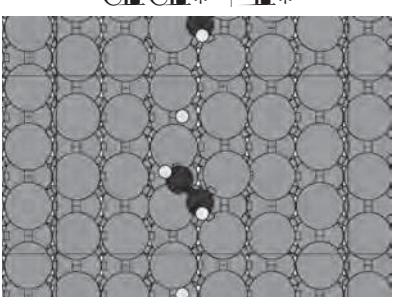
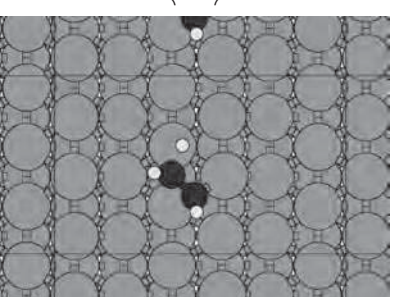
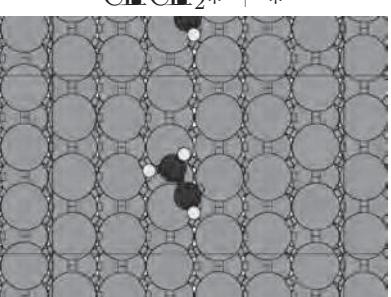
| Initial state | Transition state | Final state |
|--|---|---|
| $\text{CH}_2^* + \text{CH}_3^*$  | \longleftrightarrow  | $\text{CH}_2\text{CH}_3^* + *$  |

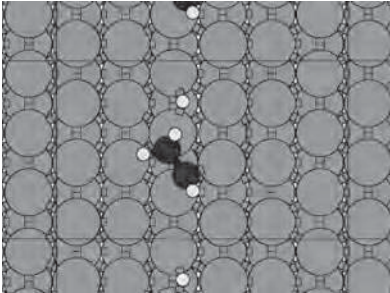
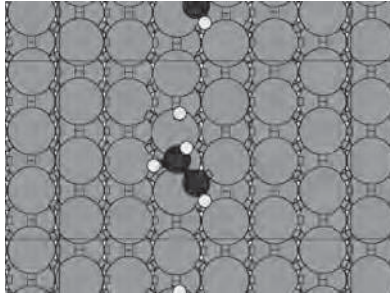
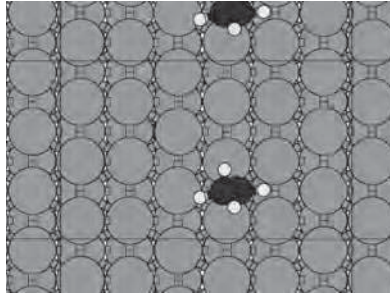
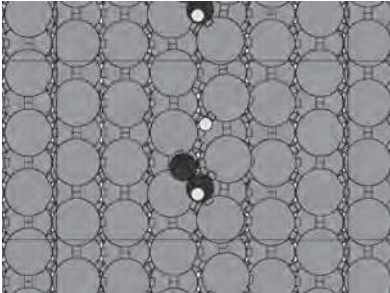
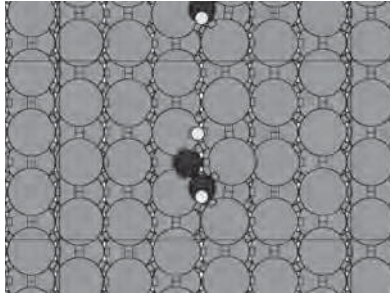
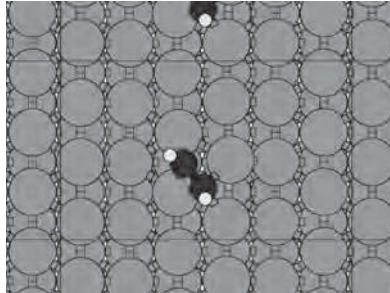
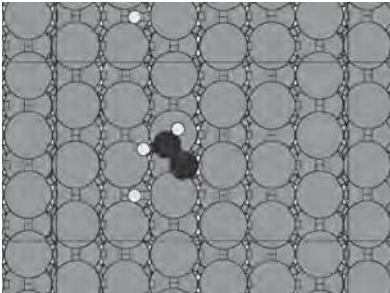
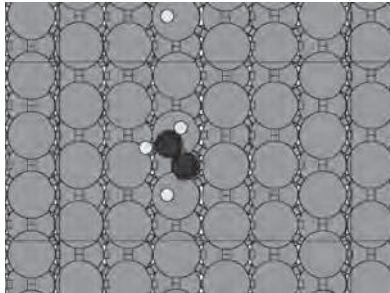
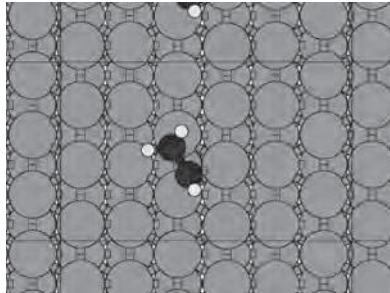
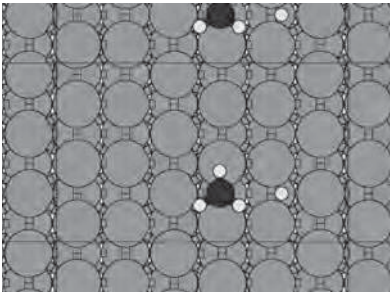
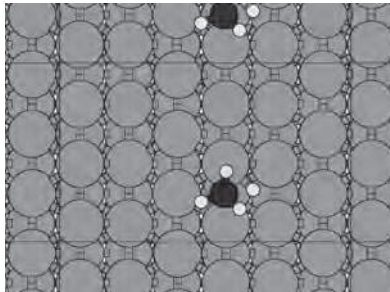
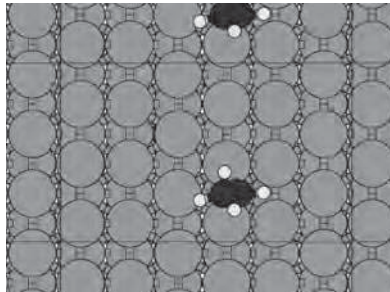
8.6 Elementary reaction steps as calculated for the hydrogenation towards C2-hydrocarbons

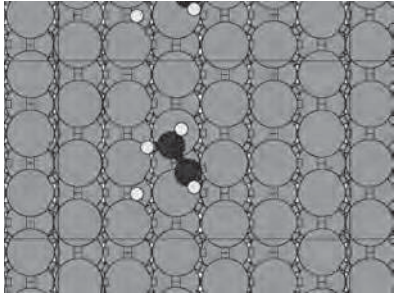
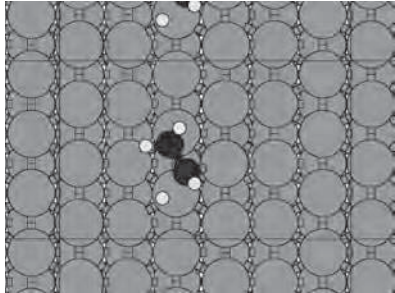
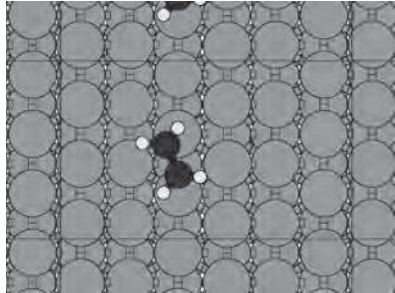
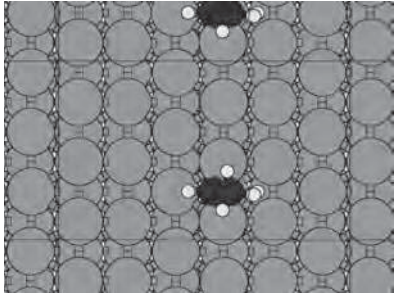
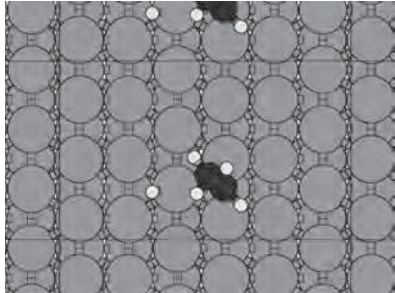
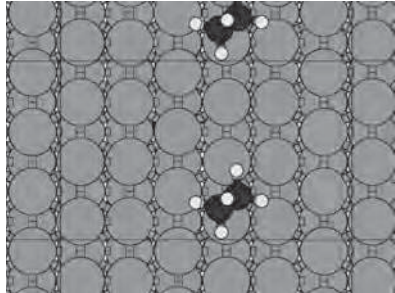
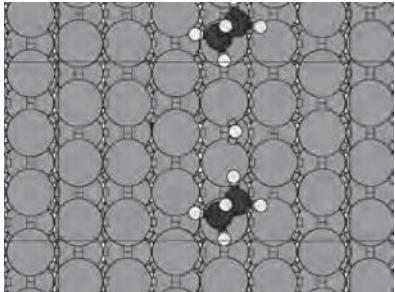
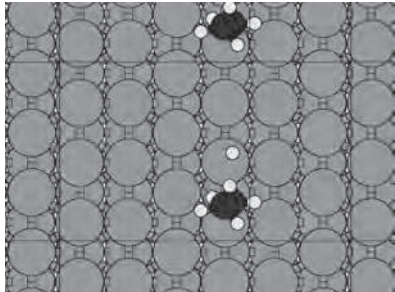
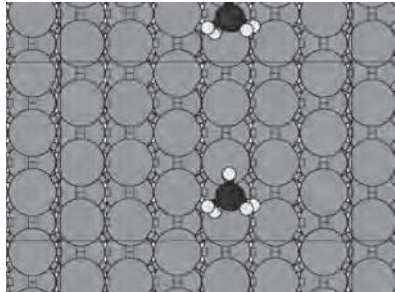
Table 22: Elementary reaction steps as calculated for synthesis towards C2-hydrocarbons.

| # | Elementary Reaction Steps | ν_f [s ⁻¹] | E_f [J/mol] | ν_b [s ⁻¹] | E_b [J/mol] |
|----|---|----------------------------|---------------|----------------------------|---------------|
| 34 | CC* + H* \longleftrightarrow CCH* + * | 4.73e+13 | 1.06e+05 | 6.27e+13 | 8.60e+04 |
| 35 | CCH* + H* \longleftrightarrow CCH ₂ * + * | 7.92e+12 | 7.46e+04 | 6.03e+12 | 4.35e+04 |
| 36 | CCH ₂ * + H* \longleftrightarrow CCH ₃ * + * | 2.64e+13 | 8.02e+04 | 3.07e+11 | 4.01e+04 |
| 37 | C ₂ H ₂ * + H* \longleftrightarrow C ₂ H ₃ * + * | 1.95e+13 | 1.01e+05 | 9.08e+12 | 3.51e+04 |
| 38 | C ₂ H ₃ * + H* \longleftrightarrow C ₂ H ₄ * + * | 6.15e+11 | 8.88e+04 | 1.13e+10 | 9.21e+04 |
| 39 | CCH* + H* \longleftrightarrow C ₂ H ₂ * + * | 5.06e+12 | 1.60e+05 | 3.39e+12 | 1.02e+05 |
| 40 | CCH ₂ * + H* \longleftrightarrow C ₂ H ₃ * + * | 8.24e+12 | 1.11e+05 | 6.33e+12 | 1.88e+04 |
| 41 | CCH ₃ * + H* \longleftrightarrow C ₂ H ₄ * + * | 3.67e+14 | 1.02e+05 | 5.37e+12 | 5.25e+04 |
| 42 | C ₂ H ₂ * + H* \longleftrightarrow C ₂ H ₃ * + * | 7.34e+12 | 6.60e+04 | 2.34e+13 | 3.52e+04 |
| 43 | C ₂ H ₃ * + H* \longleftrightarrow C ₂ H ₄ * + * | 5.81e+14 | 7.10e+04 | 2.77e+15 | 2.98e+04 |
| 44 | C ₂ H ₂ * + H* \longleftrightarrow C ₂ H ₃ * + 2* | 2.87e+12 | 9.10e+04 | 6.20e+12 | 3.40e+04 |

Table 23: Elementary reaction steps as calculated for the synthesis towards C2-hydrocarbons.

| Initial state | Transition state | Final state |
|---|---|---|
| $CC^* + H^*$  | \longleftrightarrow  | $CH_3^* + *$  |
| $CH_3^* + H^*$  | \longleftrightarrow  | $CH_4^* + *$  |
| $CH_3^* + H^*$  | \longleftrightarrow  | $CH_4^* + *$  |
| $CH_3CH_3^* + H^*$  | \longleftrightarrow  | $CH_3CH_2^* + *$  |

| Initial state | Transition state | Final state |
|--|---|---|
| $\text{ClHCl}_2^* + \text{H}^*$  | \longleftrightarrow  | $\text{ClHCl}_3^* + *$  |
| $\text{CCH}^* + \text{H}^*$  | \longleftrightarrow  | $\text{ClHCl}^* + *$  |
| $\text{CCH}_2^* + \text{H}^*$  | \longleftrightarrow  | $\text{ClHCl}_2^* + *$  |
| $\text{CCH}_3^* + \text{H}^*$  | \longleftrightarrow  | $\text{ClHCl}_3^* + *$  |

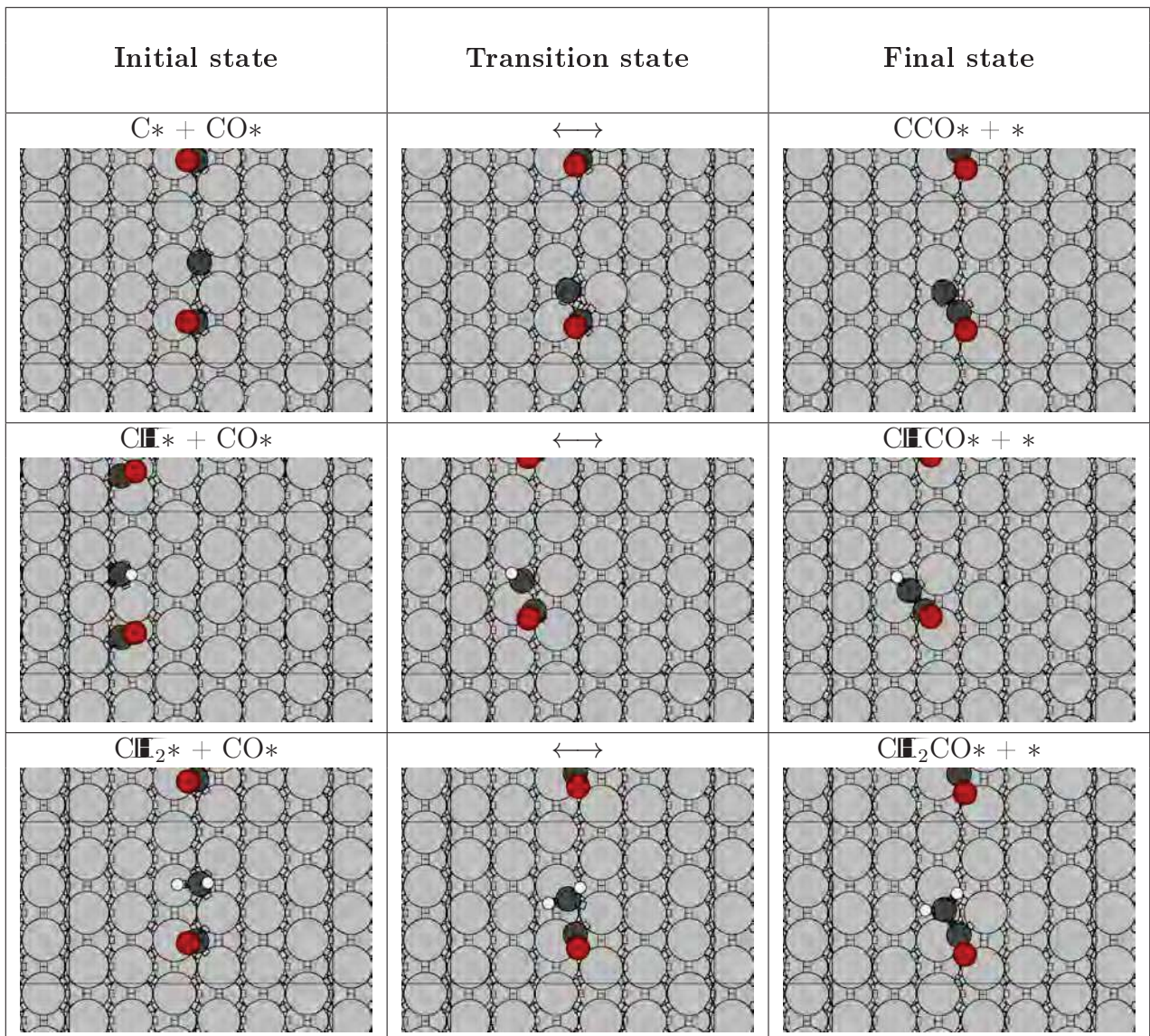
| Initial state | Transition state | Final state |
|--|---|--|
| $\text{CH}_2\text{CH}_2^* + \text{H}^*$  | \longleftrightarrow  | $\text{CH}_2\text{CH}_2^* + *$  |
| $\text{CH}_2\text{CH}_3^* + \text{H}^*$  | \longleftrightarrow  | $\text{CH}_2\text{CH}_3^* + *$  |
| $\text{CH}_2\text{CH}_3^* + \text{H}^*$  | \longleftrightarrow  | $\text{CH}_3\text{CH}_3 + 2*$  |

8.7 Elementary reaction steps as calculated for the CO-insertion reactions

Table 24: Elementary reaction steps as calculated for the CO-insertion reactions.

| # | Elementary Reaction Steps | ν_f [s ⁻¹] | E_f [J/mol] | ν_b [s ⁻¹] | E_b [J/mol] |
|----|--|----------------------------|---------------|----------------------------|---------------|
| 45 | $C^* + CO^* \longleftrightarrow CCO^* + *$ | 1.50e+13 | 1.66e+05 | 3.12e+12 | 3.78e+04 |
| 46 | $CH^* + CO^* \longleftrightarrow CHCO^* + *$ | 4.38e+12 | 1.81e+05 | 4.84e+10 | 6.57e+04 |
| 47 | $CH_2^* + CO^* \longleftrightarrow CH_2CO^* + *$ | 1.47e+11 | 1.48e+05 | 6.47e+14 | 4.77e+03 |

Table 25: Elementary reaction steps as calculated for the CO-insertion reactions.



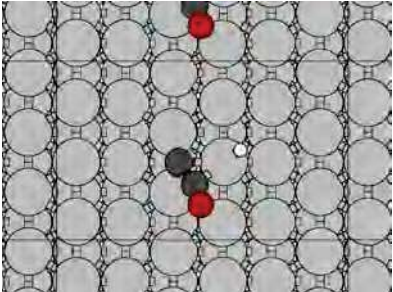
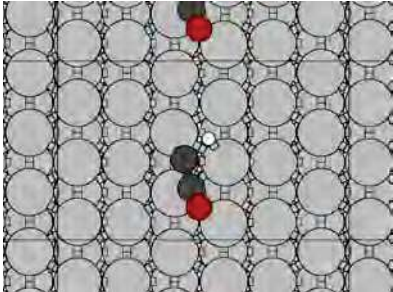
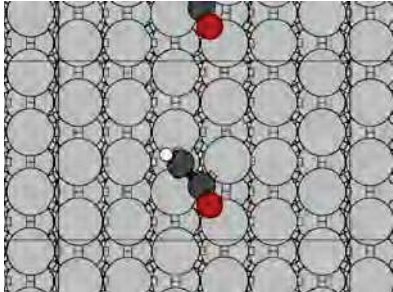
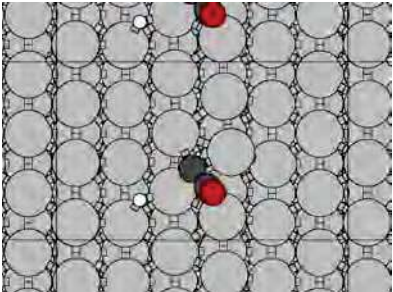
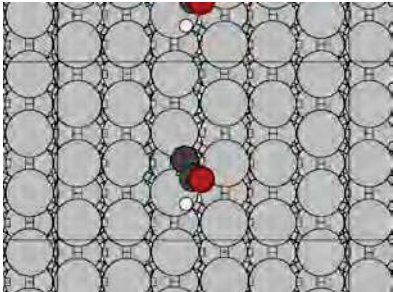
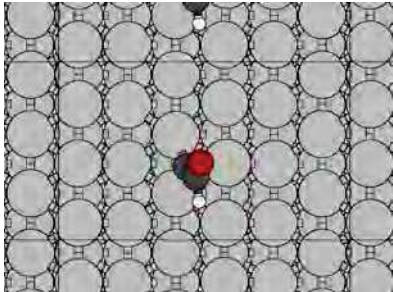
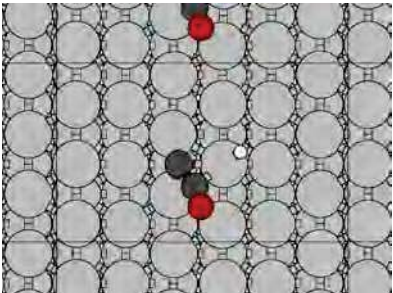
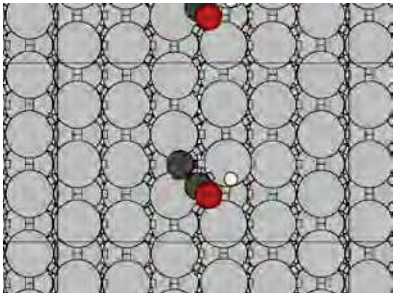
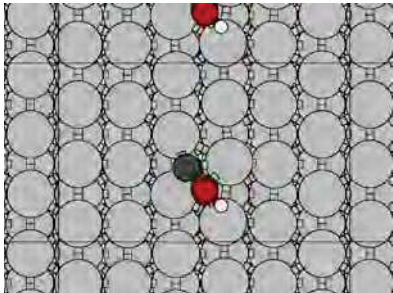
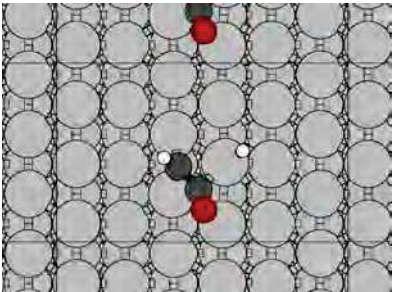
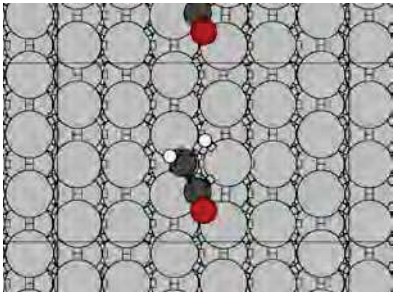
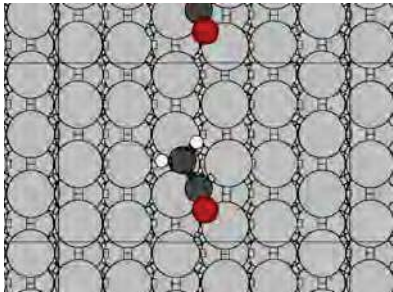
8.8 Elementary reaction steps as calculated for the hydrogenation towards C2-Oxygenates

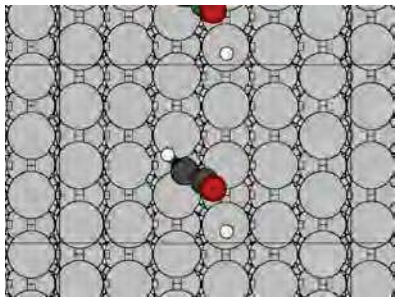
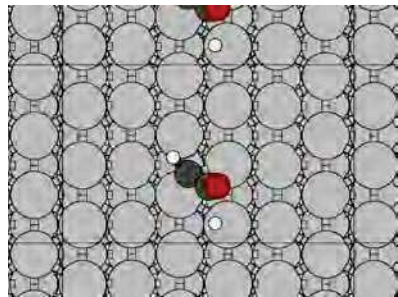
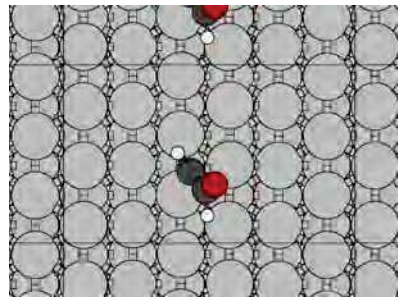
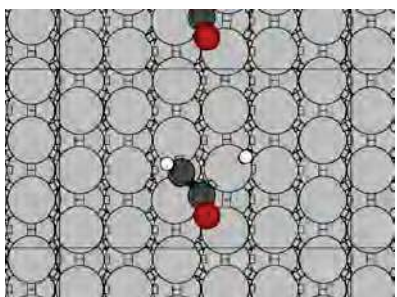
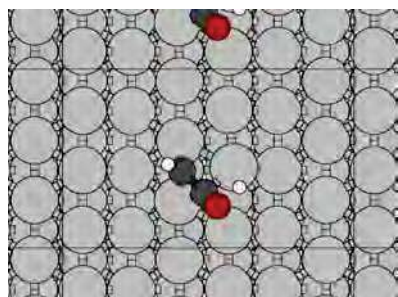
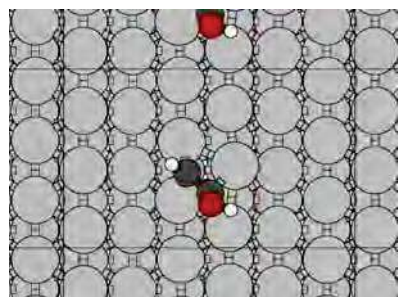
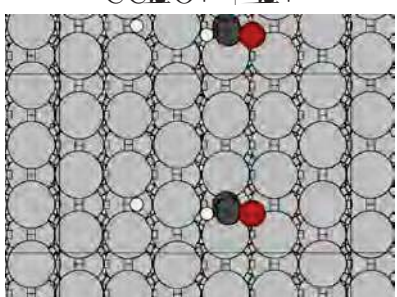
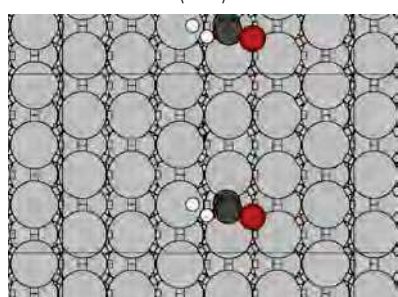
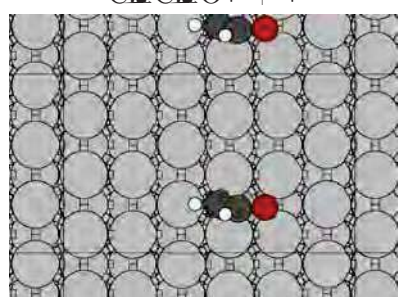
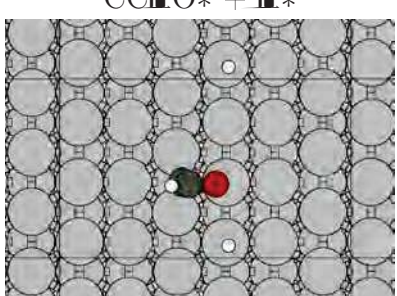
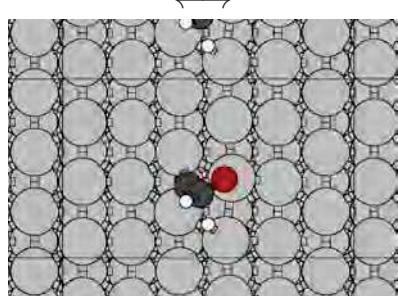

Table 26: Elementary reaction steps as calculated for synthesis towards C2-Oxygenates.

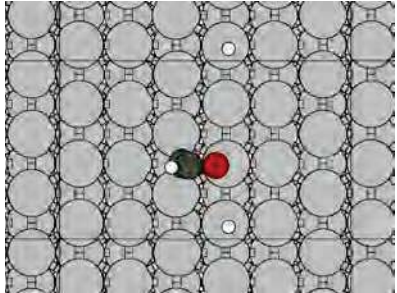
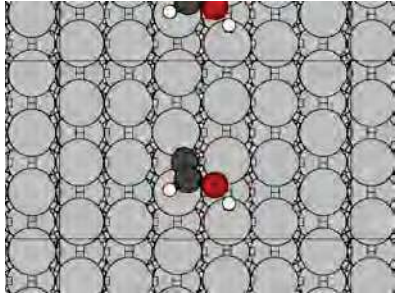
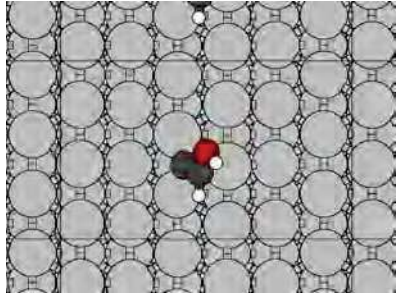
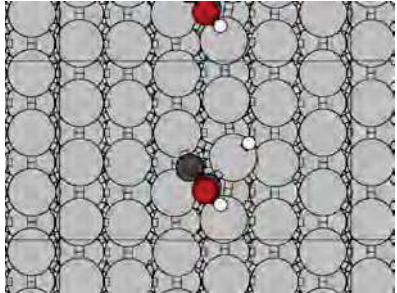
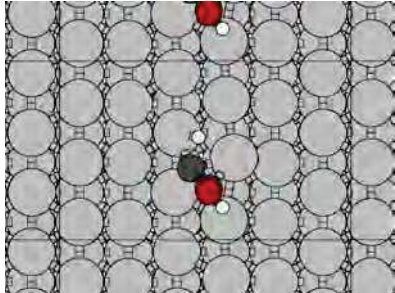
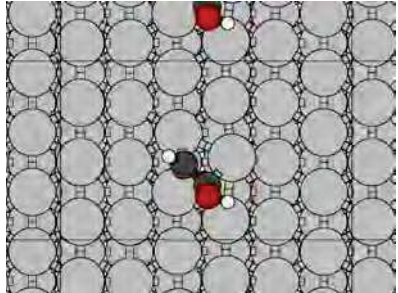
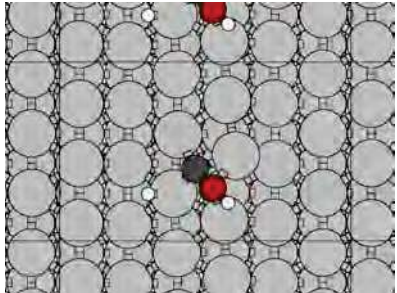
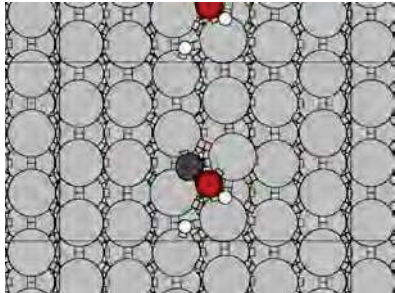
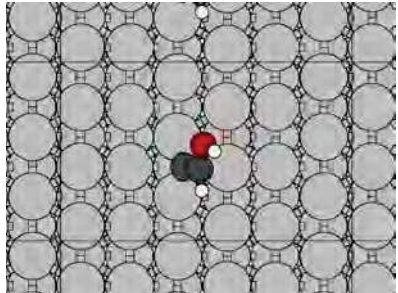
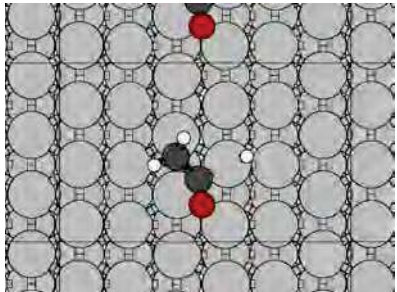
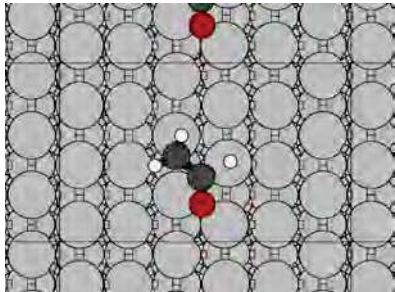
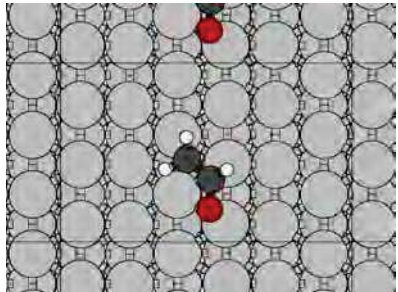
| # | Elementary Reaction Steps | | ν_f [s ⁻¹] | E_f [J/mol] | ν_b [s ⁻¹] | E_b [J/mol] | |
|----|--|---|---|---------------|----------------------------|---------------|----------|
| 48 | CCO* + H* | ↔ | C ₂ HCO* + * | 5.55e+13 | 9.63e+04 | 7.11e+13 | 1.04e+05 |
| 49 | CCO* + H* | ↔ | CC ₂ HO* + * | 1.24e+11 | 1.13e+05 | 3.77e+13 | 3.82e+04 |
| 50 | CCO* + H* | ↔ | CCOH* + * | 2.63e+14 | 2.10e+05 | 4.62e+14 | 1.39e+05 |
| 51 | C ₂ HCO* + H* | ↔ | C ₂ H ₂ CO* + * | 4.88e+11 | 9.81e+04 | 6.18e+13 | 4.07e+03 |
| 52 | C ₂ HCO* + H* | ↔ | C ₂ HCHO* + * | 2.30e+12 | 1.10e+05 | 1.65e+10 | 1.39e+04 |
| 53 | C ₂ HCO* + H* | ↔ | C ₂ HCOH* + * | 3.35e+12 | 1.87e+05 | 7.91e+12 | 1.10e+05 |
| 54 | CC ₂ HO* + H* | ↔ | C ₂ HCHO* + * | 4.20e+10 | 2.61e+04 | 3.49e+11 | 1.30e+04 |
| 55 | CC ₂ HO* + H* | ↔ | CC ₂ H ₂ O* + * | 5.28e+10 | 1.01e+05 | 1.55e+14 | 6.09e+04 |
| 56 | CC ₂ HO* + H* | ↔ | CC ₂ HOH* + * | 1.47e+11 | 1.02e+05 | 1.60e+12 | 1.06e+05 |
| 57 | CCOH* + H* | ↔ | C ₂ HCOH* + * | 3.63e+13 | 7.98e+04 | 3.65e+13 | 8.12e+04 |
| 58 | CCOH* + H* | ↔ | CC ₂ HOH* + * | 4.71e+13 | 6.02e+04 | 2.44e+13 | 5.79e+04 |
| 59 | C ₂ H ₂ CO* + H* | ↔ | C ₂ H ₂ CHO* + * | 5.34e+12 | 3.95e+04 | 1.91e+14 | 2.01e+04 |
| 60 | C ₂ H ₂ CO* + H* | ↔ | C ₂ H ₂ COH* + * | 2.43e+13 | 1.19e+05 | 3.64e+13 | 6.31e+04 |
| 61 | C ₂ HCHO* + H* | ↔ | C ₂ H ₂ CHO* + * | 2.84e+13 | 8.86e+04 | 2.77e+12 | 7.08e+04 |
| 62 | C ₂ HCHO* + H* | ↔ | C ₂ HCHO ₂ O* + * | 4.66e+10 | 1.60e+05 | 8.38e+11 | 1.16e+05 |
| 63 | C ₂ HCHO* + H* | ↔ | C ₂ HCHOH* + * | 1.16e+12 | 1.99e+05 | 3.07e+13 | 1.65e+05 |
| 64 | C ₂ HCOH* + H* | ↔ | C ₂ H ₂ COH* + * | 4.77e+12 | 1.16e+05 | 4.04e+12 | 4.27e+04 |
| 65 | C ₂ HCOH* + H* | ↔ | C ₂ HCHOH* + * | 2.51e+13 | 8.51e+04 | 2.15e+13 | 3.26e+04 |
| 66 | CC ₂ H ₂ O* + H* | ↔ | C ₂ HCHO ₂ O* + * | 2.98e+10 | 8.09e+04 | 6.12e+10 | 6.38e+04 |
| 67 | CC ₂ H ₂ O* + H* | ↔ | CC ₂ H ₂ OH* + * | 6.25e+11 | 9.28e+04 | 3.38e+10 | 9.28e+04 |
| 68 | CC ₂ HOH* + H* | ↔ | C ₂ HCHOH* + * | 3.85e+14 | 1.03e+05 | 9.12e+14 | 5.26e+04 |
| 69 | CC ₂ HOH* + H* | ↔ | CC ₂ H ₂ OH* + * | 4.78e+15 | 2.32e+05 | 1.07e+14 | 1.88e+05 |
| 70 | C ₂ H ₂ CHO* + H* | ↔ | C ₂ H ₃ CHO* + * | 1.82e+14 | 9.23e+04 | 5.65e+11 | 9.36e+04 |
| 71 | C ₂ H ₂ CHO* + H* | ↔ | C ₂ H ₂ CHO ₂ O* + * | 2.10e+14 | 9.25e+04 | 1.40e+13 | 1.68e+04 |
| 72 | C ₂ H ₂ CHO* + H* | ↔ | C ₂ H ₂ CHOH* + * | 6.93e+15 | 9.29e+04 | 5.90e+12 | 4.24e+04 |
| 73 | C ₂ H ₂ COH* + H* | ↔ | C ₂ H ₃ COH* + * | 5.46e+13 | 7.64e+04 | 1.30e+13 | 6.60e+04 |
| 74 | C ₂ H ₂ COH* + H* | ↔ | C ₂ H ₂ CHOH* + * | 1.55e+13 | 6.77e+04 | 4.13e+11 | 5.35e+04 |
| 75 | C ₂ HCHO ₂ O* + H* | ↔ | C ₂ H ₂ CHO ₂ O* + * | 5.38e+11 | 5.68e+04 | 4.76e+12 | 7.28e+03 |
| 76 | C ₂ HCHO ₂ O* + H* | ↔ | C ₂ HCHO ₂ OH* + * | 1.66e+11 | 8.29e+04 | 1.47e+12 | 8.36e+04 |
| 77 | C ₂ HCHOH* + H* | ↔ | C ₂ H ₂ CHOH* + * | 1.18e+14 | 7.68e+04 | 2.33e+15 | 4.19e+04 |
| 78 | C ₂ HCHOH* + H* | ↔ | C ₂ HCHO ₂ OH* + * | 2.82e+13 | 8.47e+04 | 1.91e+13 | 7.50e+04 |
| 79 | CC ₂ H ₂ OH* + H* | ↔ | C ₂ HCHO ₂ OH* + * | 4.89e+15 | 1.04e+05 | 1.47e+16 | 8.79e+04 |

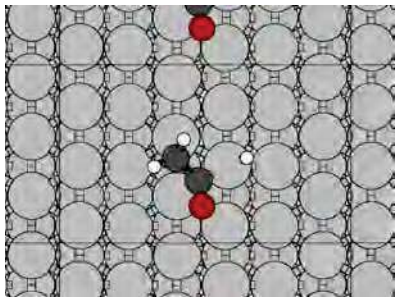
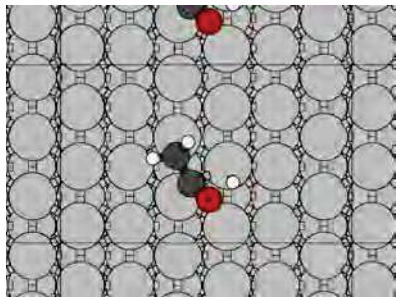
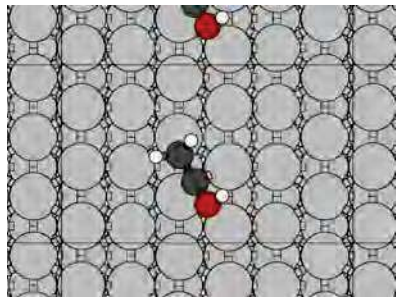
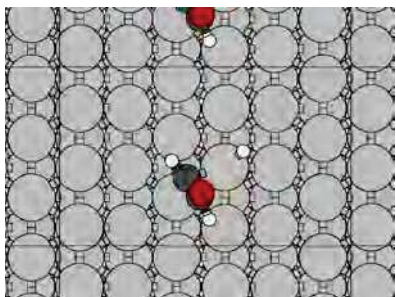
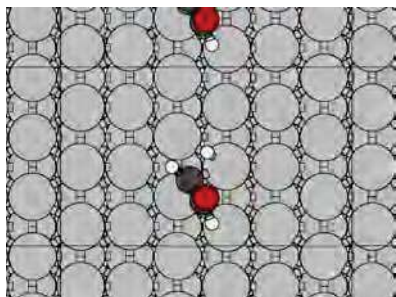
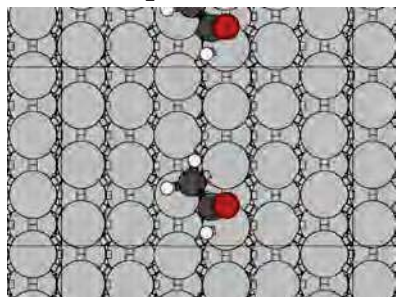
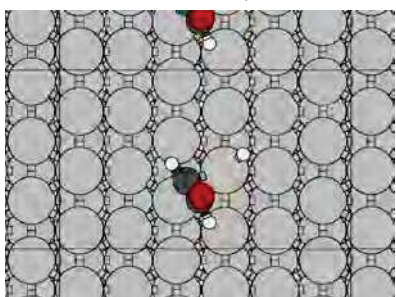
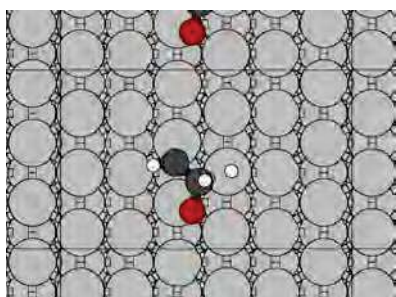
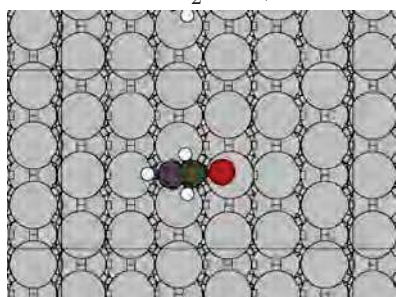
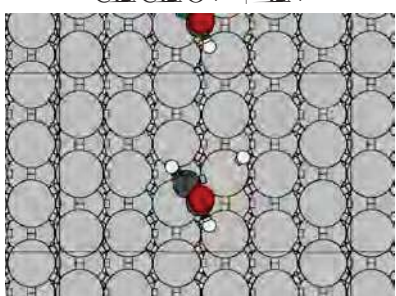
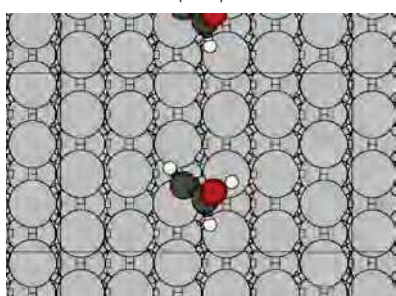

| # | Elementary Reaction Steps | ν_f [s ⁻¹] | E_f [J/mol] | ν_b [s ⁻¹] | E_b [J/mol] |
|----|---|----------------------------|---------------|----------------------------|---------------|
| 80 | $\text{CH}_3\text{CHO}^* + \text{H}^* \rightleftharpoons \text{CH}_3\text{CH}_2\text{O}^* + ^*$ | 6.66e+13 | 1.13e+05 | 3.32e+16 | 3.62e+04 |
| 81 | $\text{CH}_3\text{CHO}^* + \text{H}^* \rightleftharpoons \text{CH}_3\text{CHOH}^* + ^*$ | 5.03e+12 | 8.97e+04 | 2.66e+12 | 1.52e+04 |
| 82 | $\text{CH}_3\text{COH}^* + \text{H}^* \rightleftharpoons \text{CH}_3\text{CHOH}^* + ^*$ | 2.34e+12 | 9.17e+04 | 1.80e+10 | 6.52e+04 |
| 83 | $\text{CH}_2\text{CHO}^* + \text{H}^* \rightleftharpoons \text{CH}_3\text{CH}_2\text{O}^* + ^*$ | 1.09e+13 | 1.71e+05 | 5.64e+13 | 1.71e+05 |
| 84 | $\text{CH}_2\text{CHO}^* + \text{H}^* \rightleftharpoons \text{CH}_2\text{CHOH}^* + ^*$ | 1.99e+12 | 1.47e+05 | 1.06e+12 | 9.31e+04 |
| 85 | $\text{CH}_2\text{CHOH}^* + \text{H}^* \rightleftharpoons \text{CH}_3\text{CHOH}^* + ^*$ | 6.37e+11 | 1.47e+05 | 2.62e+11 | 1.24e+05 |
| 86 | $\text{CH}_2\text{CHOH}^* + \text{H}^* \rightleftharpoons \text{CH}_2\text{CHOH}^* + ^*$ | 2.46e+12 | 4.65e+05 | 1.55e+14 | 3.86e+05 |
| 87 | $\text{CH}_2\text{CHOH}^* + \text{H}^* \rightleftharpoons \text{CH}_2\text{CHOH}^* + ^*$ | 1.21e+14 | 1.52e+05 | 4.55e+14 | 4.77e+04 |
| 88 | $\text{CH}_3\text{CHO}^* + \text{H}^* \rightleftharpoons \text{CH}_3\text{CHOH}^* + ^*$ | 8.86e+13 | 9.90e+04 | 8.01e+11 | 4.36e+04 |
| 89 | $\text{CH}_3\text{CHOH}^* + \text{H}^* \rightleftharpoons \text{CH}_3\text{CHOH}^* + ^*$ | 2.07e+14 | 1.22e+05 | 3.11e+12 | 6.42e+04 |
| 90 | $\text{CH}_2\text{CHOH}^* + \text{H}^* \rightleftharpoons \text{CH}_3\text{CHOH}^* + ^*$ | 6.84e+14 | 7.52e+04 | 1.64e+12 | 7.38e+04 |

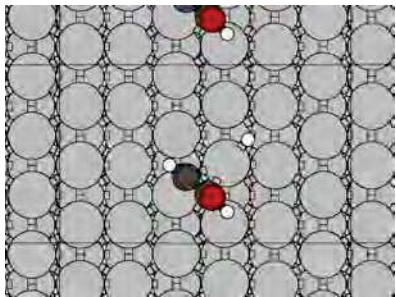
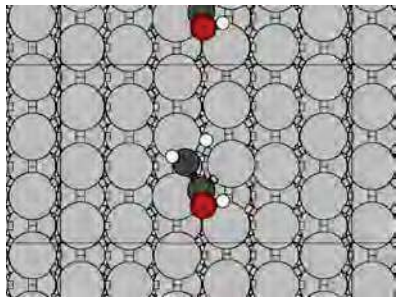
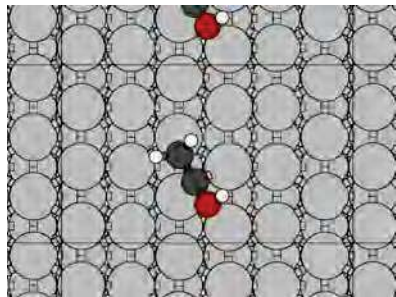
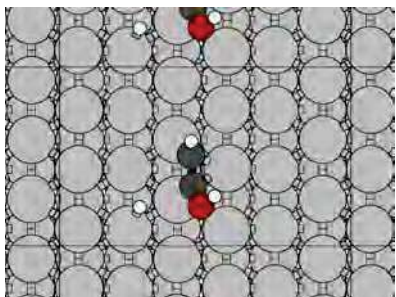
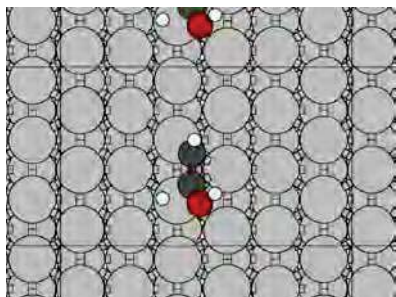
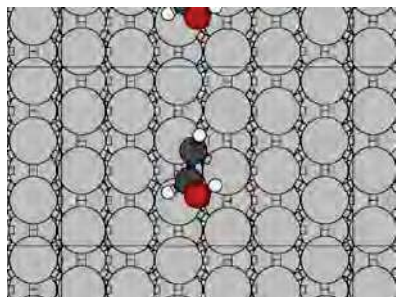
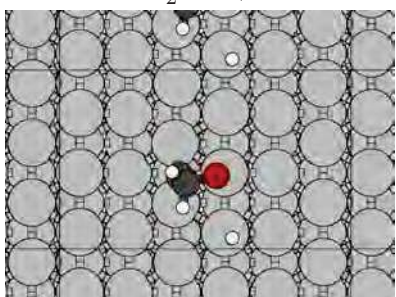
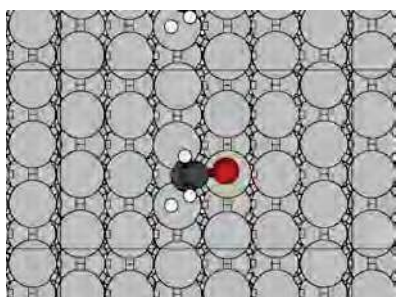
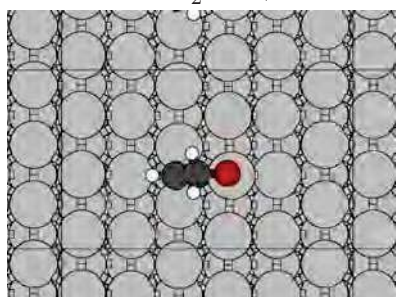
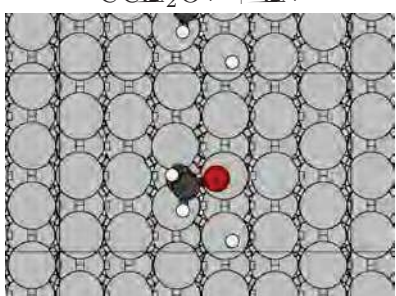
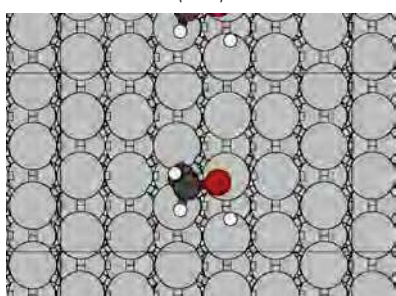
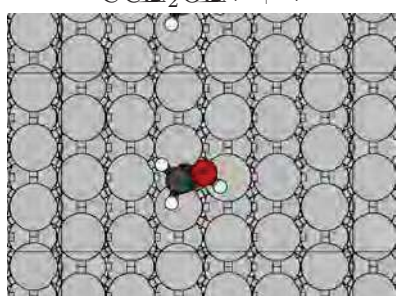
Table 27: Elementary reaction steps as calculated for the C2-Oxygenates.

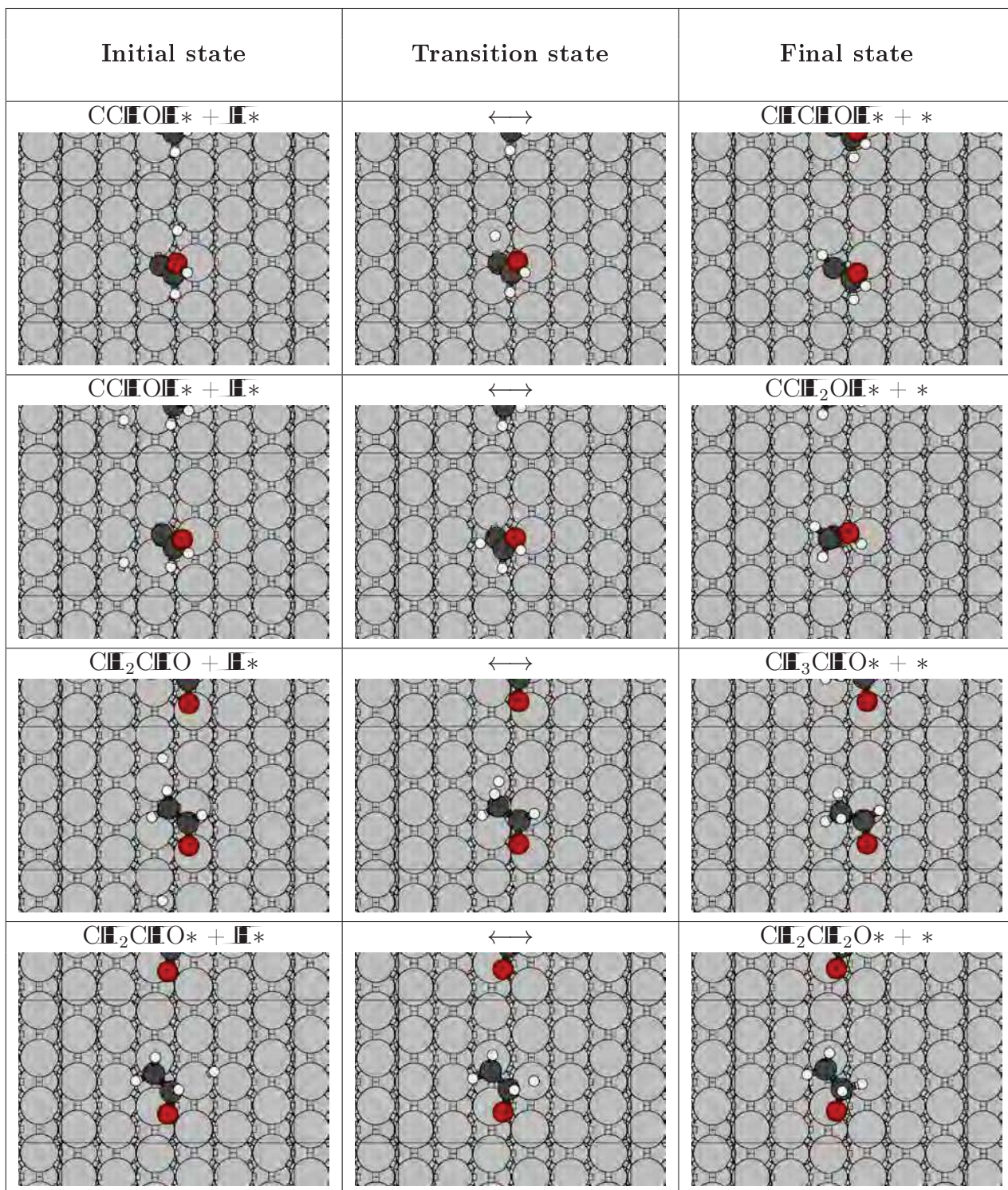
| Initial state | Transition state | Final state |
|---|---|---|
| $\text{CCO}^* + \text{H}^*$  | \longleftrightarrow  | $\text{CHCO}^* + *$  |
| $\text{CCO}^* + \text{H}^*$  | \longleftrightarrow  | $\text{CCHO}^* + *$  |
| $\text{CCO}^* + \text{H}^*$  | \longleftrightarrow  | $\text{CCOH}^* + *$  |
| $\text{CHCO}^* + \text{H}^*$  | \longleftrightarrow  | $\text{CH}_2\text{CO}^* + *$  |

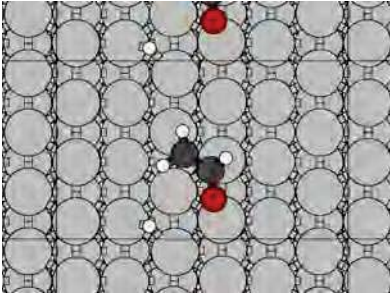
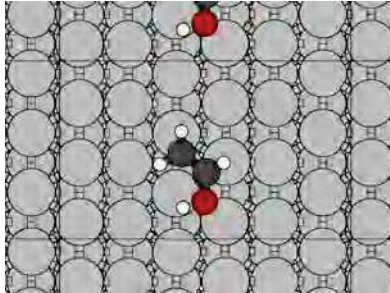
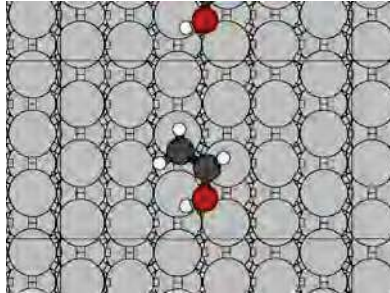
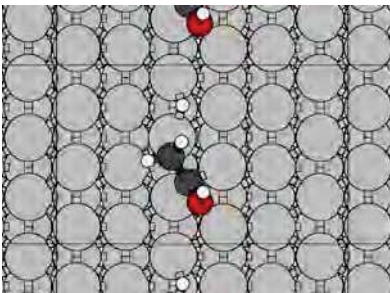
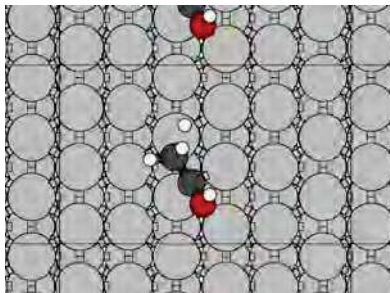
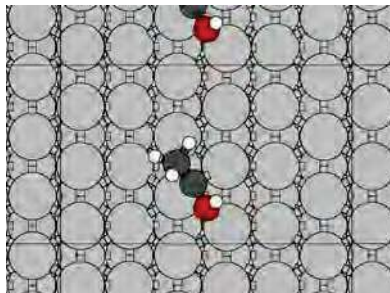
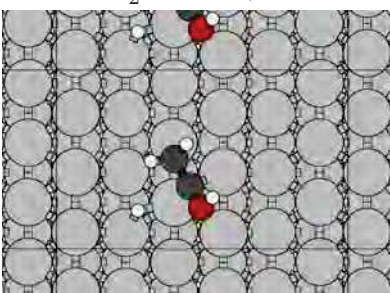
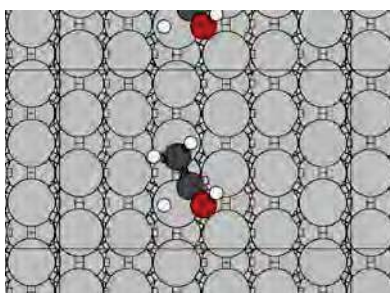
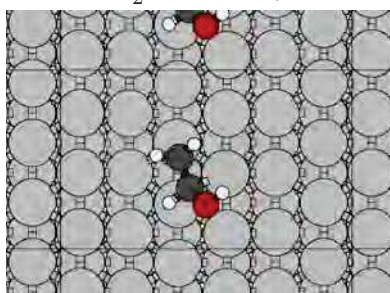
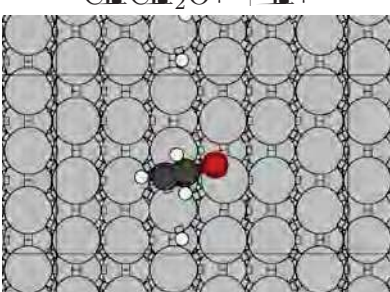

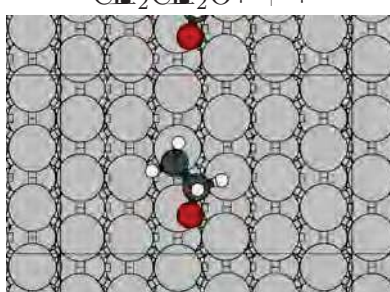
| Initial state | Transition state | Final state |
|---|---|---|
| $\text{CHCO}^* + \text{H}^*$  | \longleftrightarrow  | $\text{CHCHO}^* + *$  |
| $\text{CHCO}^* + \text{H}^*$  | \longleftrightarrow  | $\text{CHCOH}^* + *$  |
| $\text{CCHO}^* + \text{H}^*$  | \longleftrightarrow  | $\text{CHCHO}^* + *$  |
| $\text{CCHO}^* + \text{H}^*$  | \longleftrightarrow  | $\text{CCH}_2\text{O}^* + *$  |

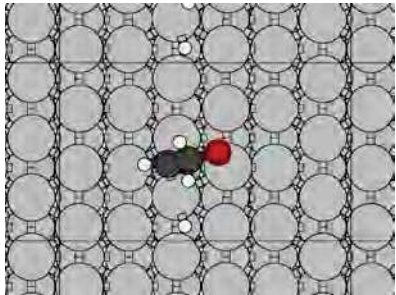
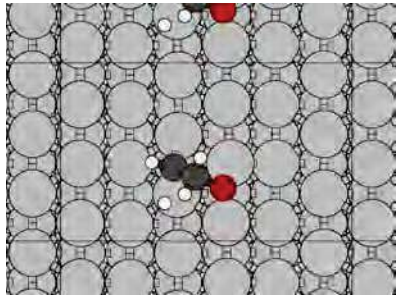
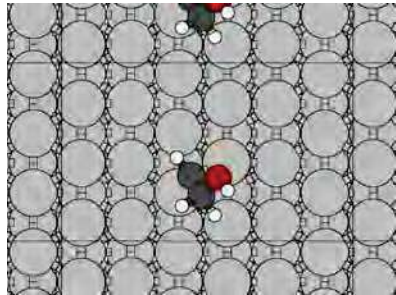
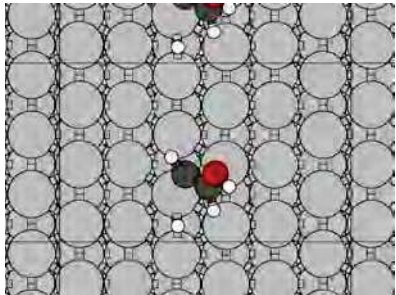
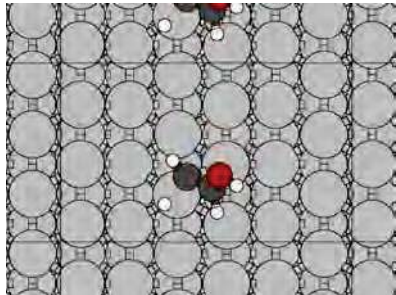
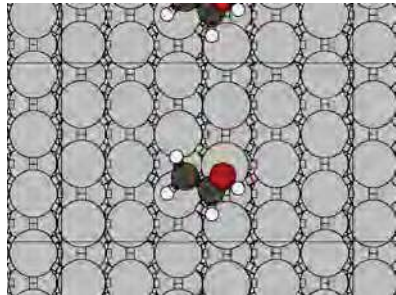
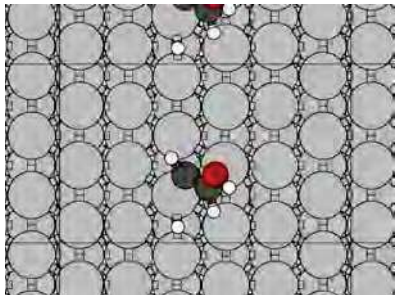
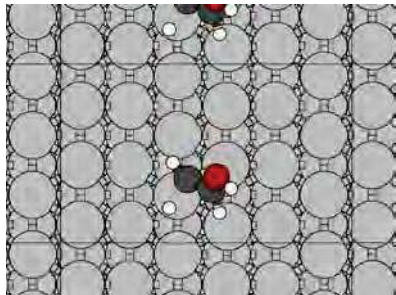
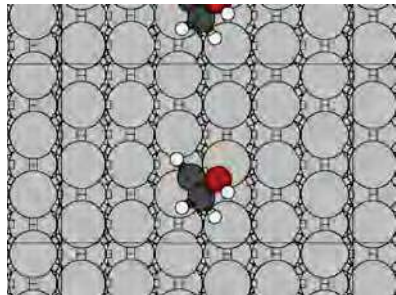
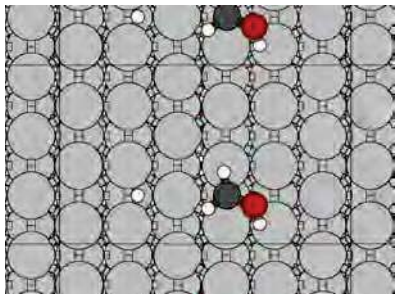
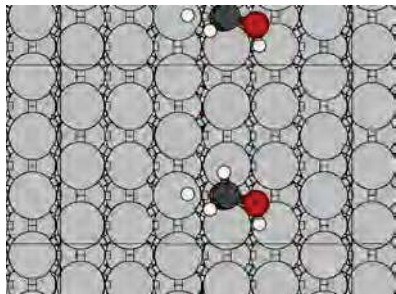
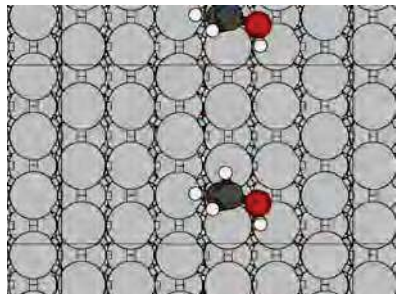
| Initial state | Transition state | Final state |
|--|---|--|
| $\text{CC}^{\text{H}}\text{O}^* + \text{H}^*$  | \longleftrightarrow  | $\text{CC}^{\text{H}}\text{OH}^* + *$  |
| $\text{CCO}^{\text{H}}* + \text{H}^*$  | \longleftrightarrow  | $\text{C}^{\text{H}}\text{COH}^* + *$  |
| $\text{CCO}^{\text{H}}* + \text{H}^*$  | \longleftrightarrow  | $\text{CC}^{\text{H}}\text{OH}^* + *$  |
| $\text{C}^{\text{H}}_2\text{CO}^* + \text{H}^*$  | \longleftrightarrow  | $\text{C}^{\text{H}}_2\text{CHO}^* + *$  |

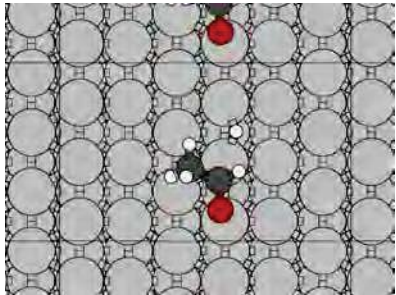
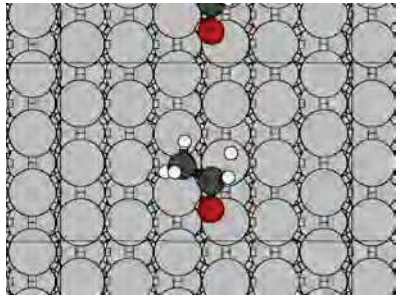
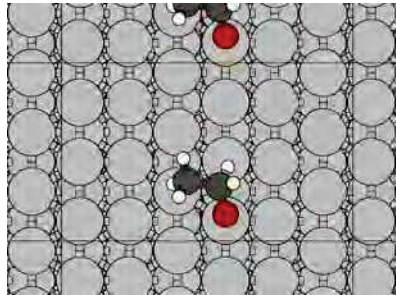
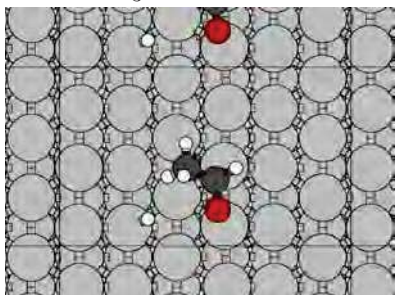
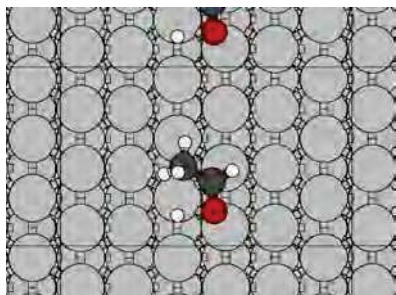
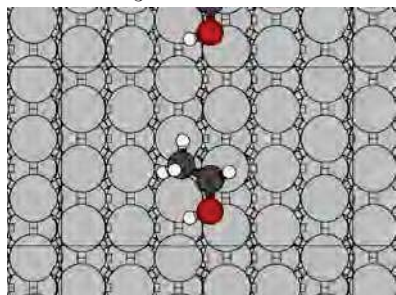
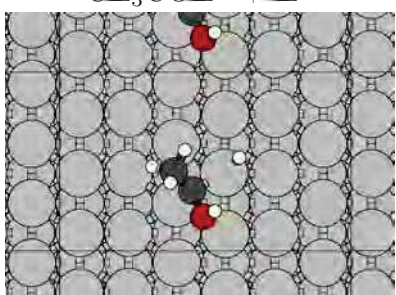
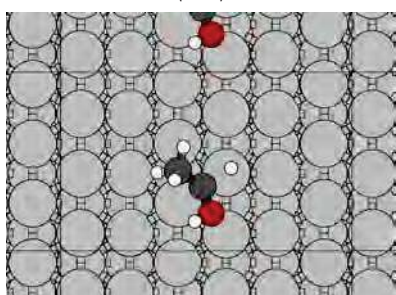
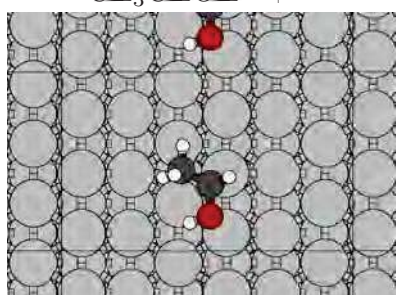
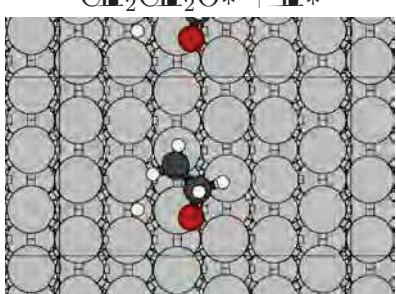
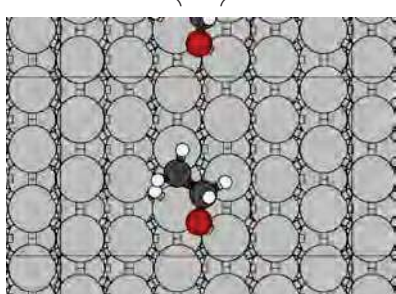
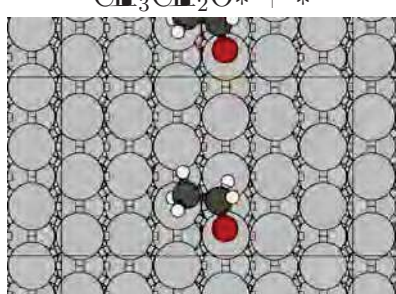
| Initial state | Transition state | Final state |
|--|---|---|
| $\text{CH}_2\text{CO}^* + \text{H}^*$  | \longleftrightarrow  | $\text{CH}_2\text{COH}^* + *$  |
| $\text{CHCHO}^* + \text{H}^*$  | \longleftrightarrow  | $\text{CH}_2\text{CHO}^* + *$  |
| $\text{CHCHO}^* + \text{H}^*$  | \longleftrightarrow  | $\text{CH}_2\text{CHO}^* + *$  |
| $\text{CHCHO}^* + \text{H}^*$  | \longleftrightarrow  | $\text{CH}_2\text{CHOH}^* + *$  |

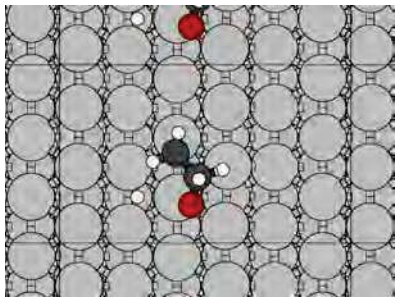
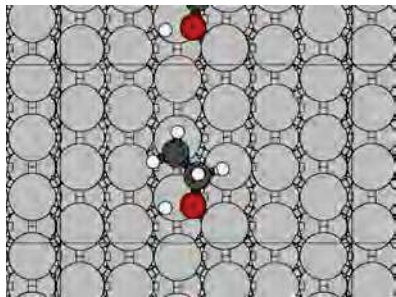
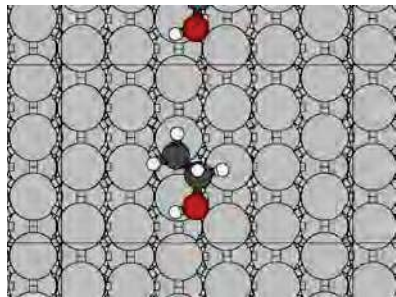
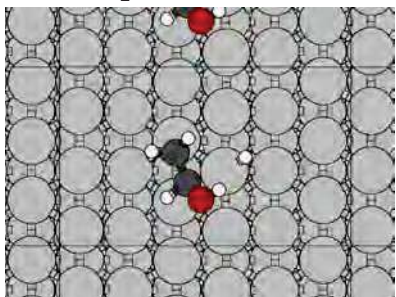
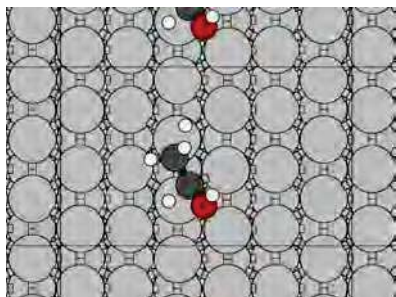
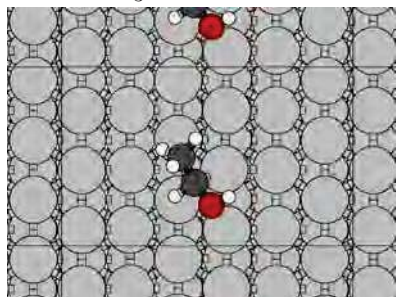
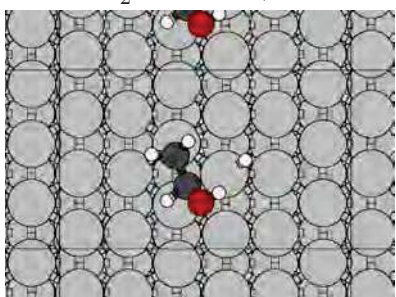
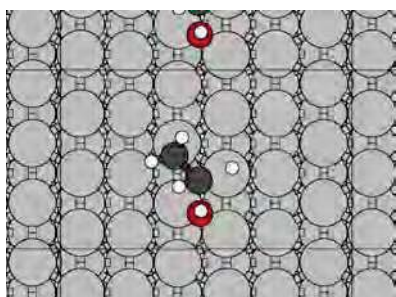
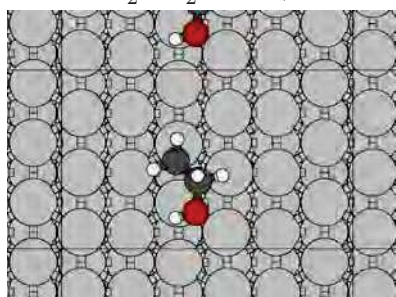
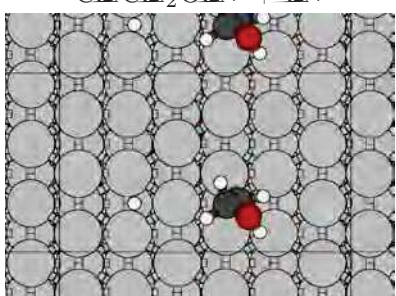
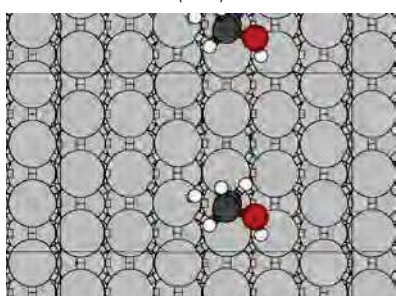
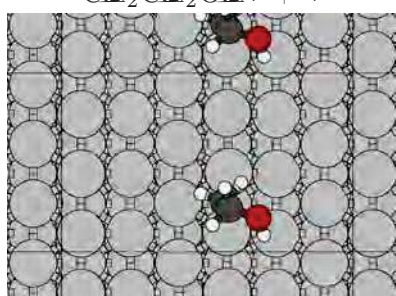
| Initial state | Transition state | Final state |
|--|---|--|
| $\text{CH}_2\text{CO}^* + \text{H}^*$  | \longleftrightarrow  | $\text{CH}_2\text{CO}^* + *$  |
| $\text{CH}_2\text{CO}^* + \text{H}^*$  | \longleftrightarrow  | $\text{CH}_2\text{CHO}^* + *$  |
| $\text{CCl}_2\text{O}^* + \text{H}^*$  | \longleftrightarrow  | $\text{CCl}_2\text{O}^* + *$  |
| $\text{CCl}_2\text{O}^* + \text{H}^*$  | \longleftrightarrow  | $\text{CCl}_2\text{OH}^* + *$  |

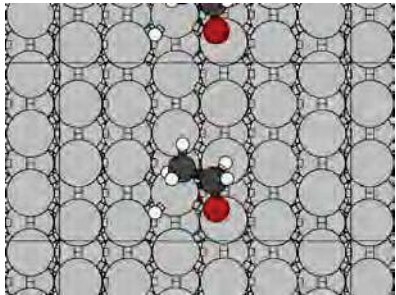
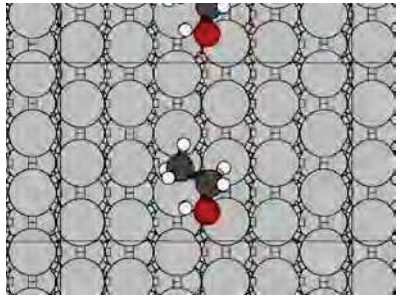
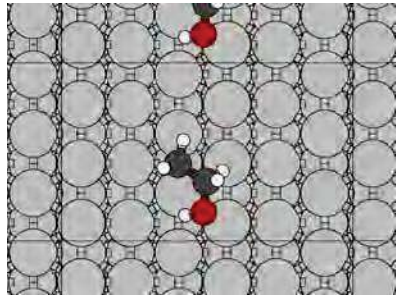
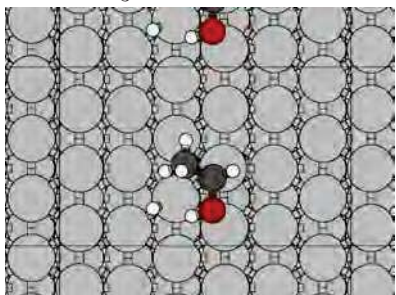
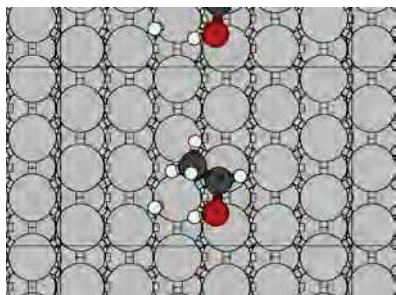
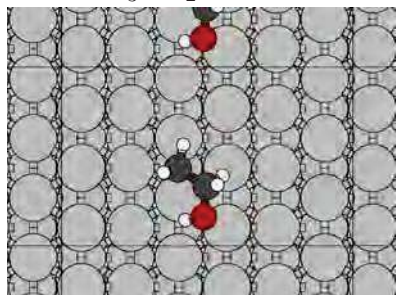
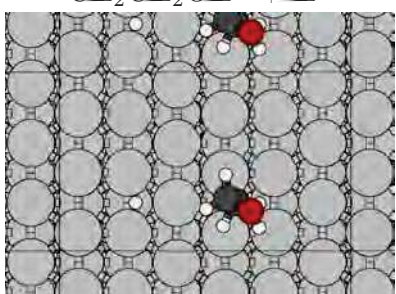
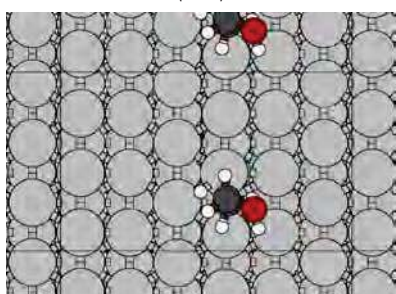
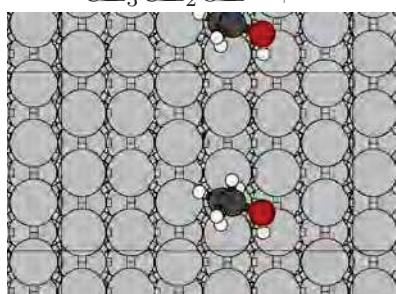


| Initial state | Transition state | Final state |
|---|---|---|
| $\text{CH}_2\text{CHO}^* + \text{H}^*$  | \longleftrightarrow  | $\text{CH}_2\text{CHOH}^* + *$  |
| $\text{CH}_2\text{COH}^* + \text{H}^*$  | \longleftrightarrow  | $\text{CH}_3\text{COH}^* + *$  |
| $\text{CH}_2\text{COH}^* + \text{H}^*$  | \longleftrightarrow  | $\text{CH}_2\text{CHOH}^* + *$  |
| $\text{CHCH}_2\text{O}^* + \text{H}^*$  | \longleftrightarrow  | $\text{CH}_2\text{CH}_2\text{O}^* + *$  |

| Initial state | Transition state | Final state |
|--|---|--|
| $\text{CH}_3\text{CH}_2\text{O}^* + \text{H}^*$  | \longleftrightarrow  | $\text{CH}_3\text{CH}_2\text{OH}^* + *$  |
| $\text{CH}_3\text{CHOH}^* + \text{H}^*$  | \longleftrightarrow  | $\text{CH}_3\text{C(OH)}_2^* + *$  |
| $\text{CH}_3\text{CHOH}^* + \text{H}^*$  | \longleftrightarrow  | $\text{CH}_3\text{CH}_2\text{OH}^* + *$  |
| $\text{CC(OH)}_2^* + \text{H}^*$  | \longleftrightarrow  | $\text{CH}_3\text{CH}_2\text{OH}^* + *$  |

| Initial state | Transition state | Final state |
|---|---|---|
| $\text{CH}_3\text{CHO}^* + \text{H}^*$  | \longleftrightarrow  | $\text{CH}_3\text{CH}_2\text{O}^* + *$  |
| $\text{CH}_3\text{CHO}^* + \text{H}^*$  | \longleftrightarrow  | $\text{CH}_3\text{CHOH}^* + *$  |
| $\text{CH}_3\text{COH}^* + \text{H}^*$  | \longleftrightarrow  | $\text{CH}_3\text{CHOH}^* + *$  |
| $\text{CH}_2\text{CHO}^* + \text{H}^*$  | \longleftrightarrow  | $\text{CH}_3\text{CH}_2\text{O}^* + *$  |

| Initial state | Transition state | Final state |
|---|---|---|
| $\text{CH}_2\text{CH}_2\text{O}^* + \text{H}^*$  | \longleftrightarrow  | $\text{CH}_2\text{CH}_2\text{OH}^* + ^*$  |
| $\text{CH}_2\text{CH}(\text{OH})^* + \text{H}^*$  | \longleftrightarrow  | $\text{CH}_3\text{CH}(\text{OH})^* + ^*$  |
| $\text{CH}_2\text{CH}(\text{OH})^* + \text{H}^*$  | \longleftrightarrow  | $\text{CH}_2\text{CH}_2\text{OH}^* + ^*$  |
| $\text{CH}(\text{CH}_2\text{OH})^* + \text{H}^*$  | \longleftrightarrow  | $\text{CH}_2\text{CH}_2\text{OH}^* + ^*$  |

| Initial state | Transition state | Final state |
|---|---|--|
| $\text{CH}_3\text{CH}_2\text{O}^* + \text{H}^*$  | \longleftrightarrow  | $\text{CH}_3\text{CH}_2\text{OH}^* + *$  |
| $\text{CH}_3\text{CHOH}^* + \text{H}^*$  | \longleftrightarrow  | $\text{CH}_3\text{CH}_2\text{OH}^* + *$  |
| $\text{CH}_2\text{CH}_2\text{OH}^* + \text{H}^*$  | \longleftrightarrow  | $\text{CH}_3\text{CH}_2\text{OH}^* + *$  |

8.9 Elementary reaction steps as calculated for the hydrogenation towards C3-Oxygenates

Table 28: Elementary reaction steps as calculated needed for formation of C₃-Oxygenates.

| # | Elementary Reaction Steps | E_f [J/mol] | E_b [J/mol] |
|----|--|---------------|---------------|
| 91 | $\text{CH}_2\text{CO}^* + * \rightleftharpoons \text{CH}_2\text{C}^* + \text{O}^*$ | 1.88 e+05 | 2.89e+05 |
| 92 | $\text{CH}_2\text{CHO}^* + * \rightleftharpoons \text{CH}_2\text{CH}^* + \text{O}^*$ | 1.24e+05 | 1.52e+05 |
| 93 | $\text{CHCH}_3^* + \text{CO}^* \rightleftharpoons \text{CH}_3\text{CHCO}^* + *$ | 2.09e+05 | 1.06e+05 |

Table 29: Elementary reaction steps as calculated for the C3-Oxygenates.

